universität wien

MASTERARBEIT / MASTER'S THESIS

Titel der Masterarbeit / Title of the Master's Thesis

„Study of Global Vortical Null Geodesics in Kerr Spacetime“

verfasst von / submitted by

Tobias Sutter, BSc

angestrebter akademischer Grad / in partial fulfilment of the requirements for the degree of

Master of Science (MSc)

Wien, 2021 / Vienna, 2021

Studienkennzahl lt. Studienblatt / degree programme code as it appears on the student record sheet:	A 066 876
Studienrichtung lt. Studienblatt / degree programme as it appears on the student record sheet:	Masterstudium Physik
Betreut von / Supervisor:	Univ.-Prof. Piotr T. Chruściel, MSc PhD
Mitbetreut von / Co-Supervisor:	Dr. Maciej Maliborski

Acknowledgements

First I want to thank my two supervisors Piotr T. Chruściel and Maciej Maliborski. I especially want to express my gratitude to the former for introducing me to the topic of special and general relativity through his interesting lectures and for giving me the opportunity to do my master's project in the gravitational physics group. Almost even more appreciation deserves my co-supervisor Maciej Maliborski who introduced me to the interesting topic of numerical relativitiy and helped me with guidance and useful discussions throughout the project. He also ensured an uncomplicated entry into the gravitational physics group and made it possible for me to attend the CERS10 meeting in Potsdam/Golm.
The next person I want to thank with all my heart is my girlfriend Eva Weiler who always showed emotional support for me and helped me through tough times. I could always count on her to discuss any problems I had, regardless of them being of academic or personal nature. Without her, the last year certainly would have been a lot more difficult for me.
And I certainly must not forget to also give thanks to my family and friends, who were always there for me. They always encouraged me to follow my dreams and supported me in any matter. There was never a time when none of them had an open ear and lead me to the right decisions through their honest opinions.

Abstract

The aim of this thesis is in the broadest sense the visualisation of a Kerr black hole. In particular, we consider an analytic extension of the Kerr metric which allows for two asymptotically flat regions of spacetime, one with positive radial coordinate (where the central is attractive) and one with negative radial coordinate (where the central object acts repellent). Based on this fact, we want to answer the question how a stationary observer very far away from the black hole in the negative region perceives a stationary light source at positive radii. To this end, we study null geodesics connecting the source with the observer. Such geodesics belong to the subclass of so-called "vortical geodesics", characterised by the negativity of Carter's constant. We first discuss some general features of these vortical null geodesics (both known and new results), before we go on and analytically and numerically solve the geodesic equations of motion in Kerr spacetime. After that, to get a feeling of these geodesics, we take a closer look at some example geodesics (i.e. trajectories which photons take from the source to the observer) and their appearance in Kerr-Schild coordinates (which serve as pseudo-Cartesian coordinates). Finally, we create visualisations of what the observer we are considering would see when looking at the central object. To make the analysis of distorting effects easier, we consider two simple model light sources located at positive radial infinity. Within the context of this analysis we also created two short animations which can be found at https://www.quantagon.at/masters-thesis/.

Kurzfassung

Das Ziel dieser Arbeit ist im weitesten Sinne die Visualisierung eines schwarzen Lochs in der Kerr-Raumzeit. Insbesondere betrachten wir hierzu eine analytische Erweiterung der Kerr-Metrik welche zwei asymptotisch flache Regionen der Raumzeit zulässt, eine mit positiver radialer Koordinate (in welcher das zentrale Objekt anziehend wirkt) und eine mit negativer radialer Koordinate (in welcher das zentrale Objekt abstoßend wirkt). Auf dieser Tatsache aufbauend wollen wir die Frage beantworten, wie ein stationärer Beobachter, welcher sich weit entfernt vom schwarzen Loch in der Region mit negativem Radius befindet, eine Lichtquelle mit positivem Radius wahrnehmen würde. Dazu untersuchen wir Null-Geodäten, welche den Beobachter und die Lichtquelle verbinden. Diese Geodäten gehören zu der Unterklasse der sogenannten „strudelartigen Geodäten“, welche durch die Negativität der Carter-Konstante charakterisiert sind. Zuerst diskutieren wir einige generelle Eigenschaften dieser „strudelartigen Geodäten“(sowohl bekannte, als auch neue Resultate), bevor wir die Geodäten-(Bewegungs-)Gleichungen der Kerr-Raumzeit sowohl analytisch als auch numerisch lösen. Um ein Gefühl für diese Geodäten zu bekommen, betrachten wir einige exemplarische Geodäten (also die Bahnen der Photonen von der Quelle zum Beobachter) und deren Erscheinung in Kerr-Schild Koordinaten (welche uns als pseudo-kartesische Koordinaten dienen). Abschließend visualisieren wir, was der Beobachter in unserem Fall sieht, wenn er/sie direkt zum zentralen Objekt blickt. Um die Verzerrungs-Effekte einfacher analysieren zu können, betrachten wir zwei simple Modell-Lichtquellen bei positiver radialer Unendlichkeit. Im Rahmen dieser Analyse haben wir auch zwei kurze Animationen erstellt, welche unter https://www.quantagon.at/masters-thesis/ gefunden werden können.

Contents

1. Introduction

After Albert Einstein published the Theory of General Relativity and thus the famous field equations in 1916 [12], many people tried to solve them exactly. The first one to successfully do so was Karl Schwarzschild [33]. His solution describes the gravitational field of a non-rotating, non-charged point particle. In the standard form the metric looks as follows:

$$\begin{aligned} g &= g_{\mu\nu}\mathrm{d}x^\mu\mathrm{d}x^\nu \\ &= -(1-\frac{2m}{r})\mathrm{d}t^2 + \frac{1}{1-\frac{2m}{r}}\mathrm{d}r^2 + r^2\mathrm{d}\theta^2 + r^2\sin^2(\theta)\mathrm{d}\phi^2 \ . \end{aligned} \tag{1.1}$$

The units here are chosen such that $G = c = 1$. These so-called geometric units will be used throughout this thesis.
The Schwarzschild metric is very well studied and gives a lot of insights into general relativity. There is a strong uniqueness theorem for the Schwarzschild metric [3] which reads: *In a vacuum region, away from the set $\{r = 2m\}$, any spherically symmetric metric can locally be written in the Schwarzschild form, for some mass parameter m.* The theorem is named after George David Birkhoff, although it was already formulated by Jørg Tofte Jebsen two years prior.
One big drawback to this solution is the lack of rotation and electric charge. Angular momentum is nowadays still not very well understood when clouds of interstellar matter (ISM) collapse to form stars because the cloud has a much higher angular momentum than the resulting star. Therefore the angular momentum needs to be transported away from the star. One possible solution for this transport is the coupling of the collapsing ISM with its surroundings via a magnetic field for which electric charge is needed. Consequently, the infalling matter and thus the resulting star has to be electrically charged. At the end of the stars life, when collapsing again to form a black hole, it cannot simply get rid of its angular momentum and electric charge. That is why we definitely want those two quantities in our theory about black holes.
Solutions to Einsteins field equations containing electric charge were found pretty quickly by the work of various people between 1916 and 1921; two of them were Hans Reissner [30] and Gunnar Nordström [26]. The metric

$$g = -(1-\frac{2m}{r}+\frac{Q^2}{r^2})\mathrm{d}t^2 + (1-\frac{2m}{r}+\frac{Q^2}{r^2})^{-1}\mathrm{d}r^2 + r^2\mathrm{d}\theta^2 + r^2\sin^2(\theta)\mathrm{d}\phi^2 \tag{1.2}$$

is thus named Reissner-Nordström-metric and it describes a charged (electric charge is encoded in Q), non-rotating, spherically symmetric body [25].
It took a lot longer to find the solution of Einsteins field equations for a rotating body. Almost 50 years after Einstein's publication, Roy Kerr found the exact solution to the field equations for a rotating body in 1963 [21]. Unfortunately, there is no general Birkhoff uniqueness theorem for Kerr spacetime. Therefore, the spacetime in the vacuum region

outside a generic rotating object such as a star is not described by Kerr geometry. There are, however, uniqueness theorems for Kerr spacetime to describe the exact solution corresponding to stationary rotating black holes.
As for the history of black hole visualisations in Schwarzschild and Kerr spacetime (and therefore the study of null geodesics in these curved spacetimes), this field of research was starting to spread in the community in the 1970's with works by Bardeen [2] who calculated the shadow boundary for an observer in the exterior region of a Kerr black hole, Cunningham & Bardeen [11] who were considering observational features of a star (point source) orbiting around a Kerr black hole as seen by an observer in the exterior of the black hole, and Luminet [22] who first simulated the appearance of a thin accretion disk around a Schwarzschild black hole. Also in this era, ground work in the study of global behaviour of null geodesics in the extended Kerr spacetime was done by Helliwell & Mallinckrodt [18].
As computational power was increasing, many more people added to the previous works in different ways in the 1980's and 1990's. For the Schwarzschild solution two such additions were done by Fukue & Yokoyama [13] who added colour to the accretion disk, and by Marck [23] who solved the geodesic equations in Kerr-Schild coordinates. In the Kerr case one noticeable paper is by Viergutz [35] who extended the visualisation of a thin accretion disk done by [22] to the Kerr spacetime.
Nowadays, the field of black hole visualisations is more present than ever, owing this increase in popularity to advances in computational resources and in observational astronomy – the first photo of a black hole was taken using the Event Horizon Telescope in 2019 [34] which can be used to check numerical simulations. Some theoretical works include papers by Riazuelo [31] [32] in which a ray tracing code for both the Schwarzschild and the Kerr spacetime are presented, and a series of papers by Gralla & Lupsasca [17] [16] whose results involve analytic solutions to the geodesic equations of motion for null geodesics. And lastly, a team around Oliver in collaboration with Kip Thorne [19] created visualisations of the exterior region of a Kerr black hole with unprecedented resolution which was used in the Hollywood film "Interstellar".
It should be clear that this list of references is a non-exhaustive selection of what has been done in black hole visualisations and is by no means complete. The mentioned works are nothing but a small sample of what has been done so far.
As one can see, a lot of research has been conducted on the visualisation of the appearance of both stationary and rotating black holes in the exterior region, i.e. for an observer outside the event horizon. We will see in the subsequent chapter 2 that Kerr spacetime allows for two asymptotically flat regions, one for $r \to +\infty$ (exterior) and one for $r \to -\infty$, both being connected through the interior of the black hole. The region with $r < 0$ does not allow for horizons and thus represents a naked singularity. Furthermore, it lies beneath the Cauchy horizon, which is thought to be unstable. That is why this region is by most researchers deemed to be unphysical. Nonetheless, in this work we will assume that the region is indeed a physical part of the spacetime geometry of a rotating black hole. Based on this assumption, we will strive to answer the question: How would an observer far away in the negative-r-region perceive the central object (in the region $r < 0$ it is not a black hole anymore as there are no horizons shielding the curvature singularity, yet in the following we will refer to the central object as the black hole) when the light is emitted at a source at positive radii, therefore crossing over from $r > 0$ to $r < 0$? In previous works only visualisations for observers close to the black hole in the region with negative radius

were done (e.g. [32]), but not for an observer in the asymptotically flat region at $r \to -\infty$. Therefore, the aim of this thesis is to extend the works by [18], [17], and [32] in this regard.
In order to fully understand the question we want to answer and the implications thereof, we will start with some basics of Kerr spacetime in chapter 2, introducing not only the metric tensor but also some features arising from it, such as the horizons, the ring singularity, etc.
As the task of visualising the appearance of the black hole involves photons, which follow null geodesics, we will give an overview of the geodesic equations of motion in Kerr spacetime in chapter 3. It is also there that we analyse some of the geodesic equations, presenting both well known as well as new features arising from them, and thus setting the stage for subsequent chapters.
Chapter 4 serves the purpose of presenting two different ways of solving the geodesic equations. We will follow a recent approach by [17] in finding analytic solutions to the equations of motion for null geodesics, modifying it to suit our case and correcting some equations. Furthermore, we will shortly discuss a method of how to solve these equations numerically before we conclude the chapter by comparing both solutions.
To gain insight into the behaviour of the null geodesics connecting the source and the observer, we will present some visualisations of individual photon trajectories in chapter 5.
Finally, we will (partly) answer the main question concerning the appearance of the black hole for an observer very far away in the negative-r-region in chapter 6 before summarising our findings and giving an outlook regarding future work in chapter 7.

2. Basics of Kerr spacetime

This section serves the purpose to give an introduction to Kerr spacetime to the reader who may not be completely familiar with it or just wants to refresh their memory. Some knowledge of the Schwarzschild solution to the Einstein field equations is assumed. The aim being the acquisition of a basic qualitative understanding of some of the fundamental features of the spacetime without involving too much technicalities, not every statement is backed up by a rigorous proof. Those can be found in the references given in the text. Summarising, this section contains the definition of the metric tensor of Kerr spacetime and its forms in various coordinate systems, as well as the interpretation of the appearing parameters a and m. Thereafter, some of the intriguing features of Kerr spacetime are outlined, including the horizons, the ring singularity, the ergosphere, as well as the causality violating region (Carter's time machine). For a deeper understanding of the global properties of Kerr spacetime, the projection diagram is useful.

2.1. The metric

As for any solution to the Einstein Equations, the metric tensor can take many various forms depending on the coordinate system used. Thus, in order to be able to study different aspects of Kerr spacetime, we need to introduce different coordinate systems. According to which problem we are facing, we can then choose the most suitable coordinates.

2.1.1. Boyer-Lindquist coordinates

One of the most commonly used coordinate systems of Kerr spacetime are the so-called Boyer-Lindquist coordinates (t, r, θ, φ) [4], in which the metric tensor takes the form

$$g = -\frac{\Delta}{\Sigma}(\mathrm{d}t - a\sin^2(\theta)\,\mathrm{d}\varphi)^2 + \frac{\sin^2(\theta)}{\Sigma}\left((r^2+a^2)\,\mathrm{d}\varphi - a\,\mathrm{d}t)\right)^2 + \frac{\Sigma}{\Delta}\,\mathrm{d}r^2 + \Sigma\,\mathrm{d}\theta^2 \tag{2.1}$$

$$= -\left(1 - \frac{2mr}{\Sigma}\right)\mathrm{d}t^2 - \frac{4mar\sin^2\theta}{\Sigma}\,\mathrm{d}t\,\mathrm{d}\varphi + \frac{(r^2+a^2)^2 - a^2\Delta\sin^2\theta}{\Sigma}\sin^2\theta\,\mathrm{d}\varphi^2 + \frac{\Sigma}{\Delta}\,\mathrm{d}r^2 + \Sigma\,\mathrm{d}\theta^2 \tag{2.2}$$

with

$$\Sigma = r^2 + a^2\cos^2(\theta)\ ,\ \Delta = r^2 + a^2 - 2mr\ . \tag{2.3}$$

These coordinates are similar to spherical coordinates in the sense that the domain of definition of the polar coordinate is $0 < \theta < \pi/2$ while the azimuthal coordinate is 2π-periodic. The real parameters a and m are to be interpreted as the parameter regarding the black hole's rotation and mass, respectively. The basic reasoning of this interpretation and the respective ranges of a and m will be outlined in section 2.2. The characteristic of Boyer-Lindquist coordinates to be similar to spherical coordinates is further supported

by the fact that in the limit $a \to 0$ and $m \to 0$ one recovers flat spacetime in spherical coordinates. It is the two roots $\Sigma = 0$ and $\Delta = 0$ which give rise to some of the most important features of the spacetime, namely the ring singularity and the horizons. These will be discussed in sections 2.3.2 and 2.3.1, respectively. From the form of the metric it can easily be deduced that the spacetime admits the two Killing vectors ∂_t and ∂_φ. This is the case as all metric components are independent of both t and φ, meaning the metric is stationary and axially symmetric. Furthermore, the spacetime admits two distinct asymptotically flat regions, one for $r > 0$ and one for $r < 0$, i.e. the metric approaches a flat spacetime metric in the limit $r \to \pm\infty$. The coordinate singularity at $\Delta = 0$ only exists for positive r, since for negative r this function is strictly positive. As will be discussed in subsection 2.3.1, this lack of the singularity for $r < 0$ renders this asymptotic region generally unphysical. It is noteworthy that this region can also be described by leaving r positive but flipping the sign of the mass m. Hence, the black hole must be repellent for $r < 0$.

2.1.2. Eddington-Finkelstein-like coordinates

In order to avoid the coordinate singularity at $\Delta = 0$, thus regularizing the metric across the horizons, one can transform to new coordinates (u, r, θ, ψ) using

$$u = t - \nu_r r^* \tag{2.4}$$

$$\psi = \varphi - \nu_r r^\# \tag{2.5}$$

where $\nu_r = \pm 1$ was introduced and where we defined

$$r^* = \int \frac{r^2 + a^2}{\Delta} \mathrm{d}r \ , \tag{2.6}$$

$$r^\# = \int \frac{a}{\Delta} \mathrm{d}r \ . \tag{2.7}$$

These coordinates are based on the principal null congruences of the Kerr spacetime (i.e. in-/outgoing null geodesics with certain constants of motion), the case $\nu_r = -1$ describing the ingoing congruence, while $\nu_r = +1$ describes the outgoing congruence (cf. [29]). We will later associate the sign ν_r with the sign of the radial geodesic equation of motion (cf. section 3.1). The coordinates are tailored so that for these special in-/outgoing null geodesics (the null congruences), the corresponding coordinates ψ, u, as well as θ, are constant along the geodesic. We will encounter this fact later on in the subsections 3.2.2 and 5.1.3. In the former subsection we show that indeed the coordinates ψ, u, and θ stay constant for all times.
The resulting metric takes the form

$$\begin{aligned} g = &- \left(1 - \frac{2mr}{\Sigma}\right) \mathrm{d}u^2 - 2\nu_r \, \mathrm{d}r \, \mathrm{d}u + \Sigma \, \mathrm{d}\theta^2 \\ &+ 2\nu_r a \sin^2\theta \, \mathrm{d}\psi \, \mathrm{d}r + \frac{(r^2 + a^2)^2 - \Delta a^2 \sin^2\theta}{\Sigma} \sin^2\theta \, \mathrm{d}\psi^2 \\ &- \frac{4amr \sin^2\theta}{\Sigma} \, \mathrm{d}\psi \, \mathrm{d}u \ . \end{aligned} \tag{2.8}$$

Note that now no metric component contains Δ in the denominator, revealing the regular behaviour at $\Delta = 0$, independent of the sign ν_r. Choosing $\nu_r = -1$ leads to the so-called Eddington-Finkelstein-like coordinates initially discovered by Kerr [21]. The name stems from the fact that in the stationary limit $a \to 0$, one recovers the Eddington-Finkelstein extension of the Schwarzschild metric [36]. Similar to the case of Boyer-Lindquist coordinates, we can deduce the existence of two Killing vectors in these coordinates, namely ∂_u and ∂_ψ.

2.1.3. Kerr-Schild coordinates

Another way to get rid of the coordinate singularity at $\Delta = 0$ is by considering the so-called Kerr-Schild coordinates $(\tilde{t}, x, y, z)$, which cast the metric into the form

$$g = \eta + \frac{2mr^3}{r^4 + a^2 z^2} \left(\mathrm{d}\tilde{t} + \frac{r(x\,\mathrm{d}x + y\,\mathrm{d}y)}{a^2 + r^2} + \frac{a(y\,\mathrm{d}x - x\,\mathrm{d}y)}{a^2 + r^2} + \frac{z}{r}\,\mathrm{d}z \right)^2 \tag{2.9}$$

$$= \eta + H\,\ell^2 \,, \tag{2.10}$$

where we have the Minkowski metric $\eta = -\mathrm{d}\tilde{t}^2 + \mathrm{d}x^2 + \mathrm{d}y^2 + \mathrm{d}z^2$ and we defined

$$H := \frac{2mr^3}{r^4 + a^2 z^2} \,, \tag{2.11}$$

$$\ell \equiv \ell_\mu\,\mathrm{d}x^\mu := \mathrm{d}\tilde{t} + \frac{r(x\,\mathrm{d}x + y\,\mathrm{d}y)}{a^2 + r^2} + \frac{a(y\,\mathrm{d}x - x\,\mathrm{d}y)}{a^2 + r^2} + \frac{z}{r}\,\mathrm{d}z \,. \tag{2.12}$$

The transformation connecting (2.1) and (2.9) is given by [29]

$$x + iy = (r + ia)\, e^{i(\varphi + r^\#)} \sin(\theta) \,, \tag{2.13}$$

$$z = r\cos(\theta) \,, \tag{2.14}$$

$$\tilde{t} = t + r^* - r \,, \tag{2.15}$$

where $r^\#$ and r^* are given in (2.7) and (2.6), and i is the imaginary unit defined by $i = \sqrt{-1}$. The Boyer-Lindquist radius r is determined by the solution of

$$x^2 + y^2 + z^2 = r^2 + a^2 \left(1 - \frac{z^2}{r^2}\right) \,. \tag{2.16}$$

One striking feature of this coordinate system is the underlying Minkowski metric. Note that ℓ is a null vector with respect to both the Kerr metric and the Minkowski metric. Furthermore, this form of the metric is also regular at $\Delta = 0$ but still singular at $\Sigma = 0$. The Killing vectors in these coordinates are $\partial_{\tilde{t}}$ and $x\,\partial_y - y\,\partial_x$, which are easily obtained by transforming the two Killing vectors found in the Boyer-Lindquist coordinates [36]. In this form of the Kerr metric the asymptotic flatness of the spacetime in the limit $r \to \pm\infty$ is evident. This can be verified by noting that $H \propto r^{-1}$ for $|r| \gg 1$ while $\ell \to \mathrm{d}\tilde{t}$ in the same limit, thus resulting in $g_{\mu\nu} \to \eta_{\mu\nu}$.
The Kerr-Schild coordinates are especially useful for visualization purposes due to its underlying flat spacetime metric, enabling the usage of (x, y, z) as pseudo-Cartesian coordinates. In what follows we will drop the tilde in the coordinate time and hence write the Kerr-Schild coordinates as (t, x, y, z). It will be clear from the context whether t corresponds to the coordinate time in Boyer-Lindquist or Kerr-Schild coordinates.

2.1.4. Toroidal coordinates

As we will display in section 2.3.2, the non-removable curvature singularity of Kerr spacetime can be depicted to be a circular string lying in the x-y-plane in Kerr-Schild coordinates. In order to study the spacetime geometry near this singular ring, the authors of [8] introduced toroidal coordinates $(t, \hat{r}, \hat{\psi}, \hat{\varphi})$, whose construction we will briefly reproduce. The disk bounded by the ring singularity

$$D := \mathbb{R} \times \{x^2 + y^2 < a^2,\ z = 0\} \subset \mathbb{R} \times \mathbb{R}^3 \tag{2.17}$$

serves as the starting point of the construction of toroidal coordinates. By solving (2.16) for r and expand for small values of z, one arrives at

$$r = \pm \begin{cases} \frac{a|z|}{\sqrt{a^2-\rho^2}} - \frac{a\rho^2|z|z^2}{2(a^2-\rho^2)^{5/2}} + \mathcal{O}\left(z^4\right), & \rho < a \\ \sqrt{\rho^2 - a^2} + \frac{\rho^2 z^2}{2(\rho^2-a^2)^{3/2}} + \mathcal{O}\left(z^3\right), & \rho > a \end{cases} \tag{2.18}$$

where $\rho^2 := x^2 + y^2$ was defined. Independent of the sign of r in (2.18), there is no smoothness problem when crossing the equatorial plane from $z > 0$ to $z < 0$ in the case $\rho > a$, corresponding to the region outside the disk (2.17). However, for a smooth extension through the equatorial plane inside the disk ($\rho < a$), one needs to choose the opposite sign for r in the region $z < 0$ to the one chosen for $z > 0$. Thus, if an observer goes through the disk once from $z > 0$ to $z < 0$, they go from one asymptotically flat region with $r > 0$ to the other with $r < 0$. Then they might go around the ring further and cross the equatorial plane from $z < 0$ to $z > 0$ outside the disk, staying in the region $r < 0$, i.e. staying in the same asymptotically flat region. If they then go around even further and crosses it again from $z > 0$ to $z < 0$ inside the disk, they come back to the starting region $r > 0$. This feature can be taken care of by introducing a 4π-periodic function which corresponds to a natural angular coordinate $\hat{\psi}$ around the ring. Then the region $\hat{\psi} \in (-\pi, \pi)$ corresponds to positive values of r while $\hat{\psi} \in (\pi, 3\pi)$ corresponds to negative values of r.
To get from Kerr-Schild coordinates to toroidal coordinates, one makes use of the transformation of the spatial coordinates to toroidal coordinates $(t, \hat{r}, \hat{\psi}, \hat{\varphi})$:

$$x = [a + \hat{r}\cos(\hat{\psi})]\cos(\hat{\varphi})\ , \tag{2.19}$$

$$y = [a + \hat{r}\cos(\hat{\psi})]\sin(\hat{\varphi})\ , \tag{2.20}$$

$$z = \hat{r}\sin(\hat{\psi})\ . \tag{2.21}$$

A qualitative plot of these toroidal coordinates can be found in Fig. 2.1. It is straightforward to see that these coordinates only make sense if we restrict $\hat{r} < a$. These coordinates, although they may be useless for studying global properties of the spacetime due to this restriction, can be very helpful for studying the singular ring and the transition between the two asymptotically flat regions of the spacetime. The complete form of the metric in toroidal coordinates is rather lengthy and complicated and does not give any further insights which would be helpful in the understanding of the following discussion. For that reason the explicit metric tensor is not stated here.

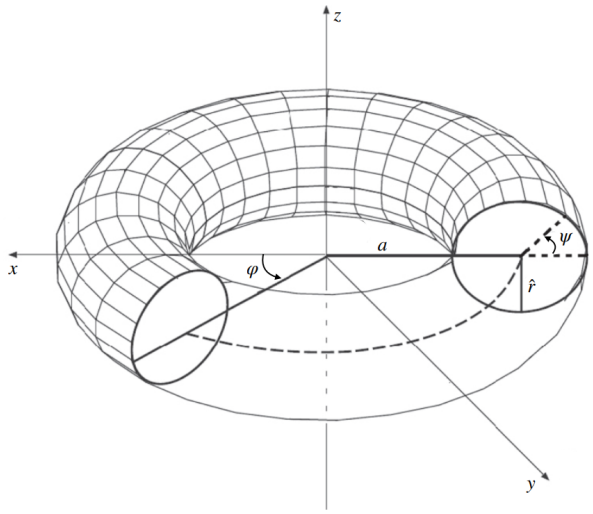

Figure 2.1.: Toroidal coordinates with major radius a and minor radius of the torus $\hat{r}$. The coordinate $\hat{\varphi}$ is 2π-periodic while $\hat{\psi}$ is 4π-periodic. This figure is taken from [8] Fig. III.1. Due to different notational conventions we identify $\psi \equiv \hat{\psi}$ and $\varphi \equiv \hat{\varphi}$ in the figure.

2.2. Interpretation and range of a and m

Taking the limit $m \to 0$ in the Kerr metric tensor in different coordinate systems (2.1), (2.8) or (2.10) always results in a locally flat spacetime metric [36], although it is maybe not immediately obvious in all three cases. It can best be seen by taking this limit in (2.10) since $H \to 0$ while l does not depend on m at all, thus leaving us with the standard form of the Minkowski metric $g_{\mu\nu} \to \eta_{\mu\nu}$ for $m \to 0$. Because the Minkowski metric describes flat spacetime, we interpret this limit as the case of vanishing mass, leading to the interpretation that m corresponds to the active gravitational mass of the spacetime. Interestingly, taking the same limit in the Boyer-Lindquist form of the metric (2.1) reveals that the resulting spacetime is topologically non-trivial. In particular, one retains the two asymptotic regions glued together through the disk framed by the ring singularity (which is still a curvature singularity!) [14].
The parameter a can be given meaning by considering the limit $a \to 0$ in either one of the forms of the metric (2.1), (2.8) or (2.9). The result will always be the Schwarzschild metric which describes the spacetime geometry of a stationary (non-rotating) central object of mass m. This can most easily be seen by taking said limit in (2.8), resulting in the Eddington-Finkelstein extension of the Schwarzschild metric and actually giving the corresponding set of coordinates of Kerr spacetime in subsection 2.1.2 its name. Therefore, we will interpret a as the parameter related to rotation.
Although in principle the Kerr metric is a solution to Einstein's field equations for any real parameters a and m, we are really interested only in a certain range of a and m. To begin with, we will require $m > 0$ and $a \neq 0$ since the cases of $m = 0$ and $a = 0$ correspond to the Minkowski metric and the Schwarzschild metric, respectively, and have been studied in more detail on their own [25]. Additionally, the overall sign of a does not change the physical properties of the spacetime. To see this, notice that in Boyer-Lindquist

coordinates the metric is invariant under $(-a, \varphi) \to (a, -\varphi)$. Hence, we only change the direction of rotation which does not produce different physics. One just needs to be consistent with the choice of the "direction of rotation". By inspecting the roots of $\Delta = 0 \Longleftrightarrow r = r_\pm = m \pm \sqrt{m^2 - a^2}$, one can define an upper bound of a. We will see in section 2.3.1 that these two zeros correspond to the event horizon and the Cauchy horizon. For $|a| > m$, the argument of the square-root is negative and we do not have a real solution, thus there exists no horizon and we have a naked singularity. Since naked singularities are deemed to be unphysical, we can finally specify that the region of interest is $0 < |a| \leq m$. In some cases we need to treat the case $|a| = m$ individually because there is a double root for $\Delta = r^2 - 2mr = 0 \Longleftrightarrow r = r_+ = r_- = m$.
Although we keep a and m in all formulae in the current work, we will, unless specified otherwise, set $m = 1$ and vary a in the region $0 < a/m \leq 1$ in all numerical calculations and visualisations. It should be clear that any effects due to rotation are stronger the closer the rotation parameter a is to the critical value 1. One recovers the case $m \neq 1$ by simple rescaling of a. Therefore, we will actually measure distances and time in terms of the black hole mass m in any of the following plots (e.g. r/m, t/m, x/m, u/m, etc.).

2.3. Features of Kerr spacetime

A good starting point to analysing features of a spacetime are singularities occurring in the metric tensor. To differentiate whether some singular set appearing in the metric components is only a coordinate singularity which can be avoided by choosing different coordinates, or a proper curvature singularity which one cannot extend through, it is useful to consider scalar invariants of the spacetime. One such invariant is the Kretschmann scalar $K := R_{\alpha\beta\gamma\delta} R^{\alpha\beta\gamma\delta}$ where $R_{\alpha\beta\gamma\delta}$ denotes the Riemann curvature tensor. Thus this quantity can be interpreted as a measure of curvature. In the well studied Schwarzschild geometry, one uses this Kretschmann scalar (cf. [25] p.822 eq. (31.7))

$$K = \frac{48m^2}{r^6}$$

which clearly diverges as the set $\{r = 0\}$ is approached. Therefore this set is interpreted as a curvature singularity, whereas the event horizon at $r = 2m$ is only regarded as a coordinate singularity which can be extended through by using e.g. Eddington-Finkelstein coordinates [25].
A similar approach concerning the analysis of metric singularities can be taken in the case of Kerr spacetime. The discussion of this analysis is the topic of this section, which will reveal the nature of the ring singularity, the two distinct horizons as well as the so-called ergoregion.

2.3.1. Horizons

As already mentioned in subsection 2.1.1, there is a coordinate singularity in the Boyer-Lindquist form of the Kerr-metric (2.1) at $\Delta = r^2 + a^2 - 2mr = 0$ which corresponds to the set $\{r = r_\pm\}$ with

$$r_\pm = m \pm \sqrt{m^2 - a^2}\ . \tag{2.22}$$

Therefore, Δ is often written as $\Delta = (r - r_+)(r - r_-)$. To determine if this is a curvature singularity, one can, as in the Schwarzschild case, compute the Kretschmann scalar [9][29]

$$\begin{aligned} K &:= R_{\alpha\beta\gamma\delta}R^{\alpha\beta\gamma\delta} \\ &= 48m^2(r^2 - a^2\cos^2(\theta))\frac{\left[(r^2 + a^2\cos^2(\theta))^2 - 16a^2r^2\cos^2(\theta)\right]}{(r^2 + a^2\cos^2(\theta))^6} \qquad (2.23) \\ &= \frac{48m^2}{\hat{r}^3}\,\frac{(2a\cos(\hat{\psi}) + \hat{r})\left(8a^2\cos(2\hat{\psi}) - 4a^2 + 4a\hat{r}\cos(\hat{\psi}) + \hat{r}^2\right)}{\left(4a^2 + 4a\hat{r}\cos(\hat{\psi}) + \hat{r}^2\right)^3}\,, \qquad (2.24) \end{aligned}$$

where the Boyer-Lindquist form of the metric was used in the second equality and the toroidal coordinates were used in the third equality. It can easily be seen that this quantity remains bounded for $r = r_\pm$. We conclude that the singularity at $\Delta = 0$ corresponds to a coordinate singularity only. Indeed by transforming to e.g. Kerr-Schild or Eddington-Finkelstein-like coordinates, this singularity vanishes. For $a = 0$ we find that $r_+ = 2m$ coincides with the event horizon in the Schwarzschild case. Therefore we call r_+ the outer horizon of the black hole or the event horizon, r_- is called the inner horizon or Cauchy horizon. A thorough discussion of the horizons including the general geometric theory behind event and Cauchy horizons can be found in either [6] or [9]. As these analyses require additional technical preliminaries while not assisting the basic physical understanding, it is not of use to reproduce them here.
For a critically rotating black hole with $a = m$, the two horizons coincide at the double root $r_\pm = m$ (for some calculations one needs to treat this case separately). Furthermore, $\Delta = r^2 + a^2 - 2mr = 0$ does not have any real solutions for $r < 0$, and consequently, horizons only exist for $r > 0$. Thus in the region with $r < 0$ one finds a naked singularity. It is this fact that only the region with positive r is accepted to be physical. A further factor for the unphysical nature of the region with $r < 0$ is that it lies under the Cauchy horizon in the sense that one can transfer from one asymptotically flat region to the other by crossing the disk bounded by the ring singularity. In subsection 2.3.2 it will be shown more thoroughly that this singularity is indeed located below the Cauchy horizon r_-.
A pictorial representation of the black hole horizons can be seen in Fig. 2.2.

2.3.2. Ring singularity

It is not so easy to show that the singularity of the Boyer-Lindquist form of the Kerr metric (2.1) corresponding to the set $\{\Sigma = 0 \Longleftrightarrow r = 0\,,\ \theta = \pi/2\}$ is actually a proper curvature singularity and not just a coordinate singularity which could be removed by a more suitable choice of coordinates. This stems from the fact that, although (2.23) being unbound at set $r = 0\,,\ \theta = \pi/2$, one can find curves reaching the singularity where (2.23) stays bounded. For example, consider any curve on which $r^2 = a^2\cos^2(\theta)$, resulting in $K \equiv 0$. An elegant solution to this problem was found by [8] using toroidal coordinates. Following the definition of toroidal coordinates, the defining equation of the singularity becomes $\hat{r} = 0$ for arbitrary $\hat{\varphi}$ and $\hat{\psi}$. The main idea of the proof is to combine the

Kretschmann scalar (2.23) with another scalar invariant, namely

$$\begin{aligned} P &:= \epsilon_{\alpha\beta\mu\nu} R^{\mu\nu}{}_{\gamma\delta} R^{\alpha\beta\gamma\delta} \\ &= -192\, am^2 r \cos(\theta)\, \frac{\left(r^2 - 3a^2\cos^2(\theta)\right)\left(3r^2 - a^2\cos^2(\theta)\right)}{\left(r^2 + a^2\cos^2(\theta)\right)^6} \qquad (2.25) \\ &= -\frac{192\, am^2 \sin(\hat{\psi})}{\hat{r}^3}\, \frac{4a^2 + 3\hat{r}^2 + 12a\hat{r}\cos(\hat{\psi}) + 8a^2\cos(2\hat{\psi})}{\left(4a^2 + 4a\hat{r}\cos(\hat{\psi}) + \hat{r}^2\right)^3}\,, \qquad (2.26) \end{aligned}$$

where again in the second and third line Boyer-Lindquist coordinates and toroidal coordinates are used, respectively. This invariant also has the property of growing without bound on almost every curve approaching the set $r = 0\,,\ \theta = \pi/2$ (or equivalently the set $\hat{r} = 0$ in toroidal coordinates). An exception is e.g. a curve lying entirely in the equatorial plane with $\theta \equiv \pi/2$, on which P is identically zero. The final trick is to combine those two quantities in toroidal coordinates and expand around $\hat{r} = 0$. This again results in a curvature invariant as combinations of scalars are still scalars. The final formula in toroidal coordinates is

$$K^2 + P^2 = \frac{18m^4}{a^6\hat{r}^6}[5 - 3\cos(6\hat{\psi})] + \frac{54m^4}{a^7\hat{r}^5}[-5\cos(\hat{\psi}) + 3\cos(7\hat{\psi})] + O(\hat{r}^{-4})\,. \qquad (2.27)$$

The first term always diverges for $\hat{r} \to 0$ because the second factor of this term would only vanish if $\cos(6\hat{\psi}) = 5/3$, which has no real solutions. Therefore we can see that $K^2 + P^2$ diverges on any curves hitting the ring singularity. This proves that the singularity at $\{\Sigma = 0 \Longleftrightarrow r = 0\,,\ \theta = \pi/2\}$ in Boyer-Lindquist-coordinates actually corresponds to a real curvature singularity.
As already mentioned in subsection 2.1.4, the ring singularity not only serves as the starting point of the definition of toroidal coordinates but also spans the disk which acts as the "portal" between the two asymptotically flat regions in Kerr spacetime, i.e. by crossing this disk the radial component changes its sign. On this disk we thus have $r = 0$, and the polar angle θ defines the distance to the centre of this disk in Kerr-Schild coordinates (x, y, z). By this we mean that on the one hand the case $\theta = 0$ corresponds to the point $(0, 0, 0)$, while on the other hand $\theta = \pi/2$ defines the ring singularity itself which satisfies $x^2 + y^2 = 0$ and $z = 0$.

2.3.3. Ergosphere

Besides the sets where the metric "blows up", there is another very interesting region in the Kerr-spacetime. This peculiar region is called ergosphere and it has the property that there cannot exist any stationary observer within that region. For finding this special region consider a stationary observer whose worldline in Boyer-Lindquist coordinates has the form

$$t \to \gamma(t) = (t,\ r = r_0,\ \theta = \theta_0,\ \varphi = \varphi_0)\,, \qquad (2.28)$$

where quantities with subscript 0 are constant, and with the tangent vector therefore being

$$\dot{\gamma} = \frac{\mathrm{d}\gamma(t)}{\mathrm{d}t} = (1,\ 0,\ 0,\ 0) = \partial_t\,.$$

The worldline of every physical observer must always be timelike, so we require

$$g(\dot{\gamma},\dot{\gamma}) = g(\partial_t,\partial_t) = g_{tt} < 0 \Longleftrightarrow -\left(1-\frac{2mr}{\Sigma}\right) < 0 \ .$$

Therefore, in the region where this inequality is violated, the Killing vector ∂_t responsible for time translations in Boyer-Lindquist coordinates becomes spacelike. This violation happens for

$$r^2 - 2mr + a^2\cos^2(\theta) < 0 \ ,$$

defining boundaries of a specific region in spacetime, which are given by

$$\mathring{r}_\pm = m \pm \sqrt{m^2 - a^2\cos^2(\theta)} \ . \tag{2.29}$$

Consequently, in the region $\mathring{r}_- < r < \mathring{r}_+$ an observer cannot "stand still" in the sense that they follow the worldline of a stationary observer. Every object within that region gets dragged with the rotation of the black hole. It is of interest that the outer boundary of the ergosphere $\mathring{r}_+$ is bigger than the outer horizon r_+, which means that there exists a region which one can physically enter, be dragged with the rotation of the black hole, and yet still escape to infinity. This intermediate region is known as the ergoregion and that it must exist can easily be deduced by comparing the defining equations of the horizons (2.22) and of the ergosphere (2.29) using the fact that $\cos(\theta) < 1$ in the domain of definition of the azimuthal coordinate $0 < \theta < \pi$. By doing so one can verify the ordering $\mathring{r}_- \leq r_- \leq r_+ \leq \mathring{r}_+$. The first and the last equality is satisfied on the axis of symmetry $\theta = 0$ and in the Schwarzschild limit $a = 0$. Furthermore, the inner boundary surface at $\mathring{r}$ intersects the ring singularity at $r = 0$ in the equatorial plane $\theta = \pi/2$. A visualisation of the boundaries where these features are clearly visible can be found in Fig. 2.2.
The ergoregion ($r_+ < r < \mathring{r}_+$) is of special interesting due to the so-called Penrose-process [28], with which one can in principle extract rotational energy from a black hole.

2.3.4. Causality violating region/Carter's time machine

The last feature resulting directly from the metric tensor is the so-called Carter's time machine region. It is defined as the part of spacetime where the Killing vector ∂_φ (in Boyer-Lindquist coordinates) becomes timelike, i.e. the region where

$$\begin{aligned} 0 > g(\partial_\varphi,\partial_\varphi) &= g_{\varphi\varphi} \\ &= \frac{(r^2+a^2)^2 - (r^2-2mr+a^2)a^2\sin^2\theta}{r^2+a^2\sin^2\theta}\ \sin^2\theta \\ &= \frac{a^4 + a^2\cos(2\theta)(r^2-2mr+a^2) + a^2r(2m+3r) + 2r^4}{a^2\cos(2\theta)+a^2+2r^2}\ \sin^2\theta \ . \end{aligned} \tag{2.30}$$

Upon closer analysis (see e.g. [9]) one can show that for a positive mass parameter $m > 0$ this corresponds to the set

$$\mathcal{V} = \{r < 0 \ ,\ \cos(2\theta) < -\frac{a^4 + 2a^2mr + 3a^2r^2 + 2r^4}{a^2(r^2-2mr+a^2)} \ ,\ \Sigma \neq 0 \ ,\ \sin\theta \neq 0\} \ , \tag{2.31}$$

which can be shown to be a non-empty set. Furthermore, it is not complicated to see that any two points inside $\mathcal{V}$ can be connected by a future-directed causal curve. A short proof

of this statement can be found in [9]. A direct consequence of this is that any two points below the inner horizon at $r = r_-$ can be connected via a future-directed causal curve, making it possible to "travel through time", hence the name Carter's time machine.
The assumption for deriving the set $\mathcal{V}$ was that $m > 0$. As already discussed before in section 2.1.1, one can describe the asymptotically flat region for $r < 0$ equivalently by leaving $r > 0$ and considering $m < 0$. Thus, if we assume $m < 0$ the causality violating region would be present for $r > 0$.

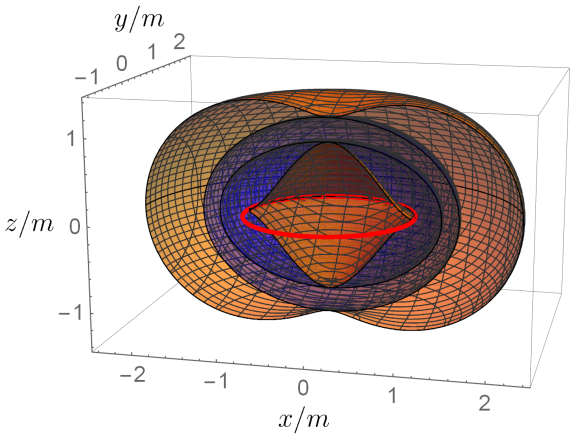

Figure 2.2.: Visualization of the horizons (blue), the ergosphere (orange) and the ring singularity (red). The two blue surfaces correspond to the horizons, the inner one being the Cauchy horizon at $r = r_-$ while the outer one is the event horizon at $r = r_+$. The outermost/innermost sphere in orange corresponds to the inner and outer boundary of the ergosphere at $r = \mathring{r}_-$ and $r = \mathring{r}_+$, respectively. The red ring in the middle depicts the set of unbound curvature, the so-called ring singularity. The ergoregion with $r_+ < r < \mathring{r}_+$ is clearly visible. This plot is made using Kerr-Schild coordinates with parameter $a/m = 0.99$.

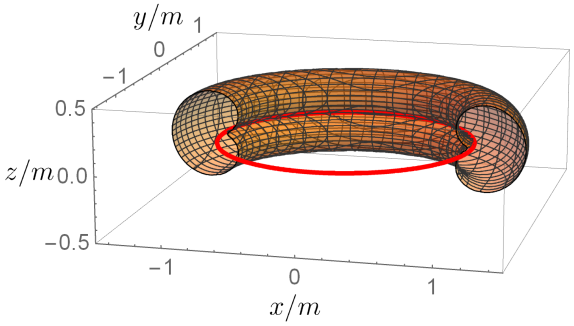

Figure 2.3.: Boundary of the causality violating region in Kerr-Schild coordinates. Inside the illustrated region one finds that $g_{\varphi\varphi} < 0$, and consequently there exist closed timelike curves. This fact can be used to "travel through time", i.e. connect any two spacetime points with $r < r_-$ via a future-directed causal curve. The ring singularity is depicted in red. These plots were made with black hole parameter $a = 0.99$.

2.4. Projection diagrams

This short section is meant to give the reader (familiar with conformal Carter-Penrose-diagrams) a feeling for the global structure of Kerr spacetime. Therefore, this section will be kept mathematically rather simple – for the precise mathematical definitions and implications, the interested reader is referred to [7] (on which this section is based on).
The basic idea behind projection diagrams is to investigate the causal structure of a spacetime. For this purpose, the spacetime is projected onto (1+1)-dimensional Minkowski spacetime. To do this one defines a projection diagram as follows:

Let $(\mathcal{M}, g)$ be a smooth spacetime, and let $\mathbb{R}^{1,n}$ denote the $(n+1)$-dimensional Minkowski spacetime. A projection diagram *is a pair $(\pi, \mathcal{U})$, where $\mathcal{U} \subset \mathcal{M}$ is an open, non-empty set and where $\pi : \mathcal{M} \to \mathcal{W}$ is a continuous map, differentiable on an open dense set, from $\mathcal{M}$ onto $\pi(\mathcal{M}) =: \mathcal{W} \subset \mathbb{R}^{1,1}$, such that π is a smooth submersion on $\mathcal{U}$. Furthermore it needs to hold that:*

1. *for every smooth timelike curve $\sigma \subset \pi(\mathcal{U})$ there exists a smooth timelike curve γ in $(\mathcal{U}, g)$ such that $\sigma = \pi \circ \gamma$;*
2. *the image $\pi \circ \gamma$ of every smooth timelike curve $\gamma \subset \mathcal{U}$ is a timelike cuve in $\mathbb{R}^{1,1}$.*

Condition 1 in the definition ensures that it is possible to investigate the causal structure of the original spacetime $\mathcal{M}$ by examining the causal structure of the projection diagram $\pi(\mathcal{U})$. This together with the second condition is tailored such that causality relations on $\pi(\mathcal{U})$ resemble the causality relations on $\mathcal{M}$ as closely as possible.
Additionally, we need to keep in mind that these conditions force us to invoke stable causality of $\mathcal{U}$, i.e. the existence of a time function on $\mathcal{U}$. For that reason we need to exclude causality violating regions from the projection diagrams – hence, in the case of Kerr spacetime we need to exclude Carter's time machine (discussed in previous section) from the projection diagram. In order to avoid possible problems, one "cuts out" a region of maximal size from the spacetime corresponding to this causality violating region. What is meant by this is the following: we require that $g_{\varphi\varphi} > 0$ everywhere in $\mathcal{M}$. By noting that both the denominator in (2.30) as well as $\sin^2\theta$ are non-negative, this inequality reduces to $a^4 + a^2\cos(2\theta)(r^2 - 2mr + a^2) + a^2 r(2m + 3r) + 2r^4 > 0$. Assuming $r < 0$, the left-hand side of this inequality is minimal in the case where $\cos(2\theta) = -1 \iff \theta = \pi/2$. By choosing this value, we ensure to not miss any part of the causality violating region. Simplifying this inequality with $\theta = \pi/2$ we arrive at

$$r(a^2(2m + r) + r^3) > 0 \,,$$

which defines the boundaries of the region we need to exclude from the whole Kerr spacetime in order to create the projection diagram. The upper boundary is simply $\hat{r}_+ = 0$ (corresponding to the disk bounded by the ring singularity), whereas the lower boundary is defined by

$$\hat{r}_- = \frac{\sqrt[3]{\sqrt{3(a^6 + 27a^4m^2)} - 9a^2m}}{3^{2/3}} - \frac{a^2}{\sqrt[3]{3}\sqrt[3]{\sqrt{3(a^6 + 27a^4m^2)} - 9a^2m}} \,.$$

Summarising, to preserve stable causality throughout Kerr spacetime (the spacetime we want to project onto $(1+1)$-dimensional Minkowski spacetime), we need to exclude the region $\hat{r}_- < r < \hat{r}_+ = 0$ from the projection.

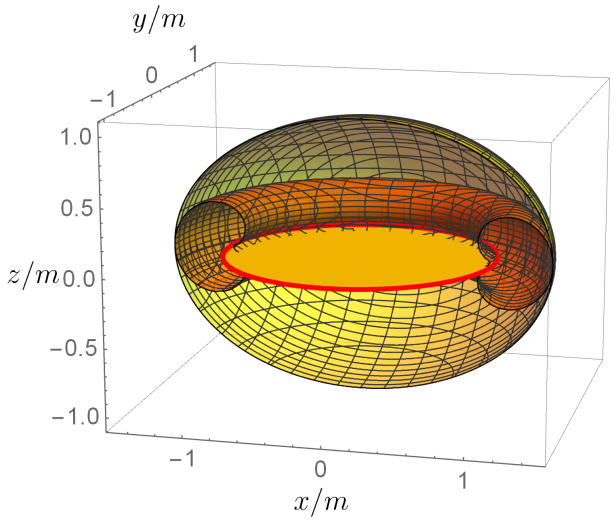

Figure 2.4.: The boundary of the causality violating region at $r < 0$ (orange) and the extended region which is excluded from the projection diagram (bounded by the yellow surfaces). The ring singularity is depicted in red. This plot is made using Kerr-Schild coordinates with parameter $a = 0.99$.

By exclusion of the region $\hat{r}_- < r < \hat{r}_+$, one can apply the definition of the projection diagram and get a representation of Kerr spacetime as a $(1+1)$-dimensional Minkowski spacetime which reflects the causal structure as close as possible. The resulting projection diagrams can be found in Fig. 2.5 and Fig. 2.6.
In the slowly rotating Kerr spacetime ($0 < a/m < 1$), one has two distinct roots of Δ and hence two different horizons. Because these horizons are null surfaces, they will divide the resulting projection diagram in three distinct regions: (I) one outside the outer/event horizon $r > r_+$, (II) one between the horizons $r_- < r < r_+$, and (III) one below the inner/Cauchy horizon $r < r_-$. For regions (I) and (III) there always exist a "mirror world" which is a copy of the corresponding region. These three regions can be seen in Fig. 2.5a. In (I) one can find spatial infinity $r = +\infty$ as well as (future and past) timelike infinity. Going towards the future direction in this region (up), one necessarily reaches either future timelike infinity, spatial infinity at $r = +\infty$, or the outer/event horizon which one needs to cross to get to (II). Being an intermediate region not containing any infinities, (II) can (in the future direction) only be left via the inner/Cauchy horizon to finally reach (III), i.e. it is a black hole region. Region (III) of the projection diagram is more complicated because in addition to spatial infinity at $r = -\infty$ and (future and past) timelike infinity, it also contains the causality violating region which is to be excluded from the projection diagram (indicated in grey with boundaries at $\hat{r}_\pm$). In this region one again has three different possible paths: either go to future timelike infinity, go to spatial infinity at $r = -\infty$, or again cross the inner horizon to get to another region between the horizons which is similar to (II) except it can in the future direction only be left via the outer horizon, thus corresponding to a white hole region. Note that since worldlines of physical observers

can only go upwards in the diagram and the horizons are null hypersurfaces, such an observer can never reach the same region twice once they leave it. To be able to continue a path which repeatedly crosses the horizons, one needs to extend the projection diagram of Fig. 2.5a by infinitely many copies of regions (I), (II), and (III). Furthermore, it needs to be mentioned that it is possible to connect a point in spacetime with $r > 0$ to a point with $r < \hat{r}_-$ via a curve along which causality is not problematic (i.e. a curve which does not traverse the causality violating region). This should be clear from Fig. 2.3 as it is possible to cross the disk without crossing the causality violating region in orange. Only by excluding the extended region $\hat{r}_- < r < \hat{r}_+$ from the projection diagram (region bounded by yellow surfaces in Fig. 2.4) this is no longer possible.
Fig. 2.5b shows the projection diagram of the critically spinning Kerr spacetime with $a/m = 1$, in which case Δ has one real double root at $r_+ = r_- = m$. Consequently, (II) vanishes completely and one is left with (I) and (III).
Lastly, Fig. 2.6 shows the projection diagram of Kerr spacetime with $a/m > 1$. For this parameter range Δ has no real roots, resulting in a naked singularity also in the region $r > 0$. This absence of horizons results in the merger of (I) and (III) which includes both spatial infinities at $r = \pm\infty$, the future and past timelike infinities, as well as the causality violating region.

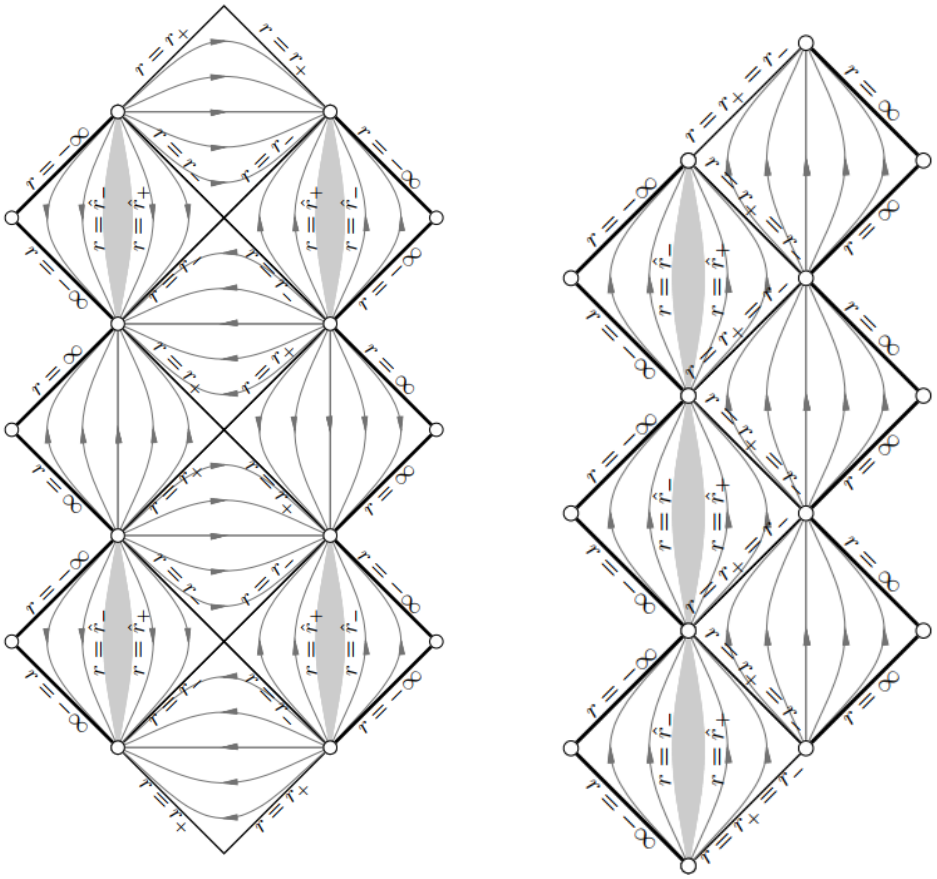

Figure 2.5.: Projection diagrams for (a) the slowly spinning Kerr case $0 < a/m < 1$ with two zeros of Δ, and (b) the extreme Kerr case $a/m = 1$ with a double root of Δ at $r = r_+ = r_-$. The figure is taken from [7].

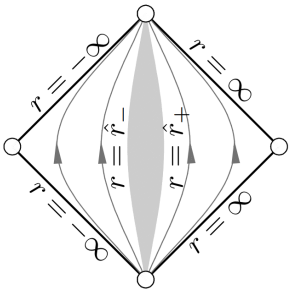

Figure 2.6.: Projection diagram of Kerr spacetime for $a/m > 1$. Only one distinct region is present due to Δ having no real roots for overcritical rotation. The figure is taken from [7].

3. Geodesics in Kerr spacetime

In general relativity, a geodesic is the shortest connection between two points in spacetime, generalizing the meaning of a straight line to curved manifolds. Every test particle, i.e. an object with negligible mass, only experiencing gravitation and no other external forces acting on it, must follow a geodesic curve. This geodesic is described by a set of equations of motion, which are given by

$$\frac{\mathrm{d}^2 x^\mu}{\mathrm{d}s^2} + \Gamma^\mu_{\alpha\beta} \frac{\mathrm{d}x^\alpha}{\mathrm{d}s} \frac{\mathrm{d}x^\beta}{\mathrm{d}s} = 0 \,,$$

regardless of the spacetime the particle moves in. Here s denotes some affine parameter along the geodesic and $\Gamma^\mu_{\alpha\beta}$ are the Christoffel symbols. This is a set of coupled second order differential equations. To reduce this to a system of first order differential equations and solve it by integration, it is necessary to find preserved quantities along the geodesic, called constants of motion (sometimes also called first-integrals).
In Schwarzschild geometry, this is rather straight forward, whereas in Kerr spacetime this is conceptually more intricate. The first one to successfully formulate the equations of motion as a system of first order equations was Brandon Carter in 1968 [5]. Building upon this, many properties of geodesics were found, e.g. [17] or [18]. This section aims at deriving the equations of motion of a test particle, thus preparing the reader conceptually for what will follow in the rest of this thesis. For historical reasons, we will follow the derivation by [5] using Eddington-Finkelstein-like coordinates (2.4) and (2.5) with $\nu_r = -1$, although it would probably make more sense pedagogically to follow e.g. [6] and derive them in Boyer-Lindquist coordinates. The reason is that we want to solve the geodesic equations in the general Eddington-Finkelstein-like coordinates (where the value of ν_r is not specified yet). Therefore, we will state the equations of motion in three different coordinate systems: Eddington-Finkelstein-like coordinates with $\nu_r = -1$, Eddington-Finkelstein-like coordinates with general ν_r, and Boyer-Lindquist coordinates. In the case of global vortical null geodesics, both well known and some new found features are described and analysed.

3.1. Geodesic equations of motion

As already stated, Brandon Carter was the first one being able to state the equations of motion for a test particle in Kerr spacetime as a system of first order differential equations [5], thus allowing to solve them by integration. In his paper, Carter did not use the generic Kerr metric, but rather the more general Kerr-Newman metric, where the black hole as well as the test particle have an electric charge. This does not hinder us to use these equations since the Kerr case is recovered by taking the limit of vanishing charges. For what follows, we will already take this limit wherever possible to keep the formulas simple. When considering vanishing charges, the metric tensor Carter used was cast in Eddington-Finkelstein-like coordinates (2.8) with $\nu_r = -1$.

One can calculate the equations of motion by considering the Lagrangian

$$\mathcal{L} = \frac{1}{2} g_{\alpha\beta} \dot{x}^\alpha \dot{x}^\beta \,, \tag{3.1}$$

where the dot represents differentiation with respect to some affine parameter s along the geodesic. To get parametrisation by proper time $\tilde{\tau}$, consider the relation of s to $\tilde{\tau}$

$$\tilde{\tau} = \mu s \,. \tag{3.2}$$

Equivalently, one can require the normalisation condition

$$g_{\alpha\beta} \dot{x}^\alpha \dot{x}^\beta = -\mu^2 \,. \tag{3.3}$$

The parameter μ is interpreted as the mass of the test particle, for timelike geodesics this takes the value $\mu^2 = +1$ while for null geodesics this takes the value $\mu^2 = 0$ (note that a spacelike geodesic must have imaginary mass $\mu = i$). μ will serve as one constant of motion. By switching to the Hamiltonian formalism and introducing the momenta $p_\alpha = g_{\alpha\beta}\dot{x}^\beta$, Carter calculates p_u, p_ψ, p_r, and p_θ. It is clear from the start that p_u and p_ψ correspond to two additional constants of motion since ∂_u and ∂_ψ are Killing vectors in Eddington-Finkelstein-like coordinates. Thus we have the two constants

$$p_u = -E \,, \tag{3.4}$$

$$p_\psi = L \,, \tag{3.5}$$

where E corresponds to the constant concerning the conservation of energy and L corresponds to conservation of angular momentum in the azimuthal direction ψ.
Hereafter, one additional constant of motion is needed which Carter finds by using the separability of the Hamilton-Jacobi equation. This constant K is known as Carter's constant and is defined by

$$K = p_\theta^2 + \left(aE \sin\theta - \frac{L}{\sin\theta} \right)^2 + a^2 \mu^2 \cos^2\theta \,, \tag{3.6}$$

where p_θ denotes the angular momentum in polar direction. With this he was able to state the Jacobi action and by differentiating with respect to the constants of motion K, μ, E, and L he derived the integral version of the equations of motion in Eddington-Finkelstein coordinates (with $\nu_r = -1$)

$$\int_{\theta_s}^{\theta_o} \frac{\mathrm{d}\theta}{\sqrt{\Theta(\theta)}} = \int_{r_s}^{r_o} \frac{\mathrm{d}r}{\sqrt{R(r)}} \,, \tag{3.7}$$

$$s = \int_{\theta_s}^{\theta_o} \frac{a^2 \cos^2\theta \, \mathrm{d}\theta}{\sqrt{\Theta(\theta)}} + \int_{r_s}^{r_o} \frac{r^2 \, \mathrm{d}r}{\sqrt{R(r)}} \,, \tag{3.8}$$

$$\psi = \int_{\theta_s}^{\theta_o} \frac{-(aE - \frac{L}{\sin^2\theta}) \, \mathrm{d}\theta}{\sqrt{\Theta(\theta)}} + \int_{r_s}^{r_o} \frac{a}{\Delta} \left(1 + \frac{P(r)}{\sqrt{R(r)}} \right) \mathrm{d}r \,, \tag{3.9}$$

$$u = \int_{\theta_s}^{\theta_o} \frac{-a(aE \sin^2\theta - L) \, \mathrm{d}\theta}{\sqrt{\Theta(\theta)}} + \int_{r_s}^{r_o} \frac{r^2 + a^2}{\Delta} \left(1 + \frac{P(r)}{\sqrt{R(r)}} \right) \mathrm{d}r \,, \tag{3.10}$$

where Δ is defined as in (2.3) and where he defined the quantities

$$Q = K - (L - aE)^2 \,, \tag{3.11}$$

$$\Theta(\theta) = Q - \cos^2\theta \left[a^2(\mu^2 - E^2) + \frac{L^2}{\sin^2\theta} \right] \,, \tag{3.12}$$

$$P(r) = E(r^2 + a^2) - La \,, \tag{3.13}$$

$$R(r) = P(r)^2 - \Delta(\mu^2 r^2 + K) \,. \tag{3.14}$$

Note that Carter made a sign mistake in his calculation: he flipped the sign of P in his paper from equation (60) onwards – each term containing P should change its sign. Corrected versions of the equations (in Boyer-Lindquist coordinates) can also be found in e.g. [6] or [27].
The quantity Q is simply another constant of motion which can serve as a replacement for K since it is composed of the other constants and thus is also constant along a geodesic. Q is also called Carter's constant and in this thesis we will refer to Q when mentioning Carter's constant. $\Theta(\theta)$ and $R(r)$ are called the polar and radial potential, respectively. Furthermore, in (3.7)-(3.10) the signs of $\sqrt{\Theta(\theta)}$ and $\sqrt{R(r)}$ may be chosen independently but consistently. For keeping track of this sign, we will encode it in a prefactor, i.e. $\sqrt{\Theta(\theta)} = \nu_\theta \sqrt{\Theta(\theta)}$ and $\sqrt{R(r)} = \nu_r \sqrt{R(r)}$. In the integral form (3.7) the polar motion in θ is clearly coupled to the radial motion in r. For a "cleaner" version of the equations of motion, one can express them as a coupled system of first-order differential equations

$$\Sigma\, \dot{r} = \nu_r \sqrt{R(r)} \,, \tag{3.15}$$

$$\Sigma\, \dot{\theta} = \nu_\theta \sqrt{\Theta(\theta)} \,, \tag{3.16}$$

$$\Sigma\, \dot{\psi} = -\left(aE - \frac{L}{\sin^2\theta} \right) + \frac{a}{\Delta}(\nu_r \sqrt{R(r)} + P(r)) \,, \tag{3.17}$$

$$\Sigma\, \dot{u} = -a(aE\sin^2\theta - L) + \frac{r^2 + a^2}{\Delta}(\nu_r \sqrt{R(r)} + P(r)) \,, \tag{3.18}$$

where the dot denotes again the differentiation with respect to an affine parameter s. The sign of the square roots ν_r and ν_θ also dictates the starting direction of the geodesic – e.g. for $\nu_r = +1$ the geodesics radial coordinate initially increases with increasing affine parameter s along the geodesic. We therefore call this case initially outgoing. The case $\nu_r = -1$ is called initially ingoing. $\nu_\theta = \pm 1$ corresponds to the polar angle initially increasing/decreasing. These equations are still coupled because Σ on the left-hand side is defined as in (2.3) and therefore dependent on both r and θ.
It can sometimes be helpful to cast the equations of motion in Boyer-Lindquist coordinates, in which they take the form [6]

$$\Sigma\, \dot{r} = \nu_r \sqrt{R(r)} \,, \tag{3.19}$$

$$\Sigma\, \dot{\theta} = \nu_\theta \sqrt{\Theta(\theta)} \,, \tag{3.20}$$

$$\Sigma\, \dot{\varphi} = \frac{a}{\Delta}(2mrE - aL) + \frac{L}{\sin^2\theta} \,, \tag{3.21}$$

$$\Sigma\, \dot{t} = \frac{r^2 + a^2}{\Delta}((r^2 + a^2)E - aL) + a(L - aE\sin^2\theta) \,. \tag{3.22}$$

3.1.1. Equations of motion for null geodesics and Mino time

The main goal of this thesis is, in the most general notion, concerned with simulating the optical appearance of Kerr black holes. Accordingly, we are interested in null geodesics, i.e. geodesics with constant of motion $\mu = 0$ describing the motion of photons. In this case only

$$\lambda = \frac{L}{E} \,, \tag{3.23}$$

$$\eta = \frac{Q}{E^2} \tag{3.24}$$

are independent, meaning that only the sign of E is important. In any numerical calculations, unless specified otherwise, we will set $E = 1$. This restriction to positive energy $E > 0$ is on the one hand possible because of remark 4.1.2 in [27] and the fact that we want to investigate geodesics which reach the region where ∂_t is timelike. Accordingly, the energy does not vanish, i.e. $E \neq 0$. On the other hand, we can reparametrise the geodesic such that the energy is normalised $E = 1$ and thus λ is the azimuthal angular momentum of the geodesic.
In addition to these new constants we take advantage of another parameter along the geodesic which makes it easier to solve the equations of motion for null geodesics numerically as well as analytically. Such a new parameter τ along the geodesic was first introduced by Mino and is consequently called "Mino time" [24]. It is defined via

$$\mathrm{d}\tau = \frac{E}{\Sigma}\,\mathrm{d}s \,. \tag{3.25}$$

By dividing both sides in the equations of motion in Boyer-Lindquist coordinates (3.19)-(3.22) by E and using the reparametrisation (3.25) as well as the newly defined constants (3.23) and (3.24) one arrives at

$$\frac{\mathrm{d}r}{\mathrm{d}\tau} = \nu_r \sqrt{R(r)} \,, \tag{3.26}$$

$$\frac{\mathrm{d}\theta}{\mathrm{d}\tau} = \nu_\theta \sqrt{\Theta(\theta)} \,, \tag{3.27}$$

$$\frac{\mathrm{d}\varphi}{\mathrm{d}\tau} = \frac{a}{\Delta}(2mr - a\lambda) + \frac{\lambda}{\sin^2\theta} \,, \tag{3.28}$$

$$\frac{\mathrm{d}t}{\mathrm{d}\tau} = \frac{r^2 + a^2}{\Delta}(r^2 + a^2 - a\lambda) + a(\lambda - a\sin^2\theta) \,, \tag{3.29}$$

with the new radial and angular potentials

$$R(r) = (r^2 + a^2 - a\lambda)^2 - \Delta(\eta + (\lambda - a)^2) \,, \tag{3.30}$$

$$\Theta(\theta) = \eta + a^2\cos^2\theta - \lambda^2\frac{\cos^2\theta}{\sin^2\theta} \,, \tag{3.31}$$

where we already used $\mu = 0$ so that (3.26)-(3.29) are the equations of motion for a null geodesic in Boyer-Lindquist coordinates. It is obvious that these equations are problematic at the horizons since the Boyer-Lindquist coordinates become singular there. In order to study geodesics crossing the horizons, it is necessary to transform to another coordinate

system. For that task we will choose general Eddington-Finkelstein-like coordinates, defined in subsection 2.1.2. These coordinates are more general than the ones used by Carter in the sense that $\nu_r = \pm 1$ can obtain both values, whereas Carter used these coordinates with $\nu_r = -1$. In these coordinates the equations of motion take the form

$$\frac{\mathrm{d}r}{\mathrm{d}\tau} = \nu_r \sqrt{R(r)} \,, \tag{3.32}$$

$$\frac{\mathrm{d}\theta}{\mathrm{d}\tau} = \nu_\theta \sqrt{\Theta(\theta)} \,, \tag{3.33}$$

$$\frac{\mathrm{d}\psi}{\mathrm{d}\tau} = \frac{a}{\Delta}(2mr - a\lambda - \sqrt{R(r)}) + \frac{\lambda}{\sin^2\theta} \,, \tag{3.34}$$

$$\frac{\mathrm{d}u}{\mathrm{d}\tau} = \frac{r^2 + a^2}{\Delta}(r^2 + a^2 - a\lambda - \sqrt{R(r)}) + a(\lambda - a\sin^2\theta) \,. \tag{3.35}$$

The extra term $\sqrt{R(r)}$ counteracts the divergent part at the horizons. This is most easily shown to hold for null geodesics. To this end, we expand the square root of the radial potential for small values of Δ, giving

$$\sqrt{R(r)} \approx \sqrt{(r^2 + a^2 - a\lambda)^2} + \frac{\Delta(\eta + (\lambda - a)^2)}{2\sqrt{(r^2 + a^2 - a\lambda)^2}} + \mathcal{O}\left((\Delta^2)\right) \,. \tag{3.36}$$

Vortical null geodesics are further restricted by $|\lambda| < a$ [17], ensuring $r^2 + a^2 - a\lambda \geq 0$ for all values of r and a. With this, (3.36) becomes

$$\sqrt{R(r)} \approx r^2 + a^2 - a\lambda) + \frac{\Delta(\eta + (\lambda - a)^2)}{2(r^2 + a^2 - a\lambda)} + \mathcal{O}\left((\Delta^2)\right) \,. \tag{3.37}$$

Inserting this approximation into (3.34) leads to

$$\frac{\mathrm{d}\psi}{\mathrm{d}\tau} \approx \frac{a}{\Delta}\left(2mr - r^2 - a^2 - \frac{\Delta(\eta + (\lambda - a)^2)}{2(r^2 + a^2 - a\lambda)}\right) + \frac{\lambda}{\sin^2\theta} + \mathcal{O}\left(\Delta\right) \,. \tag{3.38}$$

After the insertion of $\Delta = r^2 + a^2 - 2mr$ we arrive at

$$\frac{\mathrm{d}\psi}{\mathrm{d}\tau} \approx a\left(-1 - \frac{\eta + (\lambda - a)^2}{2(r^2 + a^2 - a\lambda)}\right) + \frac{\lambda}{\sin^2\theta} + \mathcal{O}\left(\Delta\right) \,, \tag{3.39}$$

which is clearly bounded for $\Delta \to 0$. A similar calculation shows that also (3.35) stays bounded at the horizon.

Equations (3.32)-(3.35) also unveil the reason for the factor ν_r in the coordinate transformation from Boyer-Lindquist to Eddington-Finkelstein-like coordinates. Without this additional factor in the transformation, there would be a factor of ν_r in front of $\sqrt{R(r)}$ in the equations of motion (3.34) and (3.35) which would cause that they are still divergent in the case of $\nu_r = -1$ since in this case another divergent part would be added. When including ν_r in the transformation, the sign cancels out and we always subtract the divergent part. In this sense we need to treat ingoing and outgoing geodesics differently by choosing coordinates adapted to the initial radial direction, i.e. if the geodesic is initially ingoing or outgoing (cf. [29] section 5.3.6).

The form (3.32)-(3.35) of the equations of motion is especially useful because of two facts. Firstly, with it we can solve for $(r(\tau), \theta(\tau), \psi(\tau), u(\tau))$ numerically rather easily.

Secondly, as was similarly done by Gralla [17] (using Boyer-Lindquist coordinates), it enables us to find explicit antiderivatives of these integrals by using elliptic integrals and elliptic functions. In comparison to the solutions found by Gralla, solutions obtained using (3.32)-(3.35) will be viable globally, meaning that the geodesics can cross horizons in both directions without problems. A discussion of both the analytic and numeric solutions to these equations can be found in chapter 4.

3.2. Global vortical null geodesics

There is an interesting subclass of geodesics called vortical geodesics, characterised by the condition $Q < 0$ or equivalently $\eta < 0$. One can discuss these special geodesics in a very general case, but because we are only concerned with null geodesics, this section is devoted solely to vortical null geodesics and some of their features. For the main part this will include an analysis of the radial and angular potentials (3.30) and (3.31). A discussion of vortical timelike geodesics can be found in [27].

3.2.1. Radial motion

Let us begin by analysing the radial motion of null geodesics, determined by equation (3.26). When we insert (2.3) and (3.30) into (3.26) it becomes

$$\frac{\mathrm{d}r}{\mathrm{d}\tau} = \nu_r \sqrt{(r^2 + a^2 - a\lambda)^2 - (r^2 + a^2 - 2mr)(\eta + (\lambda - a)^2)}\,. \tag{3.40}$$

It should be clear that the radial motion is restricted to the case where the radicand in (3.40) is non-negative. Otherwise the solution for the radial motion would become complex, which is to avoid for physically acceptable geodesics.

r-λ-plots

For a further analysis of this term let us fix the black hole mass $m = 1$ and inspect different cases of the rotation parameter $0 < a < 1$. This leaves us with three undefined quantities in the radicand, the radius r and the two constants of motion λ and η. A first qualitative analysis of how the case of vortical null geodesic differs from the general case is possible by distinguishing three different cases: $\eta < 0$, $\eta = 0$ and $\eta > 0$. For the purpose of visualisation, we will consider $\eta \in \{0, \pm 0.1\}$. This fixing of η allows us to parametrically plot the radicand $R(r)$ in the r-λ-plane, visualising not the exact value of it but rather its sign, i.e. the forbidden (negative radicand) and allowed (positive radicand) regions.
The simplest and most well known instance is the Schwarzschild case with $a = 0$, so let us start with this. Fig. 3.1 represents the r-λ-plot of the three cases for η as described. The grey areas are the forbidden regions while the white areas are the physically allowed ones, separated by the boundary at which $R(r)$, and consequently also the radial velocity $\mathrm{d}r/\mathrm{d}\tau$, vanishes. The dashed line corresponds to the radial location of the Schwarzschild horizon. Recall that in the Schwarzschild case we only have one horizon $r = r_+ = 2m$ while the inner horizon vanishes at the singularity $r = r_- = 0$. All geodesics must be contained completely in the allowed area. Since λ is a constant of the motion, any geodesic can move only along a horizontal path in these plots by changing its radial coordinate.

Whether this path is left- or right-moving depends on the sign ν_r: negative ν_r corresponds to a left-moving, positive ν_r corresponds to a right-moving geodesic. Regardless of the initial radial direction, whenever the geodesic hits the boundary of one of the forbidden areas (grey), since it cannot penetrate through, it must be reflected. This reflection is accompanied by a flip of the sign of ν_r.
Therefore, as can be seen in Fig. 3.1, in the Schwarzschild case any initially ingoing geodesic starting at $r > 3m$ will eventually hit a forbidden region and consequently be reflected at some point in time to end up at $r \to +\infty$, regardless of the sign of η and also for all λ. There are three cases one needs to distinguish. The first one being the one for large angular momenta. Notice that since the plots in Fig. 3.1 are symmetric about the abscissa we can define this by requiring $|\lambda| > \lambda_c$, where λ_c is defined by the extremal points of the curve with vanishing radial potential outside the horizon, i.e. the minimum and maximum of the curve bounding the grey area, given by the two equations $R(r) = 0$ and $\mathrm{d}R(r)/\mathrm{d}r = 0$. One can calculate that these conditions are satisfied at $r = 3m$ for $\lambda_c = \pm\sqrt{27m^2 - \eta}$. This case of large angular momentum corresponds to geodesics which are reflected in the black hole exterior region, i.e. before they cross the event horizon. It is these null geodesics which ultimately determine what an observer outside of the black hole would be able to perceive, i.e. these geodesics correspond to photons which start their journey at some source outside the black hole with $r_s > 3m$ and finally, either by being deflected or directly, reach the observers eye/photon detector, also outside the horizon. If the source of these geodesics is in the range $0 < r < 3m$ the geodesic is bound and crosses the event horizon indefinitely. Another case which has to be discussed is the one for small angular momenta $|\lambda| < \lambda_c$. Initially ingoing geodesics in this angular momentum range will cross the Schwarzschild horizon at $r = 2m$ and will get reflected at $r = 0$. Because it is impossible for the geodesic to cross the horizon a second time in the opposing direction, this outwards motion needs to lead into a different region of spacetime where the central object now acts not as a black hole but rather as a white hole. For an observer outside the horizon in the original region of spacetime, these photons would be lost and would thus correspond to the black holes shadow, illuminated by geodesics with $|\lambda| > \lambda_c$. The smallest amount of geodesics belongs to the third case where $|\lambda| = \lambda_c$. At $r = 3m$ these become trapped and form the so-called photosphere. Initially ingoing trajectories are neither reflected, nor let through to cross the horizon but rather stay at $r = 3m$ indefinitely; similar for initially outgoing ones. Note that regardless of the value of η this photon sphere is located at $r = 3m$. For an observer outside of the horizon, this would be the exact boundary of the black hole shadow (unless there is a light source present at $2m < r_s < 3m$).

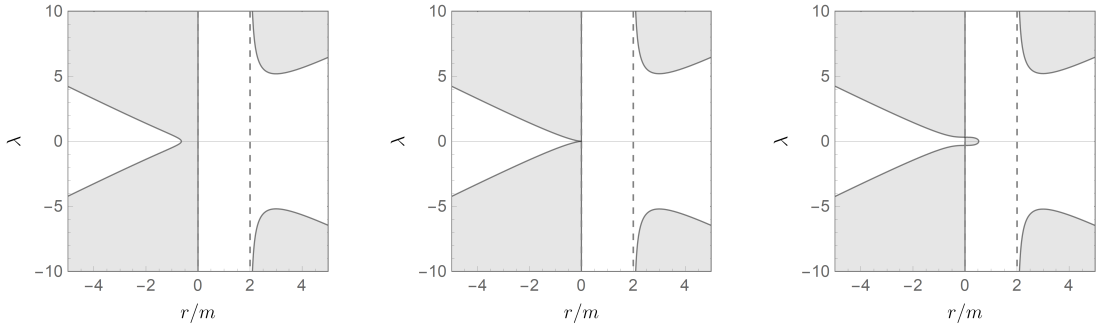

(a) $\eta > 0$ (b) $\eta = 0$ (c) $\eta < 0$

Figure 3.1.: r-λ-plot of null geodesics in the Schwarzschild case $a = 0$. The dotted line is the Schwarzschild horizon at $r = 2m$.

Moving on to the more interesting case of the Kerr metric with non-vanishing rotation $a/m \neq 0$, new features start to appear in the r-λ-plot. An example can be found in Fig. 3.2 where we chose mass $m = 1$ and rotation $a/m = 0.9$ for the black hole. Firstly, note that these plots are not symmetric about the abscissa any more and furthermore both horizons at $r = r_- \approx 0.56m$ and at $r = r_+ \approx 1.44m$ are visible. By approaching critical rotation this skewing effect gets enhanced and the horizons merge together at $r = m$. In the cases where $\eta \geq 0$, the qualitative behaviour is similar to the Schwarzschild case in the sense that there are geodesics which cross both horizons and are reflected outwards into a different region of spacetime. Such a path can be easily drawn in the projection diagram Fig. 2.5a of section 2.4 which visualises the global properties of the spacetime. This would correspond to a geodesic starting in (I), crossing (II) and going into (III), and then being reflected and going to a copy of (II) and out to a copy of (I) again. A qualitative visualisation of how such a geodesic would look like in a projection diagram can be found in Fig. 3.3 (orange line). Then there are also geodesics forming the illumination pattern that reveals the black hole shadow to an observer outside the horizons, being the counterpart to the large angular momentum case from above. This corresponds to the blue line in Fig. 3.3. Furthermore, there also exist geodesics which are bound by either having large angular momentum and oscillating in the vicinity of the black hole forever, or by having critical angular momentum $\lambda = \lambda_c$ and thus having constant radius r like in the third case above, although now there are two distinct critical angular momenta, one larger and one smaller zero $\lambda_{c-} < 0 < \lambda_{c+}$. These angular momenta correspond to prograde and retrograde orbits (orbits in the sense of rotation of the black hole and opposite to it, respectively). A more thorough discussion of such geodesics can be found in [27]. In Fig. 3.3 one finds a qualitative drawing of a geodesic with constant radial coordinate r in purple.

However, the plot shows different aspects when considering vortical null geodesics with $\eta < 0$, depicted in Fig. 3.2c. In this case, there is a gap opening up at $r < 0$ which a horizontal path can pass and actually reach arbitrary negative radial values. The fact that geodesics can only move on horizontal lines in these graphs and only reach turning points in the radial motion once they hit a forbidden region ensures that geodesics which pass through this small new gap at $r < 0$ will go all the way to the asymptotically flat

spacetime at $|r| \to \infty$. In the projection diagram Fig. 2.5a this would correspond to a path starting in (I), crossing the outer horizon to get into (II), and finally end up at spatial infinity in (III). Such a geodesic is depicted in Fig. 3.3 in green. It is interesting to note that although the black hole acts repellent in the region with negative radial component, there are geodesics which come from positive radii, cross both horizons and dip through to negative radii, before getting reflected outwards again (an example would be a trajectory with $\lambda = 0$ in Fig. 3.2c). Concluding, one can define two different sets of boundaries by solving the equations $R(r) = 0$ and $\mathrm{d}R(r)/\mathrm{d}r = 0$, which for $\eta < 0$ has four different solutions. One corresponds to the black hole shadow outside the event horizon ($r > r_+$) while the other one corresponds to the small gap opening up at $r < 0$. Consequently, these boundaries separate regions in the λ-direction where the radial potential $R(r)$ has zero, two or four real roots. By not fixing η in the beginning, one can calculate these boundaries in the λ-η-parameter-space, an approach which we will take in the rest of this subsection, although in a slightly modified way.

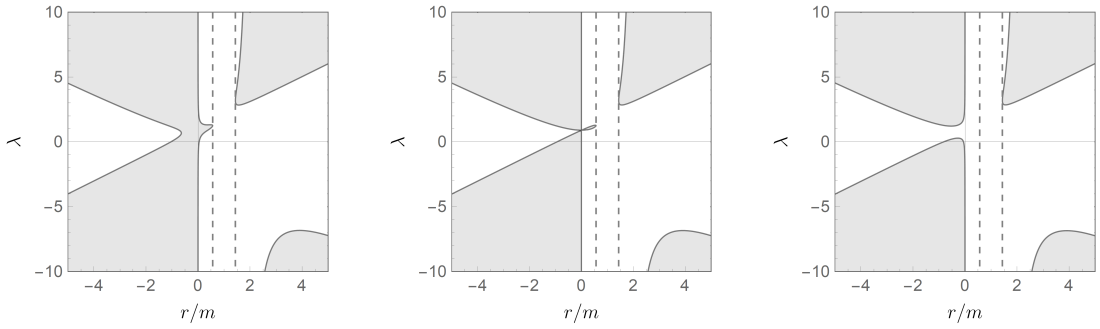

(a) $\eta > 0$ (b) $\eta = 0$ (c) $\eta < 0$

Figure 3.2.: r-λ-plot of null geodesics in the fast rotating case $a/m = 0.9$. The dotted lines correspond to the inner and outer horizon at r_- and r_+, respectively.

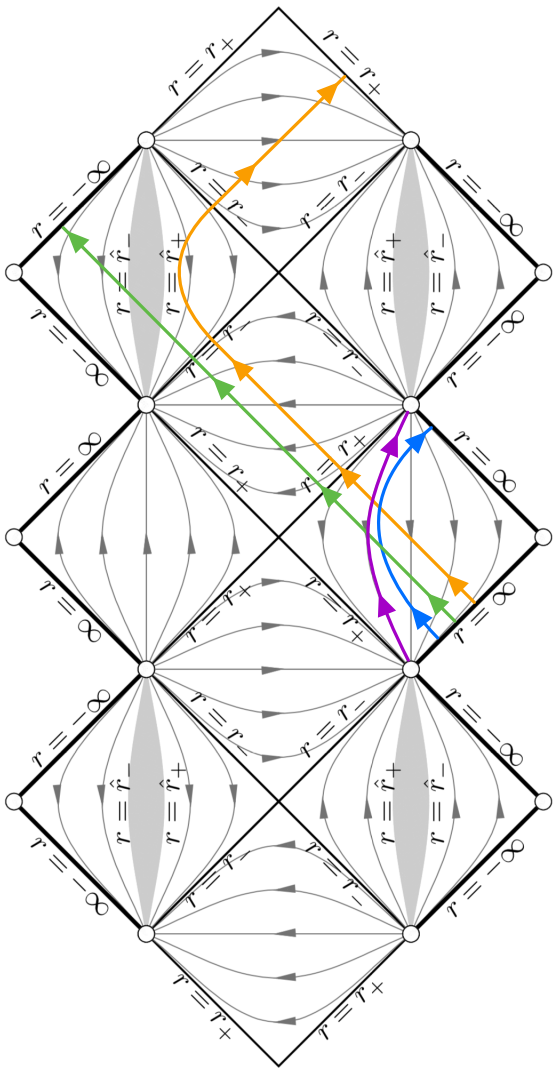

Figure 3.3.: Four qualitative examples of geodesics in the projection diagram of Kerr spacetime. All geodesics (except for the purple one) start at $r = +\infty$. The orange one crosses both horizons before getting reflected outwards again, this time in a different part of spacetime. The blue trajectory describes ingoing geodesics which are reflected outwards again at some point outside the event horizon, thus forming part of the black hole's shadow for an observer in the exterior region. The purple trajectory stays at constant radius for all times. The green geodesic starts at $r = +\infty$ and ends up at $r = -\infty$, thus crossing both potential gaps in Fig. 3.2c. The underlying plot is taken from [7].

Impact parameters

Before we analyse these boundaries in the parameter space any further, it is necessary to reconsider what insights we want to gain from it. The focus should lie on enabling the visualisation of the appearance of the black hole as seen by an observer far away from the black hole (i.e. $|r| \to \infty$) as this is the main goal of this thesis. Therefore, an

analysis of the boundaries of the turning points in the radial direction is not immediately helpful in the rather abstract λ-η-parameter-space. Nevertheless, some authors who were not mainly concerned with visualisation took this approach, e.g. [17]. [35] did also the most part of the analysis in the λ-η-parameter-space and only at the end connected these constants of motion to a local reference frame to obtain a visualisation of the black hole exterior. There is, however, a quite elegant way to convert the parameters λ and η to a more suitable form for our task. This involves the definition of impact parameters, as was done by e.g. Bardeen [2] where one can also find a detailed derivation. He first calculated how an observer would measure the momenta of a geodesic locally using Boyer-Lindquist coordinates. Based on this and the assumption that an observer far away from the black hole measures the direction of photons which reach them relative to the centre of symmetry of the spacetime (i.e. the line of sight of the observer is to the centre of the spacetime), Bardeen related the constants of motion λ and η to the impact parameters using

$$\alpha = \frac{\lambda}{\sin\theta_o} \,, \tag{3.41}$$

$$\beta = \nu_\theta \sqrt{\eta + a^2\cos^2\theta_o - \lambda^2 \,\frac{\cos^2\theta_o}{\sin^2\theta_o}} \,. \tag{3.42}$$

These impact parameters given here differ from those in [2] only by the overall sign in equation (3.41). This is due to the fact that they considered an observer at positive radii whereas we want the observer to be located far away from the black hole in the negative-r-region (for a more detailed description of the spacetime location of the observer we are considering, see the beginning of chapter 5). Because these impact parameters are normalized by the radial position of the observer (for details see [2]), this change from $r_o > 0$ to $r_o < 0$ gives an additional minus sign in both equations. Additionally, as we want to integrate "into the past" (and thus receive the photons at $r_o = -\infty$), we further need to flip the sign of ν_θ (corresponding to the sign of $p_\theta = g_{\theta\theta}\,\mathrm{d}\theta/\mathrm{d}\tau$, which changes sign for $\tau \to -\tau$).
For an observer substantially far away from the black hole, these impact parameters create a coordinate grid on a small part of the sky centred around the black hole. The impact parameters α and β therefore serve as a field of view for the observer when looking directly at the black hole, thus helping in visualising how such an observer would perceive the black hole. In this case α describes the displacement perpendicular to the axis of symmetry while β represents the displacement parallel to the axis of symmetry. A qualitative plot of how such a visualisation could look like for $r > 0$ is given in Fig. 3.4.
However, the price one has to pay by introducing these new parameters is that the location of the observer in the polar direction θ_o needs to be specified, hence the analysis of the radial potential is observer-dependent. The impact parameters (3.41) and (3.42) are problematic only at $\sin\theta_o = 0$, which corresponds to an observer located in the axis of symmetry. This problem is solved by the fact that any geodesic going through the axis of symmetry (at which $\sin\theta = 0$), and therefore especially those reaching an observer located in the axis of symmetry (for which $\sin\theta_o = 0$) must necessarily have vanishing angular momentum $\lambda = 0$ (see e.g. [27]). We will again encounter this peculiarity in subsection 3.2.2. The statement $\sin\theta_o = 0 \Leftrightarrow \lambda = 0$ also becomes apparent when considering the

inverses of (3.41) and (3.42):

$$\lambda = \alpha \sin\theta_o \,, \tag{3.43}$$

$$\eta = \beta^2 + (\alpha^2 - a^2)\cos^2\theta_o \,. \tag{3.44}$$

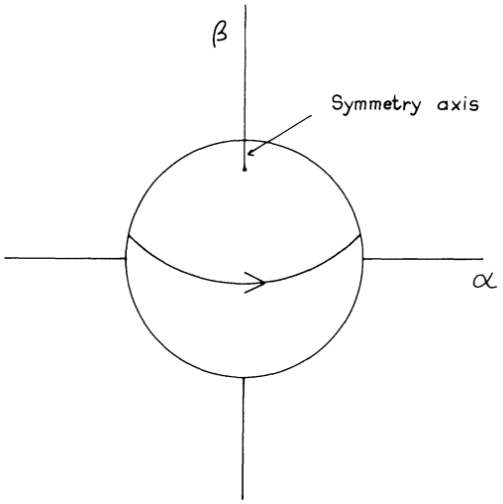

Figure 3.4.: Visualisation of the impact parameters on the celestial sphere of an observer far away from the black hole ($|r| \gg 0$). α serves as the displacement perpendicular to the symmetry axis, β as the displacement parallel to the symmetry axis. The black hole rotation is from left to right. The figure is taken from [2].

Throats

Having found a parameter space which serves our goal of visualising the appearance of the black hole, we are now ready to analyse the radial motion further. We can express (3.30) in terms of α and β by using (3.43) and (3.44) to get

$$R(r) = (r^2 + a^2 - a\,\alpha\sin\theta_o)^2 - (r^2 - 2mr + a^2)\left(\beta^2 + (\alpha^2 - a^2)\cos^2\theta_o + (\alpha\,\sin\theta_o - a)^2\right) \,.$$

Consequently, the conditions $R(r) = 0$ and $\mathrm{d}R(r)/\mathrm{d}r = 0$ define curves in the α-β-plane which separate parameter-regions in which $R(r)$ has zero, two, or four real roots. These curves are the boundaries of the openings of the radial potential inside and outside the horizon, as they are shown in Fig. 3.2c. A representative selection of three different cases for the parameter a can be seen in Fig. 3.5.
The non-rotating Schwarzschild case is depicted in Fig. 3.5a, where one can see that only one such opening gap is present, namely the one outside the horizon (cf. 3.1c). Since the Schwarzschild solution is spherically symmetric, this boundary is also symmetric. More specifically, the boundary is independent of the observational polar angle θ_o and as already mentioned, it corresponds to the shadow of the black hole as seen by an observer outside the black hole.
However, considering a rotating black hole ($a \neq 0$), parts of the symmetry are lost and another curve appears, corresponding to the inner gap forming at $r < 0$. This loss of symmetry corresponds to the spacetime not being symmetric in the polar direction. Two

such cases can be found in Fig. 3.5b and Fig. 3.5c. By departing from $a = 0$, the innermost curve appears at the origin ($\alpha = 0,\ \beta = 0$). Approaching the critical rotation $a/m = 1$, this inner curve grows and gets shifted to the right. Simultaneously, the outer boundary shifts to the left and gets flattened on the right side. Discussed by many authors in the past, this outer curve outlines the shadow of a rotating black hole as seen by an exterior observer (see e.g. [2] for the Kerr case or [22] for the Schwarzschild case). The two curves are known as inner/outer throat, respectively. Throughout this thesis, whenever we say "a geodesic inside the inner/outer throat" we more precisely mean "a geodesic with impact parameters inside the inner/outer throat".
As already mentioned, a very useful point of view of these throats is that they separate three regions. Outside the outer throat the polynomial $R(r)$ has four distinct real roots. In the region between the inner and the outer throat, two real and two complex roots are admitted by $R(r)$ (a pair of complex conjugates), and inside the inner throat the radial potential only has complex roots (two pairs of complex conjugates). From this, one can deduce that inside the inner throat, there are no turning points in the radial coordinate as they appear exactly at the real roots of $R(r)$ – once the geodesic's initial direction is fixed by ν_r in (3.40), it keeps its direction forever, i.e. an initially ingoing/outgoing geodesic will stay ingoing/outgoing. In turn, this deduction also tells us that no geodesic with impact parameters outside the inner throat can travel from $r = +\infty$ to $r = -\infty$ or vice versa since at some point it must hit a radial potential barrier and get reflected (cf. the large angular momentum case in 3.2c). For light coming from a source at $r > 0$ this reflection happens at either $r > r_+ > 0$ or at finite $r < 0$. Thus, only null geodesics having impact parameters within the inner throat can connect a light source at positive radius and an observer very far away from the black hole in the negative-r-region ($r_o \to -\infty$).

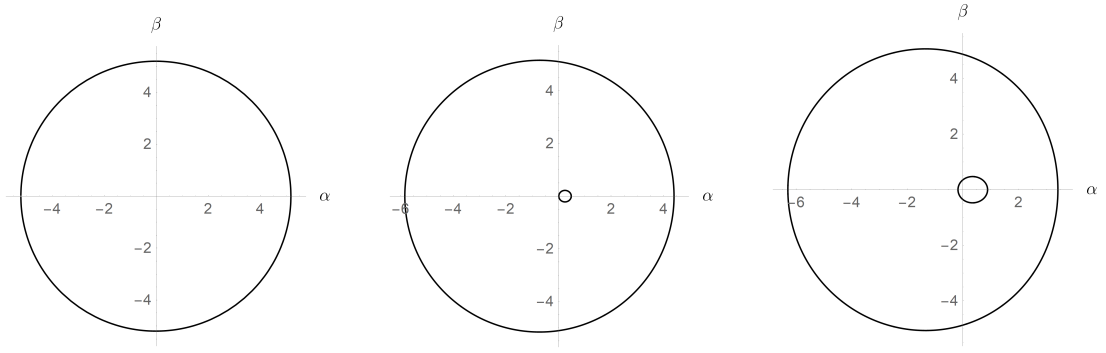

(a) $a = 0$ (b) $a = 0.5$ (c) $a = 0.9$

Figure 3.5.: Inner and outer throat for different rotational parameters in the α-β-parameter-plane. The observers polar angle is $\theta_o = \pi/4$.

Because the outer throat resembles the boundary of a black hole's shadow as seen by an observer outside the horizon, it is astrophysically important to study it in detail in order to predict the appearance of such a black hole for an observer $r > r_+$. For this reason, many papers in the past were concerned mainly with this outer throat and thus the simulation of a photograph of a black hole (cf. references given in section 1). Our goal will be to study geodesics starting at some source at positive radius and reaching the observer in the limit $r_o \to -\infty$, therefore we will analyse the inner throat more thoroughly. In contrast

to Fig. 3.5, we will do so by considering fixed rotation a/m while varying the observers polar angle θ_o. By visually studying the behaviour of the inner throat in Fig. 3.6, one can see that if $\theta_o = 0$, i.e. if the observer is located in the axis of symmetry, the inner throat will be a symmetric circle centred around the origin ($\alpha = 0,\ \beta = 0$). As the observer approaches the equatorial plane at $\theta = \pi/2$, the inner throat shrinks, becomes egg-shaped and shifts to the right until it vanishes at ($\alpha = a/m, \beta = 0$). Hence, there are no geodesics which start at $r > 0$ and reach an observer at $r < 0$ (with $|r| \gg 1$) located in the equatorial plane, a feature which will be explained in more detail in the next subsection 3.2.2.
The inner throat will serve us as the field of view for our observer since we want to consider a light source at positive radii and the observer in the limit $r_o \to -\infty$.

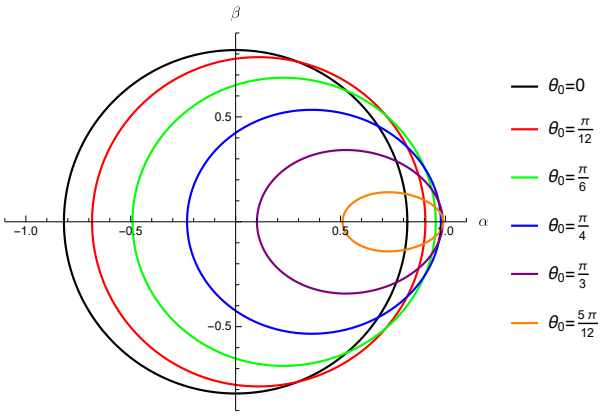

Figure 3.6.: The inner throat for different poloidal locations of the observer θ_o, fixed rotational parameter $a/m = 0.99$, and mass $m = 1$. $\theta_o = 0$ corresponds to the observer located in the axis of symmetry while $\theta_o = \pi/2$ means they are located in the equatorial plane.

A qualitative fact which will become apparent in later sections is that geodesics which are inside the inner throat but very close to its boundary stay a rather long time in the vicinity of the black hole compared with geodesics in the middle of the inner throat. This is due to the fact that these geodesics nearly hit a forbidden region (cf. Fig. 3.2c) when passing the radial potential gap at $r < 0$. As at the boundary of the forbidden region the right hand side of (3.40) vanishes and it is smooth in the allowed region, it follows that $\mathrm{d}r/\mathrm{d}\tau$ becomes small for geodesics near the throat boundary. Since this corresponds to the radial velocity of the null geodesic, the radial motion almost comes to a standstill barely below $r = 0$ at the point where it is just let through the throat (as opposed to getting reflected).

3.2.2. Polar motion

The polar motion of a geodesic in Kerr spacetime is governed by (3.33), which, upon inserting (3.31), becomes

$$\frac{\mathrm{d}\theta}{\mathrm{d}\tau} = \nu_\theta \sqrt{\eta + a^2 \cos^2\theta - \lambda^2 \frac{\cos^2\theta}{\sin^2\theta}}\ . \tag{3.45}$$

One of the most striking behavioural aspects of vortical null geodesics is concerned with this polar motion, namely the boundedness of motion to one hemisphere, i.e. the geodesic

is trapped either in the northern hemisphere $0 \leq \theta < \pi/2$ or in the southern hemisphere $\pi/2 < \theta \leq \pi$, where θ is its polar angle (in both Boyer-Lindquist as well as in Eddington-Finkelstein-like coordinates). A quick explanation to this is given by noting that in the equatorial plane (at $\theta = \pi/2$) the angular potential (3.31) becomes $\Theta(\theta) = \eta$ and consequently (3.45) is simplified to $\mathrm{d}\theta/\mathrm{d}\tau = \nu_\theta\sqrt{\eta}$. The defining characteristic of vortical geodesics is $Q < 0$ or equivalently $\eta < 0$, and thus the polar trajectory of a vortical null geodesic would become complex as it crosses the equatorial plane. From the formula for the angular potential in the equatorial plane it is also clear that the only geodesics which are completely contained in the equatorial plane must have $Q = 0$, since then $\mathrm{d}\theta/\mathrm{d}\tau \equiv 0$ for all times τ. It is this restriction of motion to one hemisphere that the subclass of vortical geodesics gets its name from (the trajectories of such geodesics look a bit like a vortex when going radially inwards).

Turning points in the polar motion

Since the motion is confined to one hemisphere but the radicand in (3.45) is in general non-zero, the geodesic must show oscillatory behaviour with turning points at the roots of $\Theta(\theta)$ (similar argument as in the radial case). To calculate the roots of this angular potential (given by (3.31)) it is useful to substitute $u = \cos^2\theta$ (as was done by e.g. [17] and [35]). With this substitution, one can calculate the roots of the new polynomial

$$\Theta(u) = \eta + a^2\, u - \lambda\, \frac{u}{1-u}\,, \tag{3.46}$$

and after resubstitution for u one finds the four roots of $\Theta(\theta)$ to be

$$\theta_i = \arccos(\pm\sqrt{u_\pm}) \tag{3.47}$$

with $i = 1, 2, 3, 4$, and where we defined

$$u_\pm = \frac{a^2 - \eta - \lambda^2}{2a^2} \pm \sqrt{\left(\frac{a^2 - \eta - \lambda^2}{2a^2}\right)^2 + \frac{\eta}{a^2}}\,. \tag{3.48}$$

A deeper analysis of this in λ-η-space can be found in [17]. The authors of this paper found, among other things, that vortical geodesics oscillate between

$$\theta_\pm = \arccos(h\sqrt{u_\mp})\,, \tag{3.49}$$

where $h = \mathrm{sign}(\cos\theta)$ determines the hemisphere the geodesic is bound to. We want to use this result to further analyse vortical geodesics inside the inner throat in the impact parameter space spanned by α and β. We use (3.43) and (3.44) to get an equation for $u_\pm(\alpha, \beta)$, resulting in

$$\begin{aligned} u_\pm = \frac{1}{4}\Bigg(3 - \frac{2(\alpha^2+\beta^2)}{a^2} + \cos(2\theta_o) \\ \pm 4\sqrt{\frac{\beta^2 + \cos^2\theta_o(\alpha^2 - a^2)}{a^2} + \frac{(a^2(\cos(2\theta_o)+3) - 2(\alpha^2+\beta^2))^2}{16a^4}}\Bigg)\,. \end{aligned} \tag{3.50}$$

This, together with (3.49), defines the polar turning points $\theta_\pm(\alpha, \beta)$ in dependence of the impact parameters.

Geodesics with constant polar angle/Principal null congruences

By solving the equation $u_+ = u_-$ we get points in the impact-parameter-plane where geodesics have constant polar angle $\theta = \theta_+ = \theta_-$. This gives us four solutions for α in dependence of β

$$\alpha = \pm\sqrt{(i\beta \pm a\sin\theta_o)^2}\ , \tag{3.51}$$

where i is again the imaginary unit defined by $i = \sqrt{-1}$. Similarly, we can calculate four solutions for β in dependence of α

$$\beta = \pm\sqrt{-(\alpha \pm a\sin\theta_o)^2}\ . \tag{3.52}$$

From (3.52) it is easy to see that β is only real when both sides vanish, thus the only two points in the α-β-space with constant polar angle θ along the whole trajectory are at

$$(\alpha = \pm a\sin\theta_o,\ \beta = 0)\ . \tag{3.53}$$

In λ-η-space these two points correspond to $\lambda = \pm a\sin^2\theta_o$ and $\eta = -a^2\cos^4\theta_o$.
Notice that for an observer in the axis of symmetry ($\theta_o = 0$) these two points coincide (because $\sin(0) = 0$). To determine if an observer with position at $r_o = -\infty$ can see photons with constant polar angle coming from positive radii, it remains to determine if these points lie inside the inner throat. For this, we can simply take the parametric solution for the inner throat boundary $(\alpha_{bnd.}(a,\theta_o,r,m), \beta_{bnd.}(a,\theta_o,r,m))$ from the previous section (due to this solution being very lengthy we do not give an explicit formula for this parametric solution but it is easily calculated by requiring $R(r) = \mathrm{d}R(r)/\mathrm{d}r = 0$) and compute if/where this parametric curve coincides with the points of constant θ at $(\alpha = \pm a\sin\theta_o,\ \beta = 0)$. Therefore, the final result will be a pair $(a(\theta_o,r,m),\ \theta_o(a,r,m))$ defining the points for in the impact-parameter-space for which this happens. Performing this calculation results in eight solutions for the rightmost point of constant θ at $(\alpha = a\sin\theta_o,\ \beta = 0)$

$$(a,\theta_o) = \left(\pm\sqrt{r(2m-r)}, \pm\arccos\left(\pm\sqrt{\frac{r}{r-2m}}\right)\right)\ , \tag{3.54}$$

whereas for the leftmost point of constant θ at $(\alpha = -a\sin\theta_o,\ \beta = 0)$ we get

$$(a,\theta_o) = \left(\pm\sqrt{\frac{r^2(3m-2r)}{m}}, \pm\arccos\left(\pm\sqrt{\frac{3m}{3m-2r}}\right)\right)\ . \tag{3.55}$$

Let us first analyse the first of these equations. There are two ways of seeing that (3.54) never gives real valued solutions for a and θ_o, regardless of the values of m and r, i.e. that there are no values for m and r such that this rightmost point in impact-parameter-space coincides with the inner throat boundary. Such geodesics would be bound geodesics with constant radial and polar component.
The first approach is a case distinction for different r in (3.54). Negative radii $r < 0$ will always result in complex rotation a since in this case $r(2m-r) < 0$ (we assume $m > 0$). The case of vanishing radius $r = 0$ recovers an equatorial geodesic in Schwarzschild spacetime where $a = 0$ and $\theta_o = \pi/2$. Since there is no inner throat in the Schwarzschild limit, this solution is not what we desire. Positive radii $r > 0$ lead to complex angle θ_o.

To see this, note that for $0 < r < 2m$ the argument of arccosine will be complex because of $r - 2m < 0$. For $r > 2m$ the argument will be real but greater 1. Since the inverse of cosine is only defined between -1 and 1 for real arguments, this produces a complex angle too. And lastly, the special case $r = 2m$ results in either a complex polar angle because (a) the argument of arccosine is imaginary (for $r \nearrow 2m$) or (b) the argument of arccosine is real but diverges, especially meaning that it is larger 1 (for $r \searrow 2m$).
The second (and arguably easier) possibility to prove that (3.54) does not produce real valued solution is to calculate $a(\theta_o)$ by first expressing r in terms of θ_o using the second equation of (3.54) and then substituting this in the first equation, resulting in

$$a_{crit,\,left}(\theta_o) = \pm 2im \frac{|\cot\theta_o|}{\sin\theta_o} \,. \tag{3.56}$$

Regardless of where the observer is located in the polar direction, there is no real rotational parameter $a(\theta_o)$ (other than the Schwarzschild case $a = 0$ in the equatorial plane $\theta_o = \pi/2$ which needs to be excluded) such that the impact parameters $(\alpha = +a\sin\theta_o,\ \beta = 0)$ coincide with the inner throat boundary. We will not calculate $\theta_o(a)$ in this case since this would not give additional insights.
The question now is, if the point $(\alpha = +a\sin\theta_o,\ \beta = 0)$ lies inside or outside the inner throat. For the values $a/m = 0.99$ and $\theta_o = 0$ as in Fig. 3.6 the point of constant θ is at $(\alpha = 0,\ \beta = 0)$ and thus lies definitely inside the inner throat. As this rightmost point of constant polar angle can never cross over to the outside of the inner throat, we conclude that it always lies inside. Therefore, every observer at $r_o = -\infty$ with polar angle θ_o can see a geodesic with constant polar angle connecting the observer and some point in the region $r > 0$ at the impact parameters $(\alpha = +a\sin\theta_o,\ \beta = 0)$.
As a geodesic with $(\alpha = +a\sin\theta_o,\ \beta = 0)$ corresponds to the principal null congruence on which the transformation to Eddington-Finkelstein-like coordinates is based on (cf. [29]), we claim that along this geodesic also ψ and u should remain constant. We prove this by showing that the equations of motion (3.34) for ψ and (3.35) for u are identically zero in this case. Let us begin by evaluating the constants of motion (3.43) and (3.44) at these impact parameters, leading to

$$\lambda = a\sin^2\theta_o \,, \tag{3.57}$$
$$\eta = -a^2\cos^4\theta_o \,, \tag{3.58}$$

with which the radial potential (3.30) becomes

$$\begin{aligned} R(r) &= (r^2 + a^2 - a^2\sin^2\theta_o)^2 - \Delta\left(-a^2\cos^4\theta_o + (a\sin^2\theta_o - a)^2\right) \\ &= (r^2 + a^2\cos^2\theta_o)^2 \,. \end{aligned} \tag{3.59}$$

For vortical geodesics we have $r^2 + a^2\cos^2\theta_o > 0$ which simplifies the radial equation (3.32) to

$$\frac{\mathrm{d}r}{\mathrm{d}\tau} = \nu_r(r^2 + a^2\cos^2\theta_o) \,. \tag{3.60}$$

Furthermore, we get for the azimuthal equation (3.34)

$$\begin{aligned}\frac{\mathrm{d}\psi}{\mathrm{d}\tau} &= \frac{a}{\Delta}\left(2mr - a\lambda - \sqrt{R(r)}\right) + \frac{\lambda}{\sin^2\theta_o} \\ &= \frac{a}{\Delta}\left(2mr - a^2\sin^2\theta_o - r^2 - a^2\cos^2\theta_o\right) + \frac{a\sin^2\theta_o}{\sin^2\theta_o} \\ &= \frac{a}{\Delta}\left(2mr - a^2(\sin^2\theta_o + \cos^2\theta_o) - r^2 + (r^2 - 2mr + a^2)\right) \\ &= 0\,, \end{aligned} \tag{3.61}$$

where in the second line we used (3.57), (3.58), and (3.59), as well as the fact that $\theta = \theta_o$ stays constant throughout the trajectory. Similarly, the calculation for u-equation (3.35) is given by

$$\begin{aligned}\frac{\mathrm{d}u}{\mathrm{d}\tau} &= \frac{r^2 + a^2}{\Delta}\left(r^2 + a^2 - a\lambda - \sqrt{R(r)}\right) + a(\lambda - a\sin^2\theta) \\ &= \frac{r^2 + a^2}{\Delta}\left(r^2 + a^2 - a^2\sin^2\theta_o - r^2 - a^2\cos^2\theta_o\right) + a(a\sin^2\theta_o - a\sin^2\theta_o) \\ &= 0\,. \end{aligned} \tag{3.62}$$

The results (3.61) and (3.62) show that besides the polar angle θ, also the azimuthal angle ψ, as well as the coordinate time u stay constant along a geodesic with impact parameters $(\alpha = +a\sin\theta_o,\ \beta = 0)$.
Now let us discuss the solution for the left edge of the inner throat (3.55). We can solve this system of equations for either $a(\theta_o)$ or $\theta_o(a)$. The easier case is the former, resulting in

$$a_{crit,\,right}(\theta_o) = \frac{3\sqrt{3}m}{2}\frac{\tan^2\theta_o}{|\cos\theta_o|}\,, \tag{3.63}$$

where we already chose the plus sign in front of the square root since we restricted ourselves to the case $a > 0$ (cf. section 2.2). This defines a critical rotation parameter a depending on the observer's polar position θ_o. For rotations faster than this critical rotation, the observer at θ_o will perceive two distinct points with constant polar coordinate inside the inner throat. Fig. 3.7 visualises the result of equation (3.63) for $0 \leq \theta_o \leq \pi/2$. Since the physically acceptable cases are restricted to $a < m$, there is only a very limited range of possible observer locations for two points of constant θ to appear. Solving (3.63) for $a/m = 1$ gives us an upper bound to this range which is $\theta_{o,max} = \pi/6$. Consequently, only observers with $0 < \theta_o < \pi/6$ can in principle observe these two distinct points, depending on the rotation speed a of the black hole.

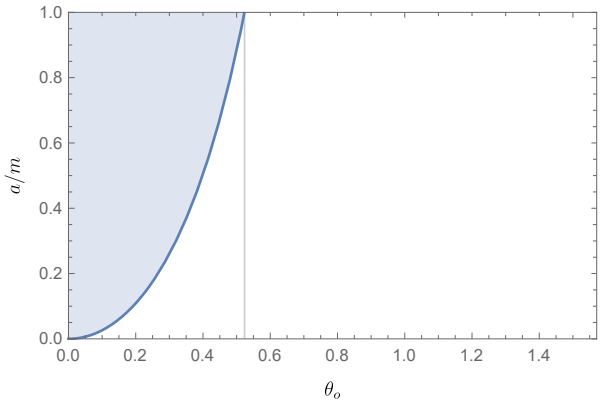

Figure 3.7.: Plot of (3.63) for $0 < \theta_o < \pi/2$. The shaded area indicates combinations of a/m and θ_o where two distinct points of constant θ lie inside the inner throat. On the boundary curve, the leftmost point of constant polar angle lies exactly at the inner throat boundary, corresponding to a geodesic with constant polar angle being captured in an orbit around the black hole. The vertical line corresponds to $\theta_o = \pi/6$.

The case of solving for $\theta_o(a)$ will give us no further insights, thus we are only stating the result here without further discussion. As the equation for a in (3.55) is cubic in r upon squaring both sides, it leads to three different solutions for r, which we then insert in the equation for θ_o. Consequently, $\theta_o(a)$ has $3 \times 4 = 12$ solutions, which are

$$\theta_{o,crit,1}(a) = \pm \arccos\left(\pm\sqrt{\frac{-3\rho m}{(m-\rho)^2}}\right), \tag{3.64}$$

$$\theta_{o,crit,2}(a) = \pm \arccos\left(\pm\sqrt{\frac{6\rho m}{4\rho m + m^2 + \rho^2 + i\sqrt{3}(\rho^2 - m^2)}}\right), \tag{3.65}$$

$$\theta_{o,crit,3}(a) = \pm \arccos\left(\pm\sqrt{\frac{6\rho m}{4\rho m + m^2 + \rho^2 - i\sqrt{3}(\rho^2 - m^2)}}\right), \tag{3.66}$$

where we defined $\rho = \sqrt[3]{m^3 - 2ma^2 + 2ma\sqrt{a^2 - m^2}}$. It is not immediately obvious whether these give the correct result or that they are even real-valued. By numerical calculation one can see that the third of these solutions is the only one giving real results and thus being the inverse function of (3.63). The $\pm$ in the argument of arccosine determines the hemisphere the geodesic is bound to, and can thus, as before, be replaced by $h = \text{sign}(\cos\theta)$. The sign in front of arccosine corresponds to a mirroring about the axis of symmetry which is equivalent to a rotation about π in the azimuthal direction. Since Kerr spacetime is rotationally symmetric in the azimuthal angle, this describes the same physical situation.
As a side note we want to mention that the calculations concerning the conservation of ψ and u in the case of ($\alpha = +a\sin\theta_o$, $\beta = 0$) above are not valid in the case ($\alpha = -a\sin\theta_o$, $\beta = 0$), meaning that even if the observer can see a geodesic with these impact parameters (which is not always the case) it does not have constant ψ and u.

Geodesic motion close to equatorial plane

Another question we can ask is how close a geodesic comes to the equatorial plane at $\theta = \pi/2$ on the course of its journey before escaping to $r \to -\infty$ and hitting a specific point on the observer's photographic plate (defined by the impact parameters α and β). These geodesics are worth discussing as we can thus decide wheter a luminous thin accretion disk around the black hole (typically assumed to be in the vicinity of the equatorial plane at $r > 0$) will be visible for an observer at $r_o = -\infty$. Note that the simplification of an infinitely thin accretion disk lying exactly in the equatorial plane (which is often made for studying the visual appearance of the black hole for an observer outside the event horizon) is of no use in the case of an observer at $r < 0$. The reason being that as was discussed in the beginning of this subsection, geodesics connecting some source-point at $r > 0$ to an observer at $r < 0$ can never cross the equatorial plane.
From the general behaviour of arccosine and (3.49) we can see that the polar turning point closest to the equatorial plane is always θ_+, regardless of the hemisphere specified by h. In the northern hemisphere ($0 < \theta < \pi/2$) we therefore have $\theta_- < \theta_+$, whereas in the southern hemisphere ($\pi/2 < \theta < \pi$) we get $\theta_- > \theta_+$. Because the spacetime is symmetric under mirroring around the equatorial plane (most easily seen by taking $z \to -z$ in (2.9)), the southern hemisphere case will not give different physical phenomena compared with the northern hemisphere. Thus, we will restrict our analysis to the northern hemisphere. Using (3.49) with (3.50) we can now numerically calculate $\theta_\pm$ for each point inside the inner throat and fixed θ_o and a/m. Examples for four different θ_o's and $a/m = 0.99$ are shown in Fig. 3.8. Any geodesic with certain impact parameters (α, β) inside the inner throat will oscillate between its corresponding values for θ_- (red) and θ_+ (green). It is clearly visible that these plots are, as anticipated, symmetric under $\beta \to -\beta$. Furthermore, one can see that an observer close enough to the axis of symmetry, namely with $0 < \theta_o < \theta_{crit} \approx 0.5217 < \pi/6$, receives a pair of two distinct photons which have constant angular coordinate θ (corresponding to the red and the green surface touching). The upper bound $\theta_{crit} \approx 0.5217$ for θ_o describes the point where the impact parameters of the geodesic with constant θ coincide with the inner throat boundary in the case of $a/m = 0.99$. The value $\pi/6$ is the maximal upper bound associated to the extreme Kerr case $a/m = 1$ (cf. Fig. 3.7). At $\theta_o = 0$ there will be only one single point of constant θ, located at ($\alpha = 0$, $\beta = 0$).

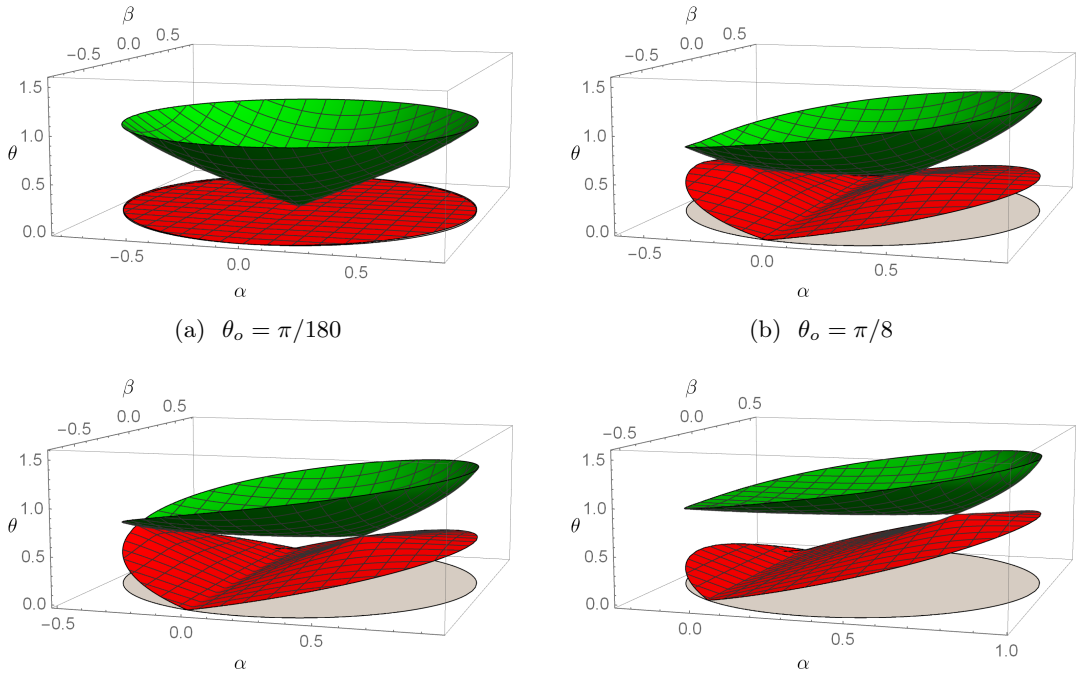

(a) $\theta_o = \pi/180$ (b) $\theta_o = \pi/8$

(c) $\theta_o \approx 0.5217 < \pi/6$ (d) $\theta_o = \pi/4$

Figure 3.8.: 3D-plots of θ_+ (green) and θ_- (red) inside the inner throat (grey disk) for fixed subcritical rotation $a/m = 0.99$ and varying polar angle θ_o of the observer. For angles $\theta_o < \theta_{crit} \approx 0.5217 < \pi/6$ there are two points where the green and the red surface make contact, i.e. points where $\theta_+ = \theta_-$ and thus $\theta = const.$ along the geodesic.

If we only restrict $\alpha = 0$ without exactly specifying β and $0 < \theta_o < \pi/2$, we find that such a geodesic will always hit the axis of symmetry, indicated by the kink in the red θ_--surface touching $\theta = 0$ (clearly visible in Fig. 3.8b - 3.8d). To approach this quantitatively, we are led to inspect (3.49) for $\alpha = 0$:

$$\begin{aligned}
\theta_-\big|_{\alpha=0} &= \arccos(h\sqrt{u_+})\big|_{\alpha=0} \\
&= \arccos\left(\frac{h}{2}\sqrt{3 - \frac{2\beta^2}{a^2} + \cos(2\theta_o) + \sqrt{\frac{(a^2 + 2\beta^2 - a^2\cos(2\theta_o))^2}{a^4}}}\right) \\
&= \arccos\left(\frac{h}{2}\sqrt{\frac{3a^2 - 2\beta^2 + a^2\cos(2\theta_o) + a^2 + 2\beta^2 - a^2\cos(2\theta_o)}{a^2}}\right) \\
&= \arccos(h)\ . \qquad (3.67)
\end{aligned}$$

The third equality is valid as $a > 0$, $\beta^2 \geq 0$ and $\cos(2\theta_o) \leq 1$. In the northern hemisphere ($h = 1$) this is zero while in the southern hemisphere ($h = -1$) this equals π – both values correspond to reaching the axis of symmetry. This feature will also have further reaching consequences for the general behaviour of the polar motion of geodesics with $\alpha = 0$, as will be discussed in subsection 4.1.4.
Additionally, the closest point to the equatorial plane can be inspected to have $\beta = 0$ and

$\alpha = \alpha_{min}$, where α_{min} is the smallest possible value for α which still lies inside the inner throat. In the special case of the observer being located exactly in the axis of symmetry at $\theta_o = 0$, all points at the inner throat boundary have the same $\theta_\pm$. Hence, generally at the rightmost point inside the inner throat the photon which can come closest to the equatorial plane throughout its journey will reach the observer. Since this is in the very proximity of the inner throat boundary (corresponding to the radial potential barrier boundary) the geodesic will stay a rather long time in the vicinity of the black hole (this will be discussed in chapter 5). Having identified this special point inside the inner throat, we can calculate $\theta_\pm$ there and see how the oscillation in θ changes for different θ_o, and therefore how close such a geodesic can approach the equatorial plane. Because the point we will calculate lies exactly on the inner throat boundary (and not inside), this will only give us an upper bound on $\theta_\pm$ for geodesics inside the inner throat.
A visualisation of this is done in Fig. 3.9. It turns out that on the right edge of the inner throat $\theta_- = \theta_o$, i.e. the geodesic is always observed at its closest point to the axis of symmetry. On the other hand, θ_+ follows a strictly increasing function in θ_o, approaching $\pi/2$ as $\theta_o \to \pi/2$ (recall that the case $\theta_o = \pi/2$ must be excluded since in this case no geodesics starting from $r > 0$ can reach the observer at $r_o = -\infty$).
To determine the proximity to the equatorial plane for a vortical null geodesic somewhere along its path, we need only θ_+. The polar distance to the equatorial plane is determined by $\frac{\pi}{2} - \theta_+$. In the case of $a/m = 0.99$ it is clear from Fig. 3.9 that if an accretion disk extends (in polar direction) closer to the axis of symmetry than around $\theta \approx 0.975$ (corresponding to the value of θ_+ for $\theta_o = 0$), it could theoretically be visible for every observer at $r_o = -\infty$. Going to thinner accretion disk models, the observer at $r_o = -\infty$ needs to be closer to the equatorial plane as well in order for $\frac{\pi}{2} - \theta_+$ on the left edge of the inner throat to be greater than the maximal extent of the accretion disk. This, in turn, results in a smaller inner throat and hence a smaller field of view. It should also be noted that the geodesic can achieve its closest point to the equatorial plane θ_+ anywhere along its trajectory. In individual cases, further analysis is needed to determine whether or not the observer at $r_o = -\infty$ indeed is able to observe an accretion disk at $r > 0$ close to the equatorial plane.

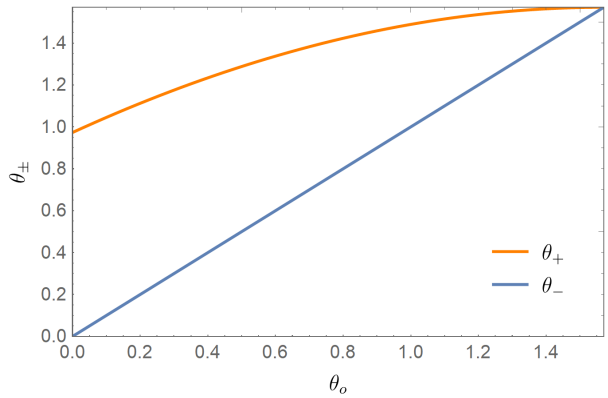

Figure 3.9.: $\theta_\pm$ for the rightmost point of the inner throat for varying polar angle of the observer θ_o. In this plot we used $a/m = 0.99$.

3.2.3. Gravitational redshift

For creating images of what an actual physical observer might see, one further task is to consider the redshift along the geodesic. In this section we want to discuss the gravitational redshift, and comment on the Doppler shift due to relative motion of source and observer which we want to consider.
In this thesis we want the observer to be stationary, which is (in Boyer-Lindquist coordinates) described by the worldline

$$\gamma_o^\mu(t) = (t,\ r_o,\ \theta_o,\ \varphi_o)$$

where r_o, θ_o and φ_o are constant. The four velocity of this observer is given by

$$U_o^\mu = (u_o^t, 0, 0, 0)\ .$$

Note that this does not necessarily correspond to an observer with zero angular momentum at any radial position r_o, which, due to the dragging of frames by the rotation of the black hole, does not have constant azimuthal coordinate but rather rotates with angular velocity [2]

$$\frac{\mathrm{d}\varphi}{\mathrm{d}t} = \frac{2amr_o}{(r_o^2+a^2)^2 - (r_o^2 - 2mr_o + a^2)a^2\sin^2\theta}\ ,$$

and only in the limit $|r_o| \to \infty$ we find that constant azimuthal coordinate corresponds to zero angular momentum of the observer. We normalise the four velocity by imposing

$$-1 = g(U_o, U_o) = g_{tt}(u_o^t)^2 \ \Rightarrow\ u_o^t = \frac{1}{\sqrt{-g_{tt}}}$$

and consequently get

$$U_o^\mu = \left(\frac{1}{\sqrt{-g_{tt}(r_o)}},\ 0,\ 0,\ 0\right)\ . \tag{3.68}$$

To emphasise and keep track of the fact that g_{tt} needs to be evaluated at the spacetime location of the observer, we explicitly wrote out the dependence on r_o. We immediately see that since $g_{tt}(r_o) = -(1 - \frac{2mr_o}{\Sigma(r_o)})$ an observer at $|r_o| \gg 1$ has four velocity $U_o^\mu = (1,0,0,0)$ (note that $\Sigma(r_o) = r_o^2 + a^2\cos^2(\theta) \propto r_o^2$ for large values of r_o). This result is also obvious with regard to the fact that in the limit $|r| \to \infty$ we find that the Kerr metric describes flat spacetime.
The light source we want to consider in this thesis is also stationary and located at fixed $r_s = +\infty$ with some fixed angular coordinates θ_s and ψ_s. The four velocity U_s of such a source is in this case the same as for an observer at $r_o = -\infty$.
We will calculate the gravitational redshift in the same manner as one does the calculation in the Schwarzschild case (see e.g. [10]).
The frequency of the emitted light as measured by an observer with four velocity U_a ($a \in \{o, s\}$, where o denotes the considered observer and s denotes (a hypothetical observer at) the light source) is given by

$$\omega_a = -g(U_a, K)\ , \tag{3.69}$$

where $K = \kappa\dot{\gamma}$ (where $\kappa > 0$) is the frequency four vector of a photon corresponding to a constant multiple of the tangent $\dot{\gamma} = (\dot{t}, \dot{r}, \dot{\theta}, \dot{\varphi})$ of a null geodesic $\gamma = (t, r, \theta, \varphi)$ in Kerr

spacetime (the dot denotes differentiation with respect to some affine parameter along the geodesic). Evaluating (3.69) further we find

$$\begin{aligned}\omega_a &= -g_{\mu\nu}\, U_a^\mu\, K^\nu \\ &= -g_{tt}\, U_a^t\, K^t - g_{t\varphi}\, U_a^t\, K^\varphi \\ &= -U_a^t(r_a)\, \left(g_{tt}(r_a)\, \kappa\, \dot{t} + g_{t\varphi}(r_a)\, \kappa\, \dot{\varphi}\right)\ , \end{aligned} \tag{3.70}$$

where again we can choose $a = o$ for the observer, or $a = s$ for (a hypothetical observer at) the source. Since the quantities g_{tt} and $g_{t\varphi}$ need to be evaluated at the spacetime position of the observer, we emphasise this again by explicitly writing the dependence on the radial position r_a in the last line.
To relate this frequency measured by the observer to the frequency measured at the source, i.e. relate ω_o to ω_s, we make use of the fact that energy is conserved along any geodesic, which corresponds to ∂_t being a Killing vector. Therefore the quantity

$$g(\partial_t, K) = g_{tt}\, \kappa\, \dot{t} + g_{t\varphi}\, \kappa\, \dot{\varphi} = const. \tag{3.71}$$

is conserved along the null geodesic connecting the source and the observer. Using this, we find the relation of the frequency as measured by an observer ω_o with the frequency as measured at the source ω_s to be

$$\begin{aligned}\omega_o &= -U_a^t(r_o)(g_{tt}(r_o)\kappa\dot{t} + g_{t\varphi}(r_o)\kappa\dot{\varphi}) \\ &= -U_a^t(r_o)(g_{tt}(r_s)\kappa\dot{t} + g_{t\varphi}(r_s)\kappa\dot{\varphi}) \\ &= \frac{U_a^t(r_o)}{U_a^t(r_s)}\, \omega_s \\ &= \frac{\sqrt{-g_{tt}(r_s)}}{\sqrt{-g_{tt}(r_o)}}\, \omega_s\ , \end{aligned} \tag{3.72}$$

where in the last line we used (3.68). As already mentioned earlier we have that $g_{tt}(r_{o/s}) \to -1$ as $|r_{o/s}| \to \infty$, and thus in the case of the observer being at $r_o = -\infty$ and the source being at $r_s = +\infty$ there will be no gravitational redshift and we find $\omega_o = \omega_s$.
Lastly, we want to mention that in the case of a stationary observer at $r_o = -\infty$ and a stationary source at $r_s = +\infty$ there will be no relative motion between source and observer and thus we also do not need to consider any Doppler shift.

4. Solving the geodesic equations

Before we start solving any equations, we specify again the goal we want to achieve in a summarising way. Our main aim is to visualise what a stationary observer located at some angles θ_o and ψ_o far away from the central black hole in the negative-r-region ($r_o = -\infty$) would see if they were to look directly at the centre of symmetry. The light source in this scenario is assumed to be at positive radii $r_s > 0$ (we ultimately want to take $r_s \to +\infty$ in this work but nothing prevents one to use finite $r_s > 0$). To obtain this visualisation, we need to find null geodesics (i.e. the paths of photons) which connect the source and the observer. These geodesics start at the source at $r_s > 0$ and end up at the observer at $r < 0$, thus they need to be vortical null geodesics ($Q < 0$ or $\eta < 0$) as shown in the previous section. Consequently, we need to solve the equations of motion for vortical null geodesics. They will be characterised by either the constants of motion (λ, η) or equivalently by the impact parameters (α, β). The transformation can easily be done using (3.43) and (3.44). Because the equations of motion and their solution do not give additional insight after the transformation, we will not give an explicit form here. Nevertheless, the impact parameters are an important tool for the visualisation and thus we will use them when implementing the solutions in Mathematica and consequently for any numerical calculations.
Apart from introducing (α, β), we did some more preliminary work towards achieving our goal by finding the differential equations of motion for null geodesics in Eddington-Finkelstein-like coordinates in subsection 3.1.1. For convenience we restate them here:

$$\frac{\mathrm{d}r}{\mathrm{d}\tau} = \nu_r \sqrt{R(r)} \,, \tag{4.1}$$

$$\frac{\mathrm{d}\theta}{\mathrm{d}\tau} = \nu_\theta \sqrt{\Theta(\theta)} \,, \tag{4.2}$$

$$\frac{\mathrm{d}\psi}{\mathrm{d}\tau} = \frac{a}{\Delta}\left(2mr - a\lambda - \sqrt{R(r)}\right) + \frac{\lambda}{\sin^2\theta} \,, \tag{4.3}$$

$$\frac{\mathrm{d}u}{\mathrm{d}\tau} = \frac{r^2+a^2}{\Delta}\left(r^2 + a^2 - a\lambda - \sqrt{R(r)}\right) + a(\lambda - a\sin^2\theta) \,, \tag{4.4}$$

where we used the radial and angular potentials $R(r)$ and $\Theta(\theta)$, as well as the horizon-defining function Δ. Definitions can be found in (3.14), (3.12) and (2.3), respectively.
For the task of solving these equations analytically, a well-suited approach is to cast them in integral form (similar to (3.7)-(3.10)). This approach was also taken by [17] whose calculations we will follow for the main part. However, in some points we will use different methods which we will indicate appropriately. The main difference to begin with is that we work in Eddington-Finkelstein-like coordinates which are regular globally, whereas the authors of [17] did their calculations in Boyer-Lindquist coordinates. Consequently, their solution is not valid for geodesics crossing the horizons, for they will become singular in φ and t there. As they were only interested in the Kerr exterior, these singularities did not state a problem for their analysis.

In integral form (4.1)-(4.4) become

$$\int_{\theta_s}^{\theta_o} \frac{\mathrm{d}\theta}{\sqrt{\Theta(\theta)}} = \int_{r_s}^{r_o} \frac{\mathrm{d}r}{\sqrt{R(r)}} \,, \tag{4.5}$$

$$\begin{aligned} \psi_o - \psi_s =& \nu_r \int_{r_s}^{r_o} \frac{a(2mr - a\lambda - \sqrt{R(r)})}{\Delta\sqrt{R(r)}} \,\mathrm{d}r \\ &+ \nu_\theta \int_{\theta_s}^{\theta_o} \frac{\lambda}{\sin^2(\theta)\sqrt{\Theta(\theta)}} \,\mathrm{d}\theta \,, \end{aligned} \tag{4.6}$$

$$\begin{aligned} u_o - u_s =& \nu_r \int_{r_s}^{r_o} \frac{r^2\Delta + 2mr(r^2 + a^2 - a\lambda) - (r^2 + a^2)\sqrt{R(r)}}{\Delta\sqrt{R(r)}} \,\mathrm{d}r \\ &+ \nu_\theta \, a^2 \int_{\theta_s}^{\theta_o} \frac{\cos^2\theta}{\sqrt{\Theta(\theta)}} \,\mathrm{d}\theta \,. \end{aligned} \tag{4.7}$$

Notice that equation (4.5) couples the r- and θ-motion. This is due to the fact that both the left-hand-side as well as the right-hand-side are equal to the elapsed Mino time τ along the geodesic. We will use this fact later by fixing the source's radial position r_s in addition to the observer's location and thus being able to calculate the polar angle of the source θ_s. The equations (4.5)-(4.7) are the general integral equations of motion for a null geodesic in Kerr spacetime. However, as mentioned above, we will restrict ourselves to the subclass of vortical null geodesics which have no turning points in the radial direction to solve the equations analytically. Accordingly, the radial potential $R(r)$ never vanishes along the geodesic and thus all its four roots are complex. In the case of no real roots, a quartic polynomial (such as $R(r)$ is) has pairs of complex roots, meaning that for the roots r_i ($i = 1, 2, 3, 4$) of $R(r)$ we can arrange that $r_1 = \bar{r_2}$ and $r_3 = \bar{r_4}$ (where the bar denotes complex conjugation). In the case of $R(r)$ this was shown to hold true for vortical null geodesics by [17] where they also calculated an especially compact analytic form of the roots of $R(r)$ which we will use (the formulas thereof are reproduced in Appendix A.1). Sometimes it can be useful to write the radial potential as $R(r) = (r - r_1)(r - r_2)(r - r_3)(r - r_4)$.
As a consequence of the radial potential $R(r)$ only possessing complex-valued roots, the denominator of the r-integral in (4.5)-(4.7) either does not vanish at all or only at the horizons. This singularity at $\Delta = 0$ is counteracted by the regularising transformation to Eddington-Finkelstein-like coordinates, meaning that as the denominator approaches zero, so does the numerator.
Lastly, a few words about the general approach of calculating the starting values of a geodesic which hit the observer's photographic plate (at certain impact parameters α and β). The fact that we want to fix the observer's position and the impact parameters results in the necessity of calculating the geodesic trajectory "back in time". Thus, what we really calculate is the trajectory of a vortical null geodesic which starts from the observer at $r_o = -\infty$ and some α and β inside the inner throat, and ends at the source at $r_s > 0$. We are allowed to do this because this is equivalent to an exchange of the integration boundaries. In our case we can thus also "integrate backwards" by a simple flip of the sign ν_r. One only needs to be careful when interpreting the geodesic trajectories and transforming them to Kerr-Schild coordinates. Some aspects of this will be discussed at the beginning of the next chapter 5. As this is the standard approach in many black hole visualisations (see e.g. [19] or [16]), we will adopt it here.

4.1. Analytic solutions

In this section we will present the analytic solution of the integral equations of motion. To this effect, as already mentioned earlier, we will mainly follow [17] but instead use Eddington-Finkelstein-like coordinates (u, r, θ, ψ) over Boyer-Lindquist coordinates (t, r, θ, φ) to enable the resulting vortical null geodesics to cross the horizons. The primary method used to solve the equations is to reduce them to elliptic integrals. In section 4.2 we will then solve the integrals numerically, with the results being used to cross-check the validity of the analytic formulas on a numerical basis. The actual working progress was that these two sections were done in parallel, resulting in finding discrepancies in some of the integrals used by [17].
The antiderivatives of the integral equations of motion are calculated in a general setting for vortical null geodesics with no radial turning points, i.e. we do not yet specify the source's or the observer's location. Only later when implementing the solutions in Mathematica, we may take the limit $r_o \to -\infty$ and $r_s \to +\infty$ to speed up numerical calculations.
In order to follow [17] in the calculation of the antiderivatives and hence allowing a comparison of this thesis and their work, we need to define some additional quantities which can be found in Appendix A.1. Included are formulas for the roots r_i $(i = 1, 2, 3, 4)$ of the radial potential, as well as for a_1, a_2, b_1, b_2, C, D, g_0, k, k_4, $x_4(r)$, h, and $X_4(\tau)$. We will also define the integrals

$$I_\pm = \nu_r \int_{r_s}^{r_o} \frac{\mathrm{d}r}{(r - r_\pm)\sqrt{R(r)}} \,, \tag{4.8}$$

$$I_\ell = \nu_r \int_{r_s}^{r_o} \frac{r^\ell \,\mathrm{d}r}{\sqrt{R(r)}} \tag{4.9}$$

in the same way as [17]. In the following $\mathcal{I}$ will always denote the antiderivative of an integral I, so e.g. $\mathcal{I}_\pm$ is the antiderivative of $I_\pm = \mathcal{I}_\pm(r_o) - \mathcal{I}_\pm(r_s)$.
To start off the section, we will give a very brief introduction into the theory of elliptic integrals for the readers who may not be well-versed in this topic, mainly giving only definitions and some relations. An extensive discussion of elliptic integrals/functions and their relations and properties can be found in e.g. [1] or [15], on which the next subsection is based.

4.1.1. Brief intermezzo on elliptic integrals and Jacobi elliptic functions

Elliptic Integrals

An integral of the form

$$\int R(x, y)\,\mathrm{d}x$$

is called an elliptic integral if $R(x, y)$ is rational and $y = \sqrt{P(x)}$ where $P(x)$ is a polynomial either cubic or quartic in x. In the general case, these integrals cannot be solved using elementary functions. All elliptic integrals can be reduced to an integral of a rational function and three canonical elliptic integrals, which are known as the elliptic integrals of the first, second, and third kind. Due to this, it is worth while studying these canonical

forms, which are defined as

$$\text{First Kind}: \qquad F[\varphi, m] := \int_0^{\varphi} \frac{\mathrm{d}\theta}{\sqrt{1 - m\sin^2\theta}} \,, \tag{4.10}$$

$$\text{Second Kind}: \qquad E[\varphi, m] := \int_0^{\varphi} \sqrt{1 - m\sin^2\theta}\,\mathrm{d}\theta \,, \tag{4.11}$$

$$\text{Third Kind}: \qquad \Pi[n, \varphi, m] := \int_0^{\varphi} \frac{\mathrm{d}\theta}{(1 - n\sin^2\theta)\sqrt{1 - m\sin^2\theta}} \,. \tag{4.12}$$

Note that [1] and [15] use different conventions for the arguments m of $F[\varphi, m]$, $E[\varphi, m]$ and $\Pi[n, \varphi, m]$. The formulas differ from (4.10)-(4.12) only by exchanging $m \to k = \sqrt{m}$ in the arguments on the left-hand side, while on the right-hand sides we have $m \to k^2$. These forms are obviously equivalent but since we later want to implement the solutions of the integral equations of motion (expressed in terms of these canonical elliptic integrals) into Mathematica, we adapt here the convention built into Mathematica (which is the one used in (4.10)-(4.12)).
The canonical elliptic integrals are all odd functions in φ satisfying $F[-\varphi, m] = -F[\varphi, m]$, $E[-\varphi, m] = -E[\varphi, m]$, as well as $\Pi[n, -\varphi, m] = -\Pi[n, \varphi, m]$. In the general case $\varphi \neq \pi/2$ the integrals (4.10)-(4.12) are called incomplete canonical elliptic integrals. For $\varphi = \pi/2$ we call them complete canonical elliptic integrals and denote them by

$$\text{First Kind}: \qquad K[m] := F\left[\frac{\pi}{2}, m\right] = \int_0^{\pi/2} \frac{\mathrm{d}\theta}{\sqrt{1 - m\sin^2\theta}} \,, \tag{4.13}$$

$$\text{Second Kind}: \qquad E[m] := E\left[\frac{\pi}{2}, m\right] = \int_0^{\pi/2} \sqrt{1 - m\sin^2\theta}\,\mathrm{d}\theta \,, \tag{4.14}$$

$$\text{Third Kind}: \qquad \Pi[n, m] := \Pi\left[n, \frac{\pi}{2}, m\right] = \int_0^{\pi/2} \frac{\mathrm{d}\theta}{(1 - n\sin^2\theta)\sqrt{1 - m\sin^2\theta}} \,. \tag{4.15}$$

In the following we will drop the term "canonical" as well as the specification complete/incomplete. This will always be clear from the notation and/or the context.

Jacobi Elliptic Functions

Based on the elliptic integrals, one can define inverse functions as follows. Let $u = F[\varphi, m]$ be the elliptic integral of the first kind. We define

$$\mathrm{am}[u, m] := \varphi \tag{4.16}$$

to be the inverse of $F[\varphi, m]$, thus considering φ to be a function of u. $\mathrm{am}[u, m]$ is called Jacobi amplitude and by definition we have $F\left[\mathrm{am}[u, m], m\right] = u$. From this we can construct three further Jacobi elliptic functions

$$\mathrm{sn}[u, m] = \sin(\mathrm{am}[u, m]) = \sin(\varphi) \,, \tag{4.17}$$

$$\mathrm{cn}[u, m] = \cos(\mathrm{am}[u, m]) = \cos(\varphi) \,, \tag{4.18}$$

$$\mathrm{dn}[u, m] = \sqrt{1 - m\sin^2(\mathrm{am}[u, m])} = \sqrt{1 - m\sin^2(\varphi)} \,, \tag{4.19}$$

which are called sine-amplitude, cosine-amplitude, and delta-amplitude, respectively. From the definition it follows immediately that $\mathrm{sn}^2[u, m] + \mathrm{cn}^2[u, m] = 1$ and $\mathrm{dn}^2[u, m] + m\,\mathrm{sn}^2[u, m] = 1$.

The functions $\mathrm{sn}[u,m]$ and $\mathrm{cn}[u,m]$ are periodic in u with period $4K[m]$, whereas $\mathrm{dn}[u,m]$ is $2K[m]$-periodic. Here, $K[m]$ is the complete elliptic integral of the first kind. Another constructible function we need later is

$$\mathrm{sc}[u,m] = \frac{\mathrm{sn}[u,m]}{\mathrm{cn}[u,m]} \,. \tag{4.20}$$

To make subsequent equations involving elliptic integrals and elliptic function easier to read, we will consistently use square brackets for their arguments. For all other purposes involving brackets, we will utilise different brackets.

4.1.2. τ-integral

To get a solution for the Mino time along the geodesic, we can take two approaches, one where τ will depend on the polar angle $\theta_{s/o}$ and one where it will depend on the radius $r_{s/o}$. We will follow the latter strategy for which we rewrite (4.1) as

$$\mathrm{d}\tau = \nu_r \frac{\mathrm{d}r}{\sqrt{R(r)}} \,. \tag{4.21}$$

By path integrating from the source to the observer we get

$$\tau_o - \tau_s = \nu_r \int_{r_s}^{r_o} \frac{\mathrm{d}r}{\sqrt{R(r)}} \,. \tag{4.22}$$

Using the definition (4.9) from above, we see that the right-hand side is equal to I_0. One can look up the antiderivative of this when integrating from some y_1 up to r in e.g. [15] §3.145 with the result being (note that this integral table uses a different convention of elliptic integrals)

$$\mathcal{I}_0(r) = \frac{2\,\nu_r}{C+D}\, F[\arctan(x_4(r)) + \arctan(g_0),\, k_4] \,. \tag{4.23}$$

Thus we can construct the integral in (4.22) as being the integral $\int_{r_s}^{r_o} = \int_{r_s}^{y_1} + \int_{y_1}^{r_o} = \int_{y_1}^{r_o} - \int_{y_1}^{r_s}$. Consequently, (4.23) is the antiderivative of the integral in (4.22) and we can write

$$\tau_o = \tau_s + \mathcal{I}_0(r_o) - \mathcal{I}_0(r_s) \,, \tag{4.24}$$

which is our general solution for the Mino time τ_o along the geodesic in dependence of the radial position of the source r_s and of the observer r_o as well as the starting time τ_s. In the cases when we are only interested in the elapsed Mino time along the geodesic we can set $\tau_s = 0$ as our starting point at the light source.

4.1.3. r-integral

To get a formula for the radial component of a vortical null geodesic, the authors of [17] inverted (4.24) by using the basic properties of elliptic integrals and elliptic functions to get a formula for $r_o(\tau)$. Since the transformation to Eddington-Finkelstein-like coordinates does not change the equations for τ and r, our calculation would yield the exact same

result. For that reason we adopt the result for the radial coordinate presented in [17] (where a full derivation can be found in Appendix B Section 4). The final formula is

$$r_o(\tau) = -a_2 \left(\frac{g_0 - \mathrm{sc}[X_4(\tau), k_4]}{1 + g_0 \, \mathrm{sc}[X_4(\tau), k_4]} \right) - b_1 \ , \tag{4.25}$$

which depends implicitly on the source's radial position r_s and the initial direction ν_r via $X_4(\tau)$.
This formula is useful for us because with (4.24) we can first calculate the final Mino time of the geodesic, i.e. when the geodesic reaches the observer, while with (4.25) we can "track" the geodesic along its path of increasing Mino time. Thus we can calculate the null geodesic's radial position for all times between the emission of the photon at τ_s and the observation of it at τ_o. An example trajectory with $r_s = -\infty$, $r_o = +\infty$ and $\theta_s = \pi/4$ can be found in Fig. 4.1. To avoid confusion we again want to stress that we integrate from the observer to the source. Therefore, in Fig. 4.1 the geodesic starts at $r_s = -\infty$ at $\tau = 0$ and is terminated at $r_o = +\infty$ (in contrast to the setup given in the beginning of this chapter). This is no big problem as τ is only a parameter along the geodesic, and thus we can simply mirror and shift these plots such that they start at $r_o = +\infty$ at $\tau = 0$ and end at $r_s = -\infty$. Hence, we recover our setup from the beginning of this section. The same procedure is followed in all the other subsections of this chapter where it applies.
The impact parameters $\alpha = -0.15$ and $\beta = 0.1$ are chosen somewhat arbitrarily, with the only requirement that these points lie inside the inner throat. One can verify that the point ($\alpha = -0.15$, $\beta = 0.1$) really lies inside the inner throat by Fig. 5.9, which will be discussed in section 5.1. The left of the two plots in Fig. 4.1 shows the actual radial trajectory (normalised by the black hole's mass parameter m) while the right one shows the trajectory of $\arctan(r/m)$. This rescaled version will later be useful for numeric integration since it captures the infinities $r = \pm\infty$ in the finite values $\arctan(r) = \pm\pi/2$.

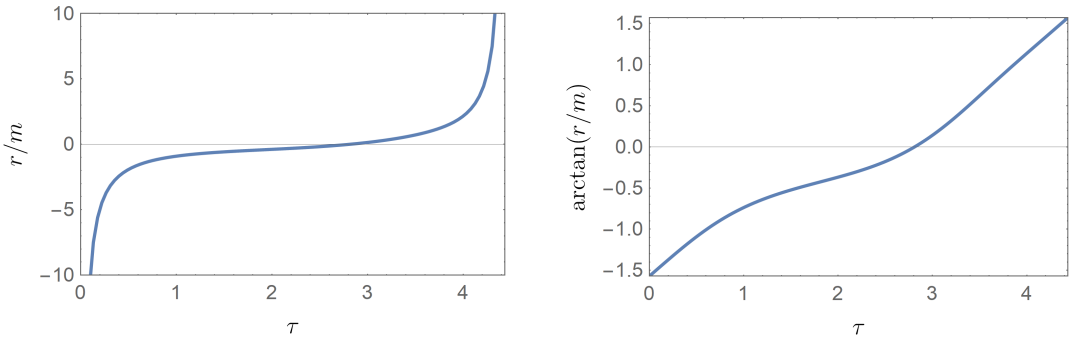

Figure 4.1.: An example radial trajectory of a vortical null geodesic with impact parameters $\alpha = -0.15$ and $\beta = 0.1$. The rotation parameter is set to $a/m = 0.99$. Because we measure distances in terms of the black hole's mass m, we are plotting r/m and $\arctan(r/m)$.

4.1.4. θ-integral

With the solution for the polar angle we proceed similarly to the subsection before in the sense that we just state the final formula as it was derived in [17] and leave out the details,

which, in the case of vortical null geodesics, can be found in [17] Section III B. Accordingly, the formula for the polar angle is given by

$$\theta_o(\tau) = \arccos\left(h\sqrt{u_-}\,\mathrm{dn}\left[\sqrt{u_-\,a^2}\left(\tau + \nu_\theta\,\mathcal{G}_\theta(\theta_s)\right),\, 1 - \frac{u_+}{u_-}\right]\right)\,, \tag{4.26}$$

where $h = \mathrm{sign}(\cos\theta_s)$, $u_\pm$ is defined as in (3.50), and $\mathcal{G}_\theta(\theta)$ is given by

$$\mathcal{G}_\theta(\theta) = -\frac{h}{\sqrt{u_-\,a^2}}\,F\left[\arcsin\left(\sqrt{\frac{\cos^2\theta - u_-}{u_+ - u_-}}\right),\, 1 - \frac{u_+}{u_-}\right]\,. \tag{4.27}$$

Using this formula we can calculate the θ-trajectory of any geodesic with impact parameters inside the inner throat. We can use the general periodicity properties of the elliptic function presented in subsection 4.1.1 to determine the period of the polar angle.

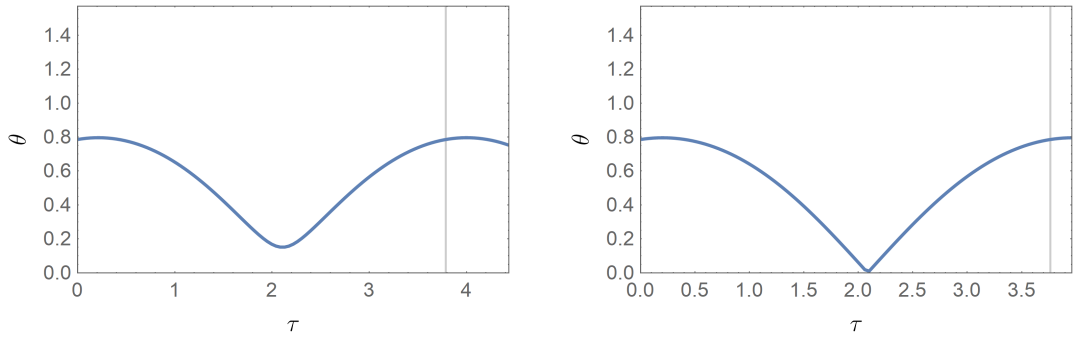

(a) $\alpha = -0.15$, $\beta = 0.1$ (b) $\alpha = 0$, $\beta = 0.1$

Figure 4.2.: Two example θ-trajectories calculated with (4.26) with $r_s = -\infty$, $r_o = +\infty$ and $\theta_s = \pi/4$. (a) It is smooth in the general case $\alpha \neq 0$. (b) For $\alpha = 0$ the trajectory is not smooth at $\theta_- = 0$. The rotation parameter is set to $a/m = 0.99$ in both plots. The vertical line denotes one full period of θ.

However, there is a problem with the smoothness for geodesics with $\alpha = 0$, which can be seen in Fig. 4.2b. In the next chapter we will see that this case corresponds to geodesics going through the axis of symmetry. In the general case $\alpha \neq 0$ the trajectory oscillates smoothly between θ_+ and θ_-, thus staying in one hemisphere (in the example in Fig. 4.2a in the northern hemisphere characterised by $\mathrm{sign}(\cos\theta_s) = 1$). Recall that Fig. 3.8 and the discussion thereof in subsection 3.2.2 showed us that for $\alpha = 0$ we have $\theta_- = 0$, meaning that such a geodesic reaches the axis of symmetry. Keeping that in mind, we see that a trajectory whose impact parameter α approaches zero (i.e. going from Fig. 4.2a to Fig. 4.2b), the turning point at θ_- loses its smooth nature and develops into a cusp. In order for the trajectory to stay smooth along its path from the source to the observer, we extend it to negative values of θ, thus the oscillation takes place in the range $-\theta_+ \leq \theta \leq \theta_+$. This extension is achieved by flipping the sign of the right-hand side in (4.26) for certain ranges of Mino time τ along the geodesic which are specified using the periodicity properties of the elliptic function $\mathrm{dn}[u, m]$. We are allowed to alter (4.26) in this way without getting problems with it being the antiderivative to (4.2) because of the ambiguity in the inverse of cosine (which is used in the derivation).

In order to implement this modification, we can calculate at which Mino time τ the solution for $\theta(\tau)$ becomes zero, i.e. we solve the equation $\theta(\tau) = 0$ for τ. Doing so gives us

$$\tau_0 = \frac{1}{a\sqrt{u_-}} F\left[arcsin\left(\sqrt{\frac{u_- - 1}{u_- - u_+}}\right), 1 - \frac{u_+}{u_-}\right] - \nu_\theta \mathcal{G}_\theta(\theta_s) , \tag{4.28}$$

where we used $a > 0$. By inserting the special case $\alpha = \lambda = 0$ into equation (3.48) for $u_\pm$, we get $u_+ = 1$ and $u_- = -\eta/a^2$. This, in turn, simplifies (4.29), yielding

$$\tau_0 = \frac{1}{a\sqrt{u_-}} K\left[\frac{u_- - 1}{u_-}\right] - \nu_\theta \mathcal{G}_\theta(\theta_s) . \tag{4.29}$$

Based on the periodicity of $\mathrm{dn}[u, m]$ we can deduce that the sign of the right hand side of equation (4.26) needs to be flipped for

$$\frac{1+4m}{a\sqrt{u_-}} K\left[\frac{u_- - 1}{u_-}\right] - \nu_\theta \mathcal{G}_\theta(\theta_s) < \tau < \frac{3+4m}{a\sqrt{u_-}} K\left[\frac{u_- - 1}{u_-}\right] - \nu_\theta \mathcal{G}_\theta(\theta_s) , \tag{4.30}$$

with $m \in \mathbb{R}$.
The modified trajectory in the case of Fig. 4.2b can be seen in Fig. 4.3. Notice that also in this case the hemisphere does not change since $h = \mathrm{sign}(\cos(\theta)) = \mathrm{sign}(\cos(-\theta))$ and the geodesic never crosses the equatorial plane at $\theta = \pi/2$.
The modified analytic solution coincides with the numerical solution (discussed in section 4.2) which confirms the need for this correction on a numerical basis.

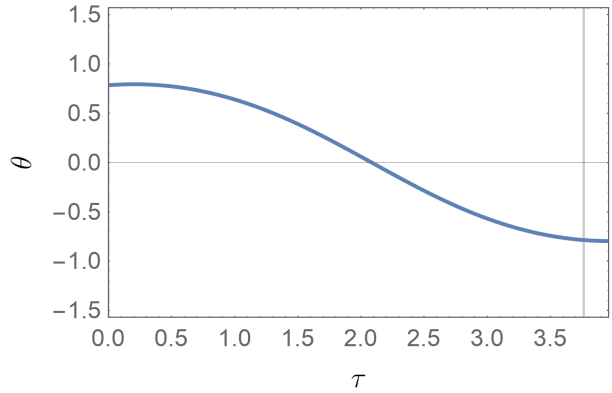

Figure 4.3.: We can smooth out the polar angle trajectory for geodesics with $\alpha = 0$ by extending it to negative θ. The hemisphere defined by $\mathrm{sign}(\cos\theta)$ stays the same throughout. The plotted trajectory has impact parameters ($\alpha = 0$, $\beta = 0.1$). In this case the vertical line denotes one half-period of the polar angle.

There is another approach to get smooth trajectories of the geodesic when combining all solutions for r, θ, ψ, and u (i.e. the trajectory in Kerr-Schild coordinates should ultimately be smooth – see subsection 5.1.4), which does not involve altering the solution for θ. To this end we would need to artificially introduce a discontinuity in the solution for ψ at the point where the polar angle gets reflected at $\theta_- = 0$ (see subsection 4.1.5). The reader can easily convince themself that this is true because θ is the polar and ψ is the azimuthal angle. Therefore, a trajectory going through the axis of symmetry can

be achieved by either allowing negative values of the polar angle or by a "jump" in the azimuthal angle by π, both resulting in the same trajectory in Cartesian coordinates (in our case pseudo-Cartesian coordinates in the form of Kerr-Schild coordinates). We did not choose this second strategy since the first one seems more natural.

4.1.5. ψ-integral

To get a solution for the ψ-integral, it is useful to write (4.6) in the form

$$\psi_o - \psi_s = I_\psi + \lambda\, G_\varphi \tag{4.31}$$

where we defined

$$I_\psi := I_\varphi - I_{reg,\varphi}\ , \tag{4.32}$$

$$I_\varphi := \nu_r \int_{r_s}^{r_o} \frac{a(2mr - a\lambda)}{\Delta\sqrt{R(r)}}\,\mathrm{d}r\ , \tag{4.33}$$

$$I_{reg,\varphi} := \nu_r \int_{r_s}^{r_o} \frac{a}{\Delta}\,\mathrm{d}r\ , \tag{4.34}$$

$$G_\varphi := \nu_\theta \int_{\theta_s}^{\theta_o} \frac{\mathrm{d}\theta}{\sin^2\theta\sqrt{\Theta(\theta)}}\ . \tag{4.35}$$

The regularisation integral (4.34) appears due to the coordinate transformation from Boyer-Lindquist to Eddington-Finkelstein-like coordinates. We can follow [17] and rewrite I_φ as

$$I_\varphi = \frac{2ma}{r_+ - r_-}\left[\left(r_+ - \frac{a\lambda}{2m}\right)I_+ - \left(r_- - \frac{a\lambda}{2m}\right)I_-\right]\ , \tag{4.36}$$

where $I_\pm$ are defined in (4.8). The calculation how to get from (4.33) to (4.36) is shown in appendix A.2. The resulting formula for ψ_o is

$$\psi_o = \psi_s + \frac{2ma}{r_+ - r_-}\left[\left(r_+ - \frac{a\lambda}{2m}\right)I_+ - \left(r_- - \frac{a\lambda}{2m}\right)I_-\right] - I_{reg,\varphi} + \lambda G_\varphi\ . \tag{4.37}$$

The task of finding a solution for the azimuthal angle ψ is now reduced to finding the antiderivatives of (4.8), (4.34), and (4.35). Let us begin with the least problematic one, which is the antiderivative of (4.35). As was shown in [17], this integral in terms of elliptic integrals equates to

$$G_\varphi = \frac{1}{(1-u_-)\sqrt{u_-\,a^2}}\,\Pi\left[\frac{u_+ - u_-}{1-u_-}, \Upsilon_\tau,\, 1 - \frac{u_+}{u_-}\right] - \nu_\theta\,\mathcal{G}_\varphi(\theta_s) \tag{4.38}$$

where they introduced

$$\Upsilon_\tau = \mathrm{am}\left[\sqrt{u_-\,a^2}\ (\tau + \nu_\theta\,\mathcal{G}_\theta(\theta_s))\,,\, 1 - \frac{u_+}{u_-}\right]\ , \tag{4.39}$$

$$\mathcal{G}_\varphi(\theta) = -\frac{h}{(1-u_-)\sqrt{u_-\,a^2}}\,\Pi\left[\frac{u_+ - u_-}{1-u_-}, \arcsin\left(\sqrt{\frac{\cos^2\theta - u_-}{u_+ - u_-}}\right), 1 - \frac{u_+}{u_-}\right]\ , \tag{4.40}$$

and where the definitions of $\mathcal{G}_\theta(\theta)$ and $u_\pm$ are given in (4.27) and (3.50), respectively. Instead of using τ in G_φ we could also use both θ_s and θ_o and calculate $G_\varphi = \nu_\theta \left(\mathcal{G}_\varphi(\theta_o) - \mathcal{G}_\varphi(\theta_s)\right)$. Taking this approach would not allow us to calculate θ_o and ψ_o in parallel, therefore we will use (4.38).
In the next step we will calculate the antiderivative of (4.34), which can easily checked to be

$$\mathcal{I}_{reg,\varphi} = \nu_r \frac{a\left(\ln(r-r_+) - \ln(r-r_-)\right)}{r_+ - r_-} \,. \tag{4.41}$$

Lastly, finding an antiderivative to (4.8) turned out to be actually kind of tricky. The reason for this is that we were not able to confirm the antiderivative found by [17] when cross-checking it with the numerical integration. To the best of our knowledge there seems to be a mistake somewhere in the formulas presented, be it some typo, a calculation error, or that the integral table they used was faulty. Thus, we calculated it anew using Mathematica, which gave the result

$$\begin{aligned}\mathcal{I}^1_\pm(r) =& \frac{\nu_r i(r_2 - r_\pm)}{\sqrt{a_1 a_2}(r_1 - r_\pm)(r_3 - r_\pm)} \, F\left[\arcsin\left(\sqrt{\frac{2ia_2(r-r_3)}{(r-r_1)(r_2-r_3)}}\right), \frac{D^2}{4a_1a_2}\right] \\ &+ \frac{\nu_r i(r_2 - r_\pm)(r_1 - r_3)}{\sqrt{a_1 a_2}(r_1 - r_\pm)(r_3 - r_\pm)} \\ &\times \Pi\left[\frac{(r_2-r_3)(r_1-r_\pm)}{2ia_2(r_3-r_\pm)}, \arcsin\left(\sqrt{\frac{2ia_2(r-r_3)}{(r-r_1)(r_2-r_3)}}\right), \frac{D^2}{4a_1a_2}\right]\end{aligned} \tag{4.42}$$

with $D^2 = (a_1 + a_2)^2 + (b_1 - b_2)^2$. This function is not continuous over the whole range of r – as it turns out it has a discontinuity just below $r = 0$. We can correct for this by introducing an integration constant which includes two Heaviside functions $H[\,\cdot\,]$ as well as the complete elliptic integrals. This integration constant has the form

$$\begin{aligned}c_{corr,\varphi}(r) =& -2\nu_r H[-r] \, H\left[-Im\left(\arcsin\left(\sqrt{\frac{2ia_2(r-r_3)}{(r-r_1)(r_2-r_3)}}\right)\right)\right] \times \\ &\times \left(\frac{i(r_2 - r_\pm)}{\sqrt{a_1 a_2}(r_1 - r_\pm)(r_3 - r_\pm)} K\left[\frac{D^2}{4a_1a_2}\right]\right. \\ &\left. + \frac{i(r_2 - r_\pm)(r_1 - r_3)}{\sqrt{a_1 a_2}(r_1 - r_\pm)(r_3 - r_\pm)} \Pi\left[\frac{(r_2-r_3)(r_1-r_\pm)}{2ia_2(r_3-r_\pm)}, \frac{D^2}{4a_1a_2}\right]\right)\end{aligned} \tag{4.43}$$

and needs to be added to (4.42) to give a smooth solution for all values of r. We finally arrive at an equation for the antiderivative of $I_\pm$

$$\mathcal{I}_\pm(r) = \mathcal{I}^1_\pm(r) + c_{corr,\varphi}(r) \,, \tag{4.44}$$

which coincides with numerical integration over the whole range of r.
Now we are able to compute ψ_o with (4.37) using (4.38) as well as the antiderivatives (4.41) and (4.44). To calculate it numerically, we further need to specify the impact parameters α and β of the geodesic and whether its initially in- or outgoing ($\nu_r = \pm 1$), the black hole parameters m and a, as well as the beforehand calculated values r_s, r_o, θ_o, τ_s and τ_o.
An example of an azimuthal trajectory can be found in Fig. 4.4, where we again used

$r_s = -\infty$, $r_o = +\infty$ and $\theta_s = \pi/4$. The grey horizontal line in the plot lies at $\psi = -2\pi$, which, naively thinking, would correspond to one whole revolution of the geodesic "around" the black hole, or more precisely around the axis of symmetry. One might be tempted to define the geodesic's order based on this. However, in section 6.1 we will see that there is a different approach which leads to the desired characterisation of the order of a geodesic.

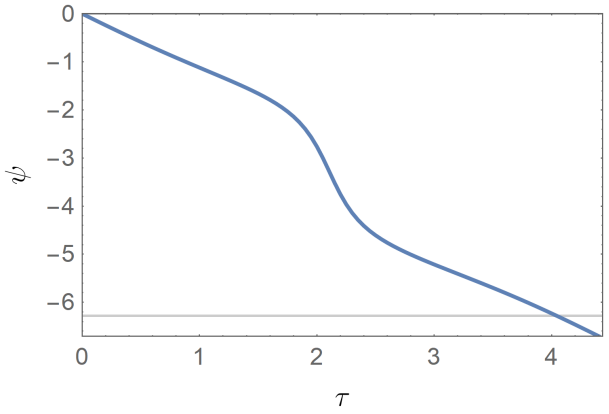

Figure 4.4.: An example azimuthal angle trajectory for a geodesic with ($\alpha = -0.15, \beta = 0.1$). The black hole's rotation parameter is set to $a/m = 0.99$. The grey horizontal line is at $\psi = -2\pi$.

4.1.6. u-integral

Solving the u-equation (4.7) is very similar to solving the ψ-equation (4.6). We once more begin by rewriting the integral equation (4.7) in a simpler form

$$u_o - u_s = I_u + a^2 G_t \,, \tag{4.45}$$

where we defined

$$I_u := I_t - I_{reg,t} \,, \tag{4.46}$$

$$I_t := \nu_r \int_{r_s}^{r_o} \frac{r^2\Delta + 2mr(r^2 + a^2 - a\lambda)}{\Delta\sqrt{R(r)}}\,\mathrm{d}r \,, \tag{4.47}$$

$$I_{reg,t} := \nu_r \int_{r_s}^{r_o} \frac{r^2 + a^2}{\Delta}\,\mathrm{d}r \,, \tag{4.48}$$

$$G_t := \nu_\theta \int_{\theta_s}^{\theta_o} \frac{\cos^2\theta}{\sqrt{\Theta(\theta)}}\,\mathrm{d}\theta \,. \tag{4.49}$$

The regularisation integral $I_{reg,t}$ is the result of the coordinate transformation from Boyer-Lindquist to Eddington-Finkelstein-like coordinates. As before, we can follow the approach in [17] and rewrite I_t as

$$I_t = \frac{(2m)^2}{r_+ - r_-}\left[r_+\left(r_+ - \frac{a\lambda}{2m}\right) I_+ - r_-\left(r_- - \frac{a\lambda}{2m}\right) I_-\right] + (2m)^2\, I_0 + 2m\, I_1 + I_2 \,. \tag{4.50}$$

Again, the calculation how to get from (4.47) to (4.50) is shown in appendix A.2. The integrals $I_\pm$ and I_ℓ (with $\ell = 0, 1, 2$) are defined in (4.8) and (4.9), respectively. Thus, to

get a solution for u, we need find solutions to (4.8), (4.9), (4.48), as well as (4.49). Luckily for us, we have solved (4.8) in the previous subsection, so we do not need to worry about this integral anymore. Next, we can take the solution of (4.49) as it was solved in [17] (specifically in Section III B). They found that for vortical null geodesics one gets

$$G_t = \sqrt{\frac{u_-}{a^2}}\, E\left[\Upsilon_\tau,\, 1-\frac{u_+}{u_-}\right] - \nu_\theta\, \mathcal{G}_t(\theta_s)\,, \tag{4.51}$$

where Υ_τ is defined as in (4.39), and where they introduced

$$\mathcal{G}_t(\theta) = -h\sqrt{\frac{u_-}{a^2}}\, E\left[\arcsin\left(\sqrt{\frac{\cos^2\theta - u_-}{u_+ - u_-}}\right),\, 1-\frac{u_+}{u_-}\right]\,. \tag{4.52}$$

Next, it is straightforward to get the antiderivative for $I_{reg,t}$, which can be checked to be

$$\mathcal{I}_{reg,t}(r) = \nu_r\left(r + \frac{a^2+r_-^2}{r_- - r_+}\ln(r-r_-) - \frac{a^2+r_+^2}{r_- - r_+}\ln(r-r_+)\right)\,. \tag{4.53}$$

This leaves us with the task to solve I_ℓ for $\ell = 0,1,2$, which we will solve similar to above. Let us begin with the antiderivative of I_0, for which we could confirm that the solution presented in [17] coincides with numerical integration. The correct solution is (4.23) as it was already used in subsection 4.1.2 for the solution for the Mino time.
Next, since we could not confirm the formulas for $\mathcal{I}_1$ and $\mathcal{I}_2$ given in [17], we calculate these antiderivatives anew using Mathematica, for which we get

$$\begin{aligned}\mathcal{I}_1(r) =& \nu_r\sqrt{\frac{4}{(r_2-r_4)(r_3-r_1)}}\left(2a_1\,\Pi\left[\frac{r_4-r_1}{r_3-r_1},\, \arcsin\left(\sqrt{\frac{(r_3-r_1)(r-r_4)}{(r_4-r_1)(r-r_3)}}\right),\, k\right]\right.\\ &\left. - ir_3\, F\left[\arcsin\left(\sqrt{\frac{(r_3-r_1)(r-r_4)}{(r_4-r_1)(r-r_3)}}\right),\, k\right]\right)\\ &- 2\nu_r H[-r]H\left[-Im\left(\arcsin\left(\sqrt{\frac{(r_3-r_1)(r-r_4)}{(r_4-r_1)(r-r_3)}}\right)\right)\right] Re\left(2a_1\,\Pi\left[\frac{r_4-r_1}{r_3-r_1},\, k\right] - ir_3\, K[k]\right)\,,\end{aligned} \tag{4.54}$$

$$\begin{aligned}\mathcal{I}_2(r) =& \nu_r\left\{(r-r_1)\sqrt{\frac{(r-r_4)(r-r_2)}{(r-r_1)(r-r_3)}}\right.\\ &- \sqrt{(r_3-r_1)(r_4-r_2)}\, E\left[\arcsin\left(\sqrt{\frac{(r_3-r_1)(r-r_4)}{(r_4-r_1)(r-r_3)}}\right),\, k\right]\\ &\left. + \sqrt{\frac{4}{(r_4-r_2)(r_3-r_1)}}\,(b_1^2 - a_1a_2)\, F\left[\arcsin\left(\sqrt{\frac{(r_3-r_1)(r-r_4)}{(r_4-r_1)(r-r_3)}}\right),\, k\right]\right\}\\ &- 2\nu_r H[-r]H\left[-Im\left(\arcsin\left(\sqrt{\frac{(r_3-r_1)(r-r_4)}{(r_4-r_1)(r-r_3)}}\right)\right)\right]\\ &\times Re\left(-\sqrt{(r_3-r_1)(r_4-r_2)}\, E[k] + \sqrt{\frac{4}{(r_4-r_2)(r_3-r_1)}}\,(b_1^2-a_1a_2)\, K[k]\right)\,,\end{aligned} \tag{4.55}$$

where the last term in each formula is the correction constant to ensure a smooth trajectory for all values of r.
With these solutions we can write

$$I_\ell = \mathcal{I}_\ell(r_o) - \mathcal{I}_\ell(r_s) \ , \tag{4.56}$$

for $\ell \in \{1, 2\}$, and together with (4.23) and the solution for $I_\pm$ from the last subsection we can find an analytical solution for (4.50). Finally, also using (4.51) and (4.53) we can get a formula for u_o in (4.45). To calculate the coordinate time u_o along the geodesic, we further need to specify u_s; to get the elapsed coordinate time u_o along the geodesic, we set $u_s = 0$. As in the case for ψ_o, to calculate u_o numerically, we need to also specify α, β, ν_r, m, a and the beforehand calculated values for r_s, r_o, θ_o, τ_s and τ_o. Such a trajectory can be found in Fig. 4.5, which starts at $r_s = -\infty$ and $\theta_s = \pi/4$ and ends at $r_o = +\infty$.

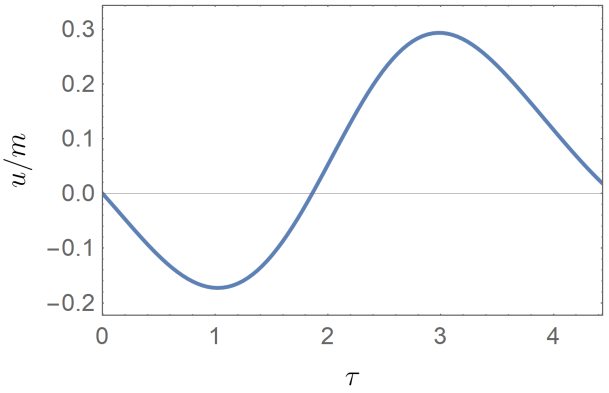

Figure 4.5.: An example u-trajectory for a geodesic with ($\alpha = -0.15$, $\beta = 0.1$). The black hole's rotational parameter is $a/m = 0.99$. Because we measure time in terms of the black hole's mass m, we are plotting u/m.

4.2. Numerical solution

To solve the system of differential equations (4.1)-(4.4) numerically, we make a few adjustments. For one, we will use the second order differential equation for r and θ, which will avoid possible problems when encountering turning points in the radial or polar direction. We get

$$\frac{\mathrm{d}^2 r}{\mathrm{d}\tau^2} = \frac{1}{2}\frac{\mathrm{d}R(r)}{\mathrm{d}r} \ , \tag{4.57}$$

$$\frac{\mathrm{d}^2 \theta}{\mathrm{d}\tau^2} = \frac{1}{2}\frac{\mathrm{d}\Theta(\theta)}{\mathrm{d}\theta} \ , \tag{4.58}$$

where we simplified the formulas using the original first order equations.
Furthermore, due to the nature of numerical integration, it is wise to avoid infinities wherever it is possible. Thus we will remove the infinity from the radial equation by making the coordinate change $x = \arctan(r)$ and solve the equation for the coordinate $x(\tau)$. For this new "radial" coordinate we can identify $r = \pm\infty$ with $x = \pm\pi/2$. In the

end we effectively want to solve the following system of differential equations:

$$\frac{\mathrm{d}^2x}{\mathrm{d}\tau^2} = \cos(x(\tau))\Big(((a-\lambda)^2+\eta)\cos(3x(\tau)) + \sin(x(\tau))\left(1+a^2\eta+((1+\eta)(1-a^2)+\lambda^2)\cos(2x(\tau))\right)\Big) , \quad (4.59)$$

$$\frac{\mathrm{d}^2\theta}{\mathrm{d}\tau^2} = \lambda^2\frac{\cos(\theta(\tau))}{\sin^3(\theta(\tau))} - a^2\cos(\theta(\tau))\sin(\theta(\tau)) , \quad (4.60)$$

$$\frac{\mathrm{d}\psi}{\mathrm{d}\tau} = \frac{a}{\Delta(\tan(x(\tau)))}\left(2\tan(x(\tau)) - a\lambda - \sqrt{R(\tan(x(\tau)))}\right) + \frac{\lambda}{\sin^2(\theta(\tau))} , \quad (4.61)$$

$$\frac{\mathrm{d}u}{\mathrm{d}\tau} = \frac{\tan(x(\tau))+a^2}{\Delta(\tan(x(\tau)))}\left(\tan^2(x(\tau)) + a^2 - a\lambda - \sqrt{R(\tan(x(\tau)))}\right) + a\lambda - a^2 + a^2\cos^2(\theta(\tau)) , \quad (4.62)$$

where the radial potential $R(r)$ is defined as in (3.30), we wrote the functional dependence in $\Delta(r) = r^2 - 2r + a^2$ explicitly, and we already set $m = 1$ everywhere. These equations are given in terms of the constants of motion λ and η, and not the impact parameters α and β but the conversion is trivially done with (3.43) and (3.44) and does not give additional insight. The only problem could arise by considering an observer for which $\sin\theta_o = 0$. We can proceed with this as before by noting that geodesics which reach such an observer must necessarily have $\lambda = 0$. Therefore, it is enough to express the equations in terms of the impact parameters α and β and only then take the limit $\theta_o \to 0$, which ensures that the equations remain finite.

In order to solve this system numerically, we need to impose initial conditions for each coordinate (two initial values for each second order equation and one initial value for each first order equation, thus six in total). Four initial values are the positional coordinates of the observer, i.e. the starting values of the geodesic when we want to follow it "back in time". We will set the Mino time $\tau = 0$ at the observer, thus we fix $x(0) = -\pi/2$, $\theta(0) = \theta_o$, $\psi(0) = \psi_o$, $u(0) = u_o$. For each second order equation, we additionally need to state the rate of change of the coordinate at the observer. One can calculate that $x'(0) = \nu_r$ and $\theta'(0) = \beta$ for the starting point at $x(0) = -\pi/2$. We require that the impact parameters α and β are such that the point they describe lies inside the inner throat. Geodesics with impact parameters inside the inner throat do not have turning points in the radial coordinate, thus for them to be able to reach the observer at $r = -\infty$ (or equivalently $x = -\pi/2$) they must be initially ingoing, i.e. $\nu_r = -1$ (remember that we integrate "into the past"). The fact that the derivative in the radial coordinate is finite at $r = \pm\infty$ ($x = \pm\pi/2$) is a result of the coordinate change $r = \tan(x)$.

For the numerical integration we use Mathematica and its built-in function *NDSolve*. The method of choice is explicit Runge-Kutta. Because we start the integration at the observer at $r_o = -\infty$, we will stop it once we reach the source at $r_s > 0$. An example trajectory with with $r_o = -\infty$ and $r_s = +\infty$ can be found in Fig. 4.6. The observer's position and the impact parameters are chosen as in the examples in the previous section and thus the plots coincide. This is obvious since one way to validate the analytic solutions was that they would coincide with the numerical integration. However, only because the analytic and numerical solutions coincide for one specific pair of impact parameters does not necessarily mean that they match for all other pairs of impact parameters as well, which will be

discussed in the next subsection.

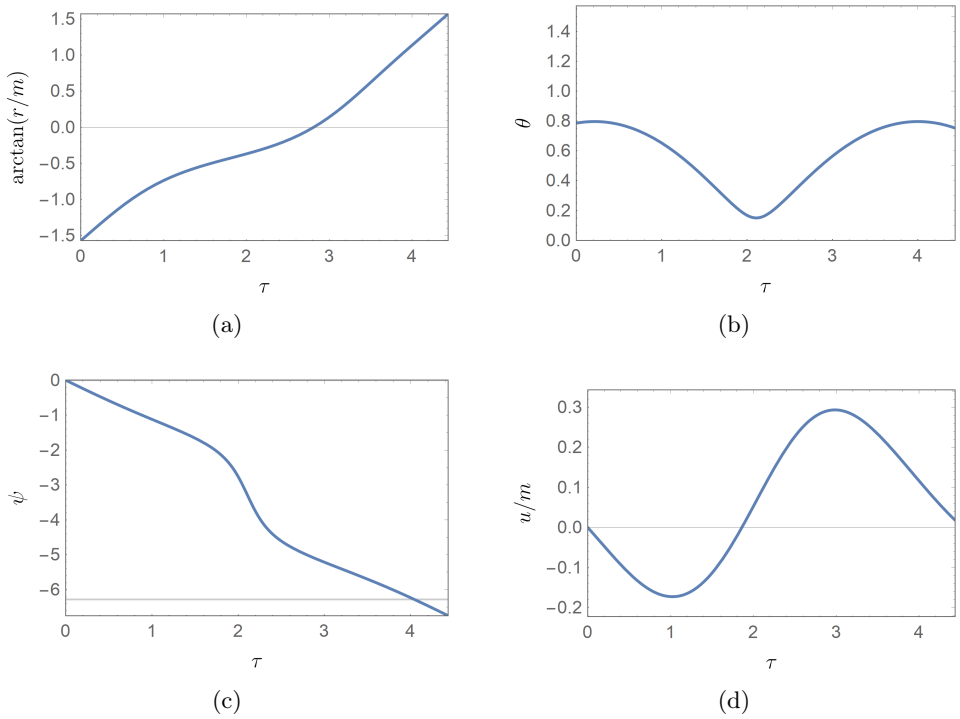

Figure 4.6.: Numerically calculated trajectories for (a) $x = \arctan(r(\tau))$, (b) $\theta(\tau)$, (c) $\psi(\tau)$ and (d) $u(\tau)$ for a geodesic with impact parameters ($\alpha = -0.15$, $\beta = 0.1$) and $r_o = -\infty$ and $r_s = +\infty$ (corresponding to $x_o = -\pi/2$ and $x_s = +\pi/2$), $\theta_o = \pi/4$, $\psi_o = 0$ and $u_o = 0$. The black hole's rotation parameter is set to $a/m = 0.99$.

4.3. Comparing analytics and numerics

With both the analytic and the numeric solution of the geodesic equations of motion we now have two distinct ways of calculating the position of the (light-emitting) source for each vortical null geodesic (photon) coming from $r_s > 0$ and with impact parameters inside the inner throat (corresponding to a point on the photographic plate of the observer). The question is what method is faster and/or more precise. In this subsection we will discuss a few differences/similarities of the analytic and numeric solution to the geodesic equations of motion and argue which solution best to use in which situation.
It should be clear that for some geodesics the two different solutions will coincide (up to a very high accuracy) since one of the premises we used to check whether the analytic antiderivatives were valid was that the resulting trajectory would coincide with the numerical integration, which we assumed to be correct. However, the analytic and the numeric trajectories need not always coincide perfectly. Simply speaking, the analytic solutions are just the difference of the antiderivatives of the integrals of motion evaluated at

the start and the end point of the geodesic, whereas the numerical integration uses a finite step size to determine the next point in the trajectory, therefore "following" the geodesic step by step. This finite step size could become a problem in impact-parameter-regions where only small deviations of the trajectory result in completely different behaviours of the geodesic, as is the case in the vicinity of the inner throat boundary. In this region minor changes in the impact parameters decide whether the radial potential has two or zero real roots, i.e. whether the geodesic gets reflected into the region it came from by reaching a turning point in the radial motion, or can pass through to the other asymptotically flat region of spacetime, thus having no radial turning points at all.
To determine how accurate the solutions are, we compare the results for θ_s, ψ_s and u_s for geodesics which are emitted at $r_s = +\infty$ and observed at $r_o = -\infty$. This is the maximal range in r and thus the error should be largest for such trajectories. In the short discussion that follows we will consider the accuracy of the equations in the example case $a/m = 0.99$ for an observer located at $\theta_o = \pi/4$, $\psi_o = 0$ and $u_o = 0$. These values are chosen such that the inner throat remains relatively big while at the same time examining (asymmetric) features arising from the rotation of the black hole. A more thorough discussion of why we chose this exact observer's location can be found at the beginning of the next chapter 5.
In this section we will talk about distances in the α-β-impact-parameter-plane. To compare the mentioned distances to the whole extent of the inner throat, recall that for $m = 1$, $a/m = 0.99$, and $\theta_o = \pi/4$ it is egg-shaped with semi-major axis of around 0.6 and semi-minor axis of about 0.5 (cf. the blue curve in Fig. 3.6).
Far inside the inner throat (up to a distance of 10^{-3} from the inner throat boundary) the difference of the analytic and the numeric solution for θ_s and u_s is maximally 10^{-9}, while in the worst case it is of the order 10^{-8} for τ_s and ψ_s. We interpret this as complete agreement of the two solutions.
As expected, the error grows with decreasing distance to the throat boundary. At a distance of 10^{-8} from the boundary the maximal error we get is around 10^{-5} in θ_s and u_s, and 10^{-4} in τ_s and ψ_s. Even closer at 10^{-10} away from the boundary we find that the maximal disagreement in θ_s, u_s, τ_s, as well as ψ_s is of order 10^{-3}. The error in the angles is still rather small in comparison with the polar and azimuthal range of θ_s ($0 < \theta_s < \pi/2$) and ψ_s ($0 < \psi_s < 2\pi$), meaning that for the observer such small angular errors would not be perceivable. Furthermore, these regions where the accuracy might get lost form a very thin strip just inside the inner throat boundary. Taking all this into account, we conclude that for all practical purposes our solutions match at least up to a distance of 10^{-10} from the throat boundary, corresponding to the agreement of the numerical and analytical solution in the region which an actual physical observer would (probably) be able to resolve. We further discuss the topic of the possible (photographic) resolution an actual physical observer could probably achieve in section 6.1.
As a rule of thumb we can say that the error we make in the calculated starting position θ_s, u_s, and ψ_s, as well as in the calculated Mino time τ_s is in the worst case of the order of machine precision ($\approx 10^{-16}$) divided by the distance to the throat boundary times 10^4.
As a final point of this subsection we want to note that the numerical integration always calculates the whole trajectory, regardless of whether we only need the source's positional values or the whole path connecting the source and the observer. This is due to the nature of numerical integration but it also adds a lot of (often unnecessary) calculations to the solution. Because of this, when we are only interested in the source's position, we will generally use the analytic formulas as they are only differences of analytic formulas

(i.e. we do not calculate any point in between the source and the observer) and thus the computation is a lot quicker. When we are interested in the whole trajectory connecting the source and the observer, we can choose which method to use since in this case both methods take more or less the same time. This freedom of choice is due to the fact that the analytic and the numerical solutions match rather well (up to very close to the inner throat boundary).
Fig. 4.7 shows the difference of the numerical and analytic solution along a vortical null geodesic with impact parameters ($\alpha = -0.15$, $\beta = 0.1$). As this corresponds to the example trajectory always considered in this chapter, the individual trajectories (calculated with both the numeric and analytical solution) can be found in the various figures in sections 4.1 and 4.2. As is expected far away from the inner throat boundary, the different solutions match up to a very high accuracy.

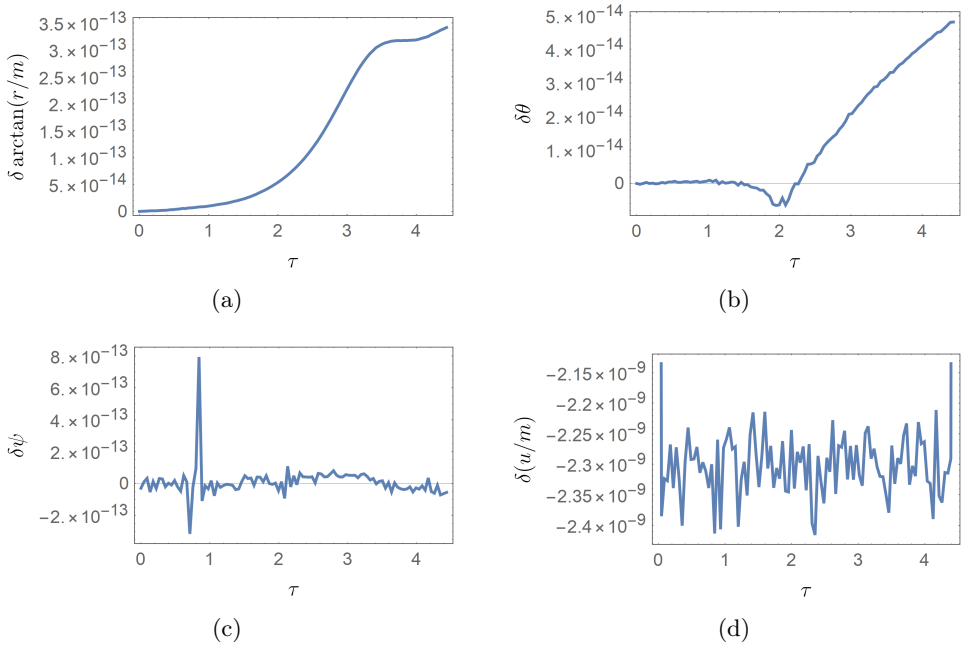

Figure 4.7.: Difference of the numerical and the analytic solution for a geodesic with ($\alpha = -0.15$, $\beta = 0.1$) along its trajectory. The black hole's rotation parameter is set to $a/m = 0.99$.

5. Visualising individual trajectories

After having solved the geodesic equations of motion in the last section, in this section we want to visualise and analyse some individual trajectories of vortical null geodesics in more detail. To this end, we will show the trajectories of some of the (arguably) more interesting vortical null geodesics in Kerr-Schild coordinates. Recall from section 2.1.3 that in Kerr-Schild form, the metric has an underlying flat spacetime and thus we will treat the coordinates (x, y, z) as pseudo-Cartesian coordinates.
Throughout this section we will consider a black hole with rotation $a/m = 0.99$. This rotational parameter just below criticality is chosen such that the effects of rotation are considerably large. The observer will be located at $r_o = -\infty$, $\theta_o = \pi/4$, $\psi_o = 0$ and $u_o = 0$. This radial position ensures that our premise of the observer far away in the negative-r-region is fulfilled, while the polar angle $\theta_o = \pi/4$ makes sure that the geodesic stays in the northern hemisphere throughout its trajectory. By doing so, it can also be guaranteed that the inner throat (i.e. the field of view of the observer) is reasonably large while still maintaining the asymmetry caused by the loss of symmetry of the spacetime in the polar direction. In comparison, if the observer would be located nearer to the equatorial plane ($\pi/4 < \theta_o < \pi/2$) the throat size would decrease while it would become more symmetric closer to the axis of symmetry ($0 < \theta_o < \pi/4$) (cf. Fig. 3.6). Furthermore, due to the rotational symmetry in the azimuthal direction, we can choose ψ_o arbitrary. The choice $u_o = 0$ corresponds to the coordinate time of the observation of the vortical null geodesic, which can also be chosen arbitrarily. We will start the integration at the position of the observer and integrate until we hit the source at $r_s = +\infty$. By inverting the parameter τ along the geodesic, we get a trajectory which starts at the source and is terminated at the observer. In this section we are more interested in the behaviour of the geodesic between the source and the observer (especially in the vicinity of the black hole) and thus the source's exact position is not important.
Recall from subsection 2.1.4 that one can cross over from one asymptotically flat region to the other (i.e. from $r > 0$ to $r < 0$ or vice versa) only by crossing the disk bounded by the ring singularity. We only consider vortical null geodesics which can never cross the equatorial plane at $\theta = \pi/2$. Hence, in Kerr-Schild coordinates they can only go from positive to negative values of z by crossing the disk located in the x-y-plane and therefore changing the sign of r. Because of that, in the plots made in Kerr-Schild coordinates which we will show in this section, the region with positive/negative z corresponds to the region with positive/negative radius r. We can therefore interpret the "upper half" of the 3D-plots as the positive-r-region while the "lower half" corresponds to the negative-r-region, both being the northern hemisphere in their respective asymptotically flat region of spacetime (defined by the polar angle between 0 and $\pi/2$). Consequently, the horizons and ergosphere are only present at positive z while the causality violating region is only present at negative z.

5.1. Trajectories in Kerr-Schild coordinates

In the last section we already showed some trajectories in Eddington-Finkelstein-like coordinates, but only considered the trajectories individually. To get a feeling for how the trajectory of a vortical null geodesic would actually look like in three spatial dimensions, we need to combine the radial and the angular solutions. In order to do so, we can transform them into Kerr-Schild coordinates (x, y, z) as described in subsection 2.1.3 and plot them in a three-dimensional Cartesian coordinate system (similarly to the discussion and plot of the horizons and the ring singularity in Fig. 2.2). However, one needs to be careful as this transformation involves the quantities $\varphi + r^{\#}$ and $u + r^*$. Due to our setup, we send photons "into the future" (the parameter τ increases along the geodesic) from the observer at negative radii to the source at positive radii, meaning that we effectively choose $\nu_r = +1$. This results in the fact that the coordinates we calculate are actually $\psi = \varphi - r^{\#}$ and $u = t - r^*$, making the standard transformation unusable because of the alternating signs in these equations. Only by using the discrete symmetry $t \to -t$, $\varphi \to -\varphi$ of the Boyer-Lindquist metric, and thus changing the geodesic from radially outgoing to radially ingoing, we get the quantities $\psi = -\varphi - r^{\#}$ and $u = -t - r^*$, allowing us to use the transformation (2.13)-(2.15) with $-\psi$ and $-u$. This way we get a geodesic which starts at $r_s = +\infty$ and is terminated at $r_o = -\infty$, as opposed to our integration starting at $r_o = -\infty$ and ending at $r_s = +\infty$.
At the end of this section the reader can find a plot of the inner throat (Fig. 5.9) where we marked the impact parameters used for the trajectories in this section. This can be viewed in anticipation of the next chapter 6, especially section 6.1.

5.1.1. Trajectory with $\alpha = -0.15$ and $\beta = 0.1$

The example trajectory of the last chapter plotted in Kerr-Schild coordinates can be found in Fig. 5.1, where (a) shows the trajectory in Eddington-Finkelstein-like coordinates and (b) shows the trajectory in Kerr-Schild coordinates. The middle plot in Fig. 5.1b shows the trajectory visualised in pseudo-Cartesian coordinates. The ring singularity is a purple ring lying in the equatorial plane at $z = 0$. Considering the scenario discussed at the beginning of this section, the starting point of the geodesic is at $r_s = +\infty$, corresponding to the direction of the green curve at $z > 0$. Along the geodesic the radial value decreases and the geodesic approaches the black hole and subsequently the disk bounded by the ring singularity. When it reaches $z = 0$, it crosses this disk and changes the sign of its radial coordinate from $r > 0$ to $r < 0$. To emphasise this, the colouring changes from green to orange at this transition. Lastly the geodesic can be seen to escape to radial negative infinity, where it is ultimately "caught" by the observation at a photographic plate or the like.
The left plot in Fig. 5.1b shows the projection of the trajectory onto the x-z-plane. We already mentioned earlier that vortical null geodesics can only go from the lower to the upper half plane of this plot by crossing the disk bounded by the ring singularity and therefore transitioning from $r > 0$ to $r < 0$ or vice versa. And since the hemisphere does not change along the trajectory, both the upper and the lower half plane correspond to the northern hemisphere in each of the respective asymptotically flat regions. We also included the intersection of the boundaries of the ergosphere (light blue) and the event/Cauchy horizon (solid/dashed grey) with the x-z-plane to this projective plot, but due to the

fact just mentioned we only added them for $z > 0$ ($r > 0$) while for $z < 0$ ($r < 0$) these surfaces are not present at all. In turn, the causality violating region can only be found for $r < 0$ – the intersection of its boundary with the x-z-plane is only plotted in the lower half plane (dark blue). It can be seen quite nicely that along the path of the geodesic which comes from $r_s = +\infty$ in the top right it first crosses the light blue curve and enters the ergosphere before crossing both the event and the Cauchy horizon and finally exiting the ergoregion again. Only then it crosses over to negative values of r by going through the disk bounded by the ring singularity (purple), emphasised by the change of colour from green to orange, until it finally escapes to $r_o = -\infty$.
In the rightmost plot of Fig. 5.1b the projection onto the x-y-plane is displayed. As before, the event horizon (continuous) and the Cauchy horizon (dashed) are coloured in grey.

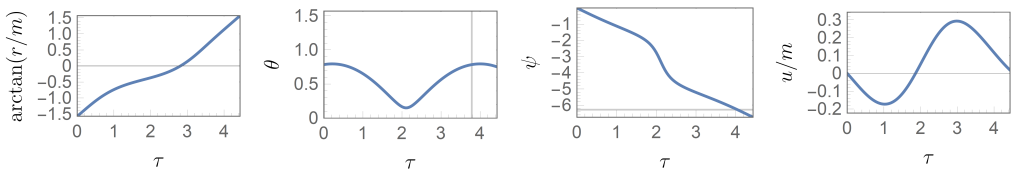

(a)

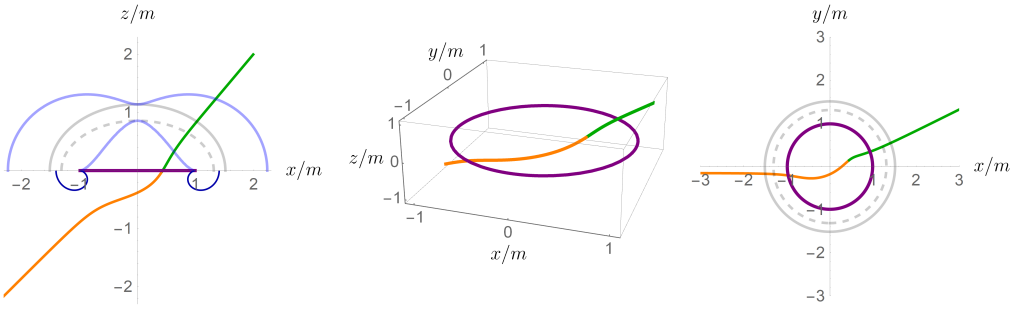

(b)

Figure 5.1.: The example trajectory of the last chapter with impact parameters ($\alpha = -0.15$, $\beta = 0.1$). (a) shows the trajectory in Eddington-Finkelstein-like coordinates while (b) shows the trajectory in Kerr-Schild coordinates. The green part of the geodesic in (b) is at positive r ($z > 0$) while the orange part is at negative r ($z < 0$). The left plot in (b) is the projection onto the x-z-plane in which the upper (lower) half plane corresponds to $r > 0$ ($r < 0$). Hence, the ergosphere (light blue) and the horizons (grey) are only drawn for $z > 0$ and the causality violating region (dark blue) is only drawn for $z < 0$. The right plot in (b) is the projection onto the x-y-axis, where we included the intersections with the horizons in grey. The ring singularity is depicted as a purple ring lying in the equatorial plane at $z = 0$.

5.1.2. Trajectories close to the inner throat boundary

The next two vortical null geodesics we will investigate in more detail are both close to the inner throat boundary. Let us start with one characterised by the impact parameters ($\alpha = -0.2315214984$, $\beta = 0$). We calculated that for $\beta = 0$ the exact throat boundary should lie at approximately $\alpha = -0.23152149851285644$. The difference of these two values is about 1.13×10^{-10}, meaning this point is more than 10^{-10} away from the boundary. This is good since we argued before that in this region the accuracy of both the analytic and the numerical solution should be acceptable, meaning we can use either solution to calculate the trajectory. However, because the numerical integration becomes problematic below a certain distance to the inner throat boundary, we will calculate this trajectory with the analytic formulas.
When envisioning a vortical geodesic very close to the throat boundary in an r-λ-plot (as in Fig. 3.2c) we expect that it passes the opening just below $r = 0$ in the close vicinity of the grey forbidden area. Thus we expect that the trajectory stays rather long at small negative radial values until it escapes to $r_o = -\infty$. During this time it may make multiple revolutions in the θ- and/or ψ-coordinate.
This is indeed also the suggestion of the plots in Eddington-Finkelstein-like coordinates, shown in Fig. 5.2a. Again the integration was done starting at the observer at $r_o = -\infty$ and terminated at the source at $r_s = +\infty$. The $\arctan(r/m)$-plot in Fig. 5.2a conveys the fact that for a rather long Mino time span (from around $\tau = 2$ to $\tau = 15$) the geodesic stays just below $r = 0$. In the same time interval, the polar angle θ oscillates multiple times between θ_+ and θ_-, and the azimuthal angle ψ wraps around the axis of symmetry multiple times. For the general spatial appearance of the trajectory in Kerr-Schild coordinates, the u-coordinate is not necessary, nevertheless, we included it here for completeness.
Similar to the previous subsection, we combine the radial and angular trajectories by using the transformation to Kerr-Schild coordinates. Thus, we are able to plot the trajectory in three-dimensional pseudo-Cartesian coordinates (Fig. 5.2b). The green corresponds again to the region with $r > 0$ while the orange part lies in the region $r < 0$. As is best visible in the left plot of Fig. 5.2b, (upon inverting the time direction) the geodesic comes from $r_s = +\infty$ and, as in the first example, crosses the ergoregion and the horizons to further transition to negative radii by going through the disk. Also in this plot it can be seen that indeed right after this transition, the geodesic stays a rather long time in the close vicinity of the ring singularity, as was suggested by the $\arctan(r/m)$-plot in Fig. 5.2a.

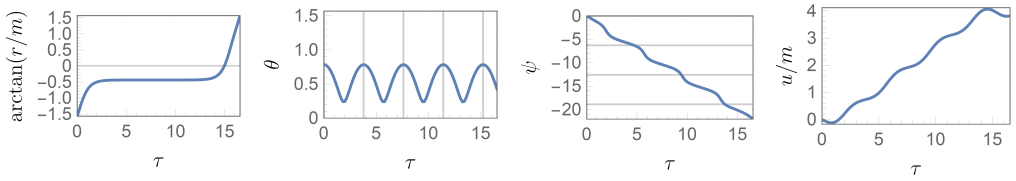

(a)

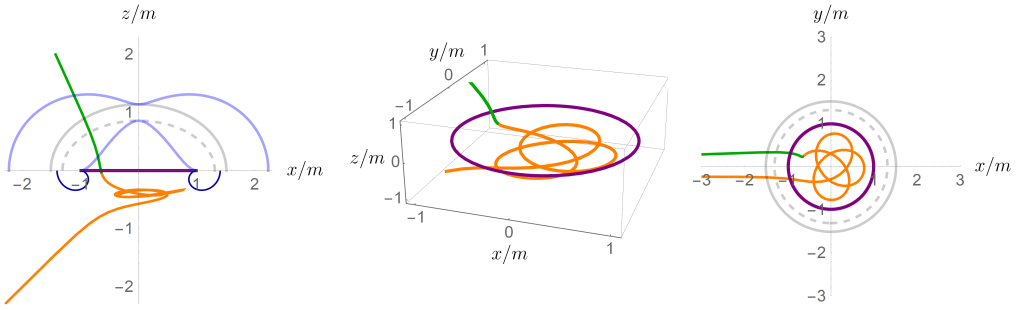

(b)

Figure 5.2.: The trajectory of a vortical null geodesic with ($\alpha = -0.2315214984$, $\beta = 0$) (a) Eddington-Finkelstein-like coordinates and (b) Kerr-Schild coordinates. (a): the $\arctan(r/m)$-plot shows that the geodesic stays just below $r = 0$ for a rather long span of Mino time; the vertical lines in the θ-plot show the periodicity of the polar angle; the horizontal lines in the ψ-plot correspond to multiples of 2π. (b): the projection onto the x-z-plane shows (in accordance with (a)) that the geodesic stays a rather long time just below $r = 0$; the projection onto the x-y-plane show that during this stay the azimutal angle constantly decreases as the geodesic "wraps around" the axis of symmetry; the ergosphere, the horizons, and the causality violating region are depicted as in Fig. 5.1b.

The second trajectory close to the inner throat boundary we want to inspect lies on the "opposite side" of the inner throat, namely at ($\alpha = 0.9783392085$, $\beta = 0$). The true throat boundary on this side is at approximately $\alpha = 0.978339208614951$, meaning that our point is around 1.15×10^{-10} away from the true boundary and thus it is ensured that the geodesic can be computed with both the numerical and the analytic solution since the accuracy is acceptable for both. As for the first geodesic close to the inner throat boundary, we will, however, again compute the trajectory using the analytic formulas.
The resulting trajectories in Eddington-Finkelstein-like coordinates can be found in Fig. 5.3a. The trajectories look for the most part similar to the ones for ($\alpha = -0.2315214984$, $\beta = 0$) in Fig. 5.2a with the exception of the ψ-solution which now increases "stepwise" rather than decreasing monotonically (as in Fig. 5.2a). Another major difference is the behaviour in the θ-component for which the lower bound is now $\pi/4$, whereas before $\pi/4$ was the upper bound. The point where θ_+ and θ_- flip is the point where they are equal at ($\alpha = +a \sin\theta_o$, $\beta = 0$), which will be discussed in subsection 5.1.3.

The corresponding path in Kerr-Schild coordinates is plotted in Fig. 5.3b. Because the ψ-coordinate in Fig. 5.3a is not monotonically decreasing, the resulting path in Kerr-Schild coordinates with ($\alpha = 0.9783392085$, $\beta = 0$) shows a completely different behaviour than the geodesic before with ($\alpha = -0.2315214984$, $\beta = 0$). As can be seen in the right plot in Fig. 5.3b it does not "wrap around" the axis of symmetry in the same manner, instead revolving around the axis of symmetry in the opposite direction. For that reason it is hard to define a meaningful measure of the order of a geodesic on the basis of the azimuthal angle ψ. In the next chapter we will see that we can use another characterisation of the order of a geodesic based on the polar coordinate. Another striking observation is that the geodesic comes very close to the ring singularity (up to around $4 \times 10^{-4} m$), yet the geodesic can never hit it. This last statement is justified by the fact that only geodesics which are bound to the equatorial plane can actually hit the ring singularity (already discussed by [5]).

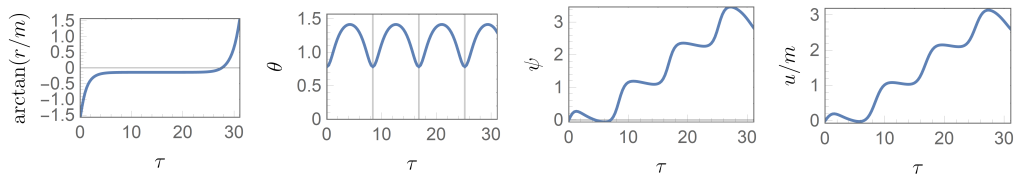

(a)

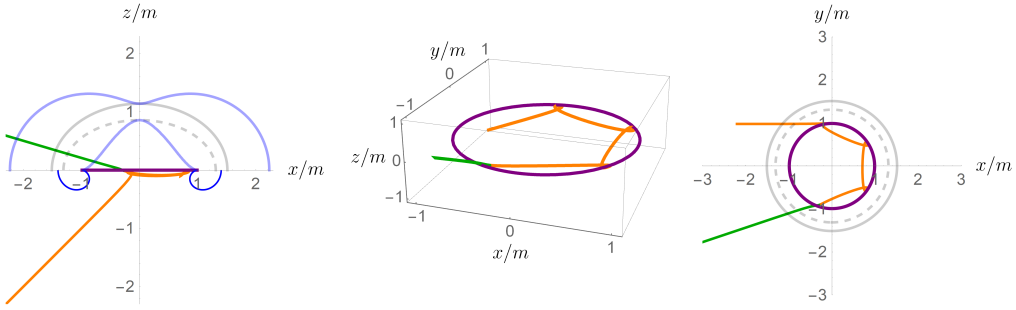

(b)

Figure 5.3.: The trajectory of a vortical null geodesic with ($\alpha = 0.9783392085$, $\beta = 0$) (a) Eddington-Finkelstein-like coordinates and (b) Kerr-Schild coordinates. (a): the arctan(r/m)-plot shows that the geodesic stays just below $r = 0$ for a rather long span of Mino time; the vertical lines in the θ-plot show the periodicity of the polar angle; the horizontal lines in the ψ-plot correspond to multiples of 2π. (b): the projection onto the x-z-plane shows (in accordance with (a)) that the geodesic stays a rather long time just below $r = 0$; the projection onto the x-y-plane shows that during this stay the azimutal angle gradually grows as the geodesic "wraps around" the axis of symmetry; the ergosphere, the horizons, and the causality violating region are depicted as in Fig. 5.1b.

Whether or not these geodesics traverse the causality violating region from subsection

2.3.4 can neither be deduced with certainty from the three-dimensional Kerr-Schild plots, nor from the projections onto the x-y-axis or onto the x-z-axis in Fig. 5.2b and 5.3b. To investigate this feature, we can inspect the value of the metric component $g_{\varphi\varphi}$ along either geodesic (remember that the causality violating region is defined as the region where $g_{\varphi\varphi} < 0$). The resulting curves are shown in 5.4. The left plots in the subfigures (a) and (b) show $g_{\varphi\varphi}$ along the geodesic parametrised by Mino time τ, whereas the right plots show $g_{\varphi\varphi}$ against the radius r/m. Since the causality violating region is only present for $r < 0$, we only need to inspect the latter in this range. Doing so for the first vortical null geodesic with ($\alpha = -0.2315214984$, $\beta = 0$) (Fig. 5.4a) shows that along its trajectory $g_{\varphi\varphi} > 0$ everywhere. However, the vortical null geodesic with ($\alpha = 0.9783392085$, $\beta = 0$) (Fig. 5.4b) travels multiple times through the causality violating region. With respect to the Mino time τ along the geodesic, these "dips" into the causality violating region seem somewhat fairly spread – this results from the fact that the geodesic stays a rather long amount of Mino time just below $r = 0$ where violation of causality can happen. Inspecting the right plot of Fig. 5.4b reveals that indeed these journeys inside the causality violating region happen for small negative r.

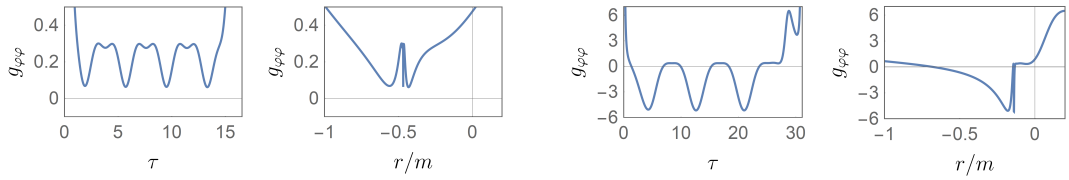

(a) $\alpha = -0.2315214984$, $\beta = 0$ (b) $\alpha = 0.9783392086$, $\beta = 0$

Figure 5.4.: The metric component $g_{\varphi\varphi}$ along the two example trajectories close to the inner throat boundary. While the geodesic with ($\alpha = -0.2315214984$, $\beta = 0$) in (a) clearly keeps $g_{\varphi\varphi} > 0$ along its trajectory, the one with ($\alpha = 0.9783392085$, $\beta = 0$) in (b) experiences $g_{\varphi\varphi} < 0$ several times at small negative r and hence traverses the causality violating region.

5.1.3. Trajectories with constant polar angle

We discussed in subsection 3.2.2 that there are certain pairs of impact parameters resulting in a trajectory with constant polar angle θ. These special points are at ($\alpha = \pm a \sin\theta_o$, $\beta = 0$), although it does not have to be the case that both these points lie inside the inner throat. However, we can say with certainty that the point ($\alpha = +a \sin\theta_o$, $\beta = 0$) is always included in the inner throat, thus we will first visualise the trajectory of a vortical null geodesic with exactly these values.
In subsection 3.2.2 we showed that along a geodesic with impact parameters ($\alpha = +a \sin\theta_o$, $\beta = 0$) not only the polar angle θ but also the azimuthal angle ψ and the coordinate time u are constant. The full trajectory in Eddington-Finkelstein-like coordinates can be seen in Fig. 5.5a.
We can again transform this vortical null geodesic to Kerr-Schild coordinates and plot it in three dimensions, shown in Fig. 5.5b. Neither the polar nor the azimuthal angle change, resulting in a straight trajectory which goes through the y-axis at $a \sin\theta_o = 0.99 \sin\pi/4$. The exact value of this crossing is just and incident as this value comes from the trans-

formation law to Kerr-Schild coordinates (2.13)-(2.15) and is not further connected to the value of α. Furthermore, with this transformation law it is easy to verify that the geodesic is a straight line in Kerr-Schild coordinates.

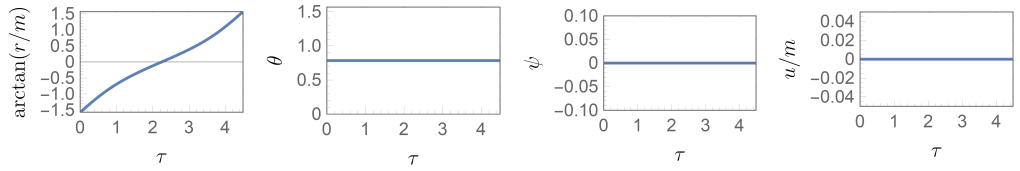

(a)

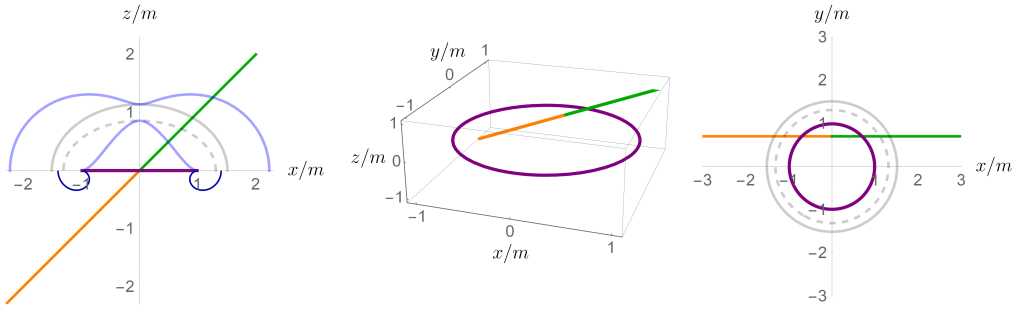

(b)

Figure 5.5.: Trajectory of a vortical null geodesic with constant polar angle θ at ($\alpha = +a\sin\theta_o$, $\beta = 0$) in (a) Eddington-Finkelstein-like coordinates and (b) Kerr-Schild coordinates. (a): θ, ψ, and u are constant along the geodesic. (b): the trajectory seems to be a completely straight line going through the y-axis at $a\sin\theta_o = 0.99\sin\pi/4$; the ergosphere, the horizons, and the causality violating region are depicted as in Fig. 5.1b.

In subsection 3.2.2 we also mentioned that in the case of ($\alpha = -a\sin\theta_o$, $\beta = 0$) we do not get constant ψ and u. To confirm this also numerically, the plots in Fig. 5.6 show a geodesic with impact parameters ($\alpha = -a\sin\theta_o$, $\beta = 0$). As this point in the impact-parameter-plane is not visible for an observer at $\theta_o = \pi/4$, we moved their position closer to the axis of symmetry to $\theta_o = \pi/8$, for which ($\alpha = -a\sin\theta_o$, $\beta = 0$) corresponds to a point inside the inner throat.
Already in Fig. 5.6a we can see that ψ and u are not constant along this geodesic, a feature which can also be observed in Fig. 5.6b.
A noteworthy feature observed in Fig. 5.6b is that the geodesic ends up much closer to the axis of symmetry (when one follows it to $r_o = -\infty$) compared with the previous cases, which is the result of the smaller polar angle of $\theta_o = \pi/8$.

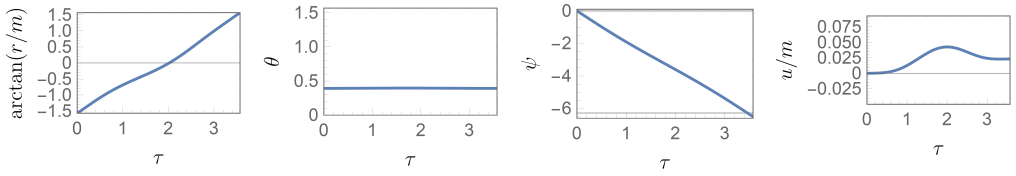

(a)

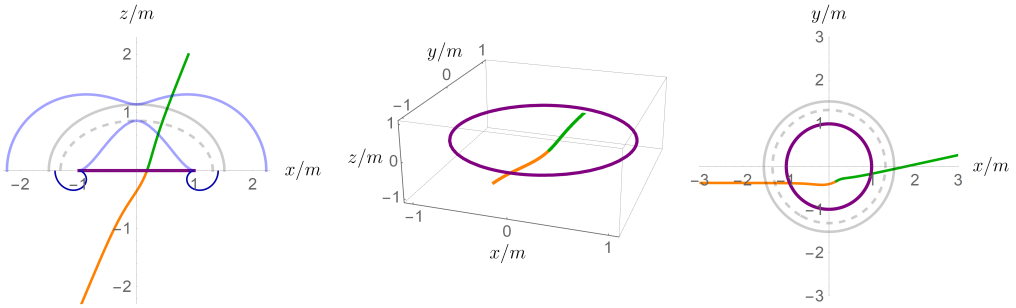

(b)

Figure 5.6.: The trajectory of a vortical null geodesic with ($\alpha = -a\sin\theta_o$, $\beta = 0$) in (a) Eddington-Finkelstein-like and (b) Kerr-Schild coordinates for an observer at $\theta_o = \pi/8$. (a): the coordinates ψ and u are not constant along the geodesic. (b): as ψ and u change along the trajectory, it is no straight line as in Fig. 5.5b; the ergosphere, the horizons, and the causality violating region are depicted as in Fig. 5.1b.

5.1.4. Trajectories going through the axis of symmetry

Concluding the visualisation of individual trajectories, we again want to argue for the necessity of changing the analytic solution for the polar angle θ (presented in subsection 4.1.4) in the case of $\alpha = 0$, namely by extending it through to negative values of θ and therefore letting it oscillate between $-\theta_+ < \theta < +\theta_+$ instead of $0 = \theta_- < \theta < \theta_+$.
For that reason we are considering three adjacent trajectories. We fixed $\beta = 0.1$ for all of them and considered geodesics with $\alpha = -0.001$, $\alpha = 0$, and $\alpha = +0.001$. We expect that a correct solution of the equations of motion give us similar geodesics in all three cases. In the first step, we will calculate these geodesics with the unmodified solution for θ from subsection 4.1.4. We will again start the integration at $r_o = -\infty$ and terminate it at $r_s = +\infty$.
The resulting curves for r, θ and u in Eddington-Finkelstein-like coordinates (shown in Fig. 5.7a) strengthen our expectation that the trajectories are similar (one cannot tell the different curves for r, θ and u apart). Note that the grey and black curves (with $\alpha \neq 0$) never touch $\theta = 0$ since $\theta_- > 0$, however the red curve (with $\alpha = 0$) does so since $\theta_- = 0$ (cf. subsection 3.2.2). Only the behaviour in ψ separates the three trajectories: The geodesic with $\alpha < 0$ (grey) seems to have a "jump down" of around $-\pi$ at $\tau \approx 2.1$ (at the point where θ_- is reached), while the one with $\alpha > 0$ (black) "jumps up" by around π

at the same time. These jumps, although being steep, are continuous.
The transformed trajectories in Kerr-Schild coordinates can be seen in Fig. 5.7b.

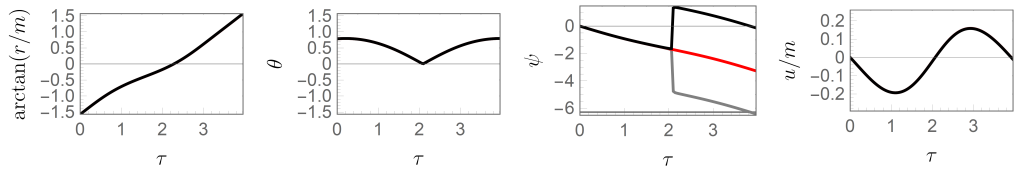

(a)

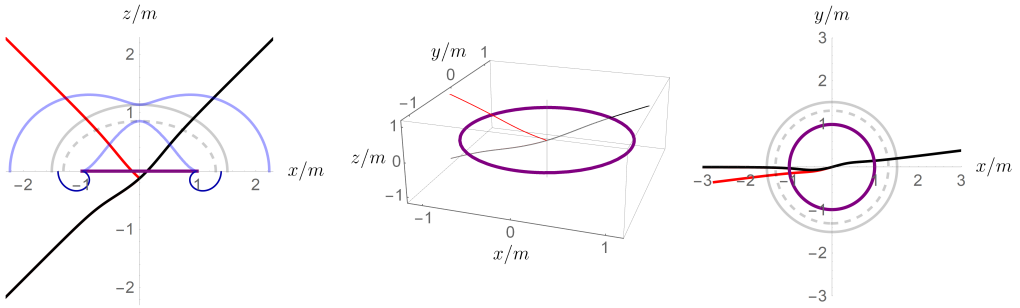

(b)

Figure 5.7.: The uncorrected trajectories of three neighbouring vortical null geodesics with $\beta = 0.1$. Here the individual trajectories are colour-coded: grey denotes $\alpha = -0.001$, red $\alpha = 0$, and black $\alpha = +0.001$. Where the trajectories overlap, only the black curve is visible. The thin vertical line in the middle plot of (b) corresponds to the axis of symmetry. For a reasonable solution, they should show similar behaviour throughout the whole trajectory in Kerr-Schild coordinates.

To interpret the "jumps" in ψ qualitatively, recall that the azimuthal coordinate increases around the axis of symmetry in the anticlockwise direction. At $\tau \approx 2.1$, the grey trajectory (with $\alpha = -0.001$) passes just to the left of the axis of symmetry. This is equivalent to a very fast rotation in ψ by around π in the clockwise direction, thus the "jump" down. The black trajectory (with $\alpha = +0.001$) experiences the opposite, namely it passes just to the right of the axis of symmetry, "jumping" up by around π in the ψ-coordinate. After the passing when the trajectories departs again from the axis of symmetry, the polar angle θ increases again.
However, the red ψ-trajectory (with $\alpha = 0$) is smooth throughout its whole path, resulting in an effective reflection at the axis of symmetry, as can be seen quite nicely in Fig. 5.7b. The only way that it would not get reflected in this manner is to either (1) add or subtract an additional π to the azimuthal coordinate, therefore going around the axis of symmetry artificially, or (2) extend the domain of θ to negative values, thus letting the geodesic really cross over the axis of symmetry. As the latter seems more natural, we will choose option (2). The numerical solution results also in variant (2). To extend the domain of θ we need to modify the solution of the integral equation of motion as described in subsection 4.1.4.

The resulting corrected trajectory of the three example geodesics can be seen in Fig. 5.8.

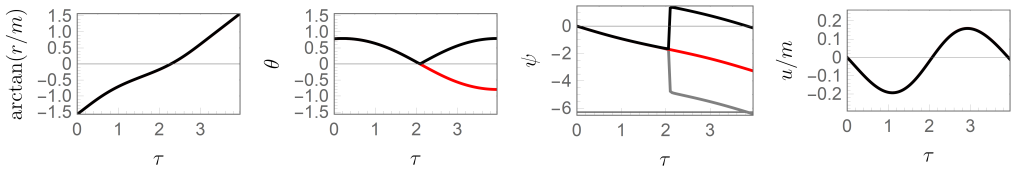

(a)

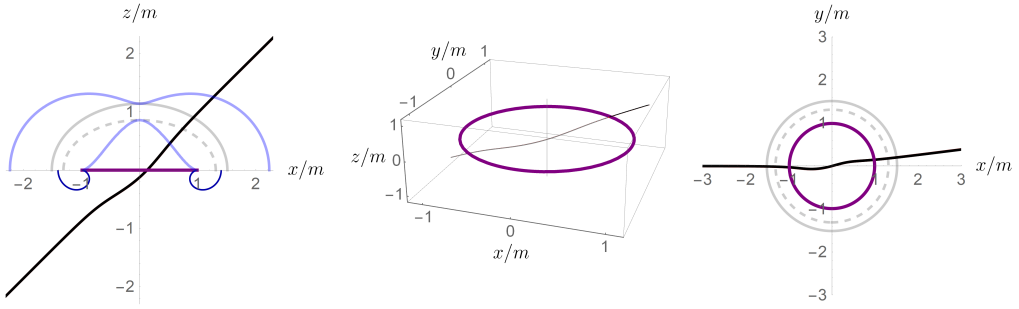

(b)

Figure 5.8.: The corrected trajectories of the three neighboring vortical null geodesics from Fig. 5.7. The colour-coding is the same as before. The thin vertical line in the middle plot of (b) corresponds to the axis of symmetry. These three geodesics are smooth through the axis of symmetry and show the same overall behaviour in Kerr-Schild coordinates.

On the one hand, as is evident from Fig. 5.8a, the θ-trajectory for geodesics with $\alpha = 0$ now departs from neighbouring trajectories with $\alpha \neq 0$. On the other hand, through the modification we gained a smooth trajectory for the three neighbouring vortical null geodesics in Kerr-Schild coordinates. The main point we want to emphasise is that they now end up in the same region of spacetime. This ensures that if the source at positive radii is only finitely big and vortical null geodesics connecting the source and the observer come close to and even pass through the axis of symmetry, there will be no artefact on the observers photographic plate which would let him determine the exact position of the axis of symmetry (which would seem somewhat unnatural).
To conclude this short discussion, let us again briefly comment option (1) of creating a smooth trajectory in Kerr-Schild coordinates (which we do not choose), namely to leave the θ-solution as it is and artificially introduce a discontinuity in the ψ-solution. This discontinuity would need to be a "jump" by $\pi + 2n\pi$ where $n \in \mathbb{Z}$. By choosing $n = 0$ we would basically let the red path follow the black one, thus creating a smooth trajectory. The choice $n = -1$ would let the red trajectory follow the grey one, also resulting in a smooth trajectory. Other choices of n need not be considered as the spacetime is 2π-periodic in the azimuthal direction.

5.2. Location of example trajectories inside the inner throat

To end this chapter, we want to give the reader a feeling for where the points which were discussed in this section are located inside the inner throat. Fig. 5.9 shows the inner throat for an observer located at $\theta_o = \pi/4$, which is the scenario we discussed for the most part in this chapter. One can interpret the α-β-plane as a photographic plate for an observer very far away from the black hole. Considering this, the marked points in the plot would correspond to points where the detector would have clicked since the corresponding photon would reach it at this exact point. We want to mention that the red points ($\alpha = -0.2315214984$, $\beta = 0$) and ($\alpha = 0.9783392086$, $\beta = 0$), although seemingly almost outside the inner throat, are just inside the boundary (for $\beta = 0$ the boundary would be at approximately at $\alpha = -0.23152149851285644$ and $\alpha = 0.978339208614951$). The three neighbouring trajectories with $\beta = 0.1$ from subsection 5.1.4 are not resolved individually in Fig. 5.9 but rather appear as one purple dot due to their vicinity in the impact-parameter-plane.
Furthermore, since the second case of the geodesic with constant polar angle at ($\alpha = -a \sin\theta_o$, $\beta = 0$) was done with the observer at $\theta_o = \pi/8$, this point is not included in Fig. 5.9.
The main point we want to get across with Fig. 5.9 is that when comparing the trajectories corresponding to the individual points, we see that by going closer to the inner throat boundary the geodesic takes more and more Mino time from the source to the observer (as can be seen by the plots in Eddington-Finkelstein-like coordinates), resulting in multiple periods in the polar motion and therefore higher orders of the geodesics (cf. section 6.1).

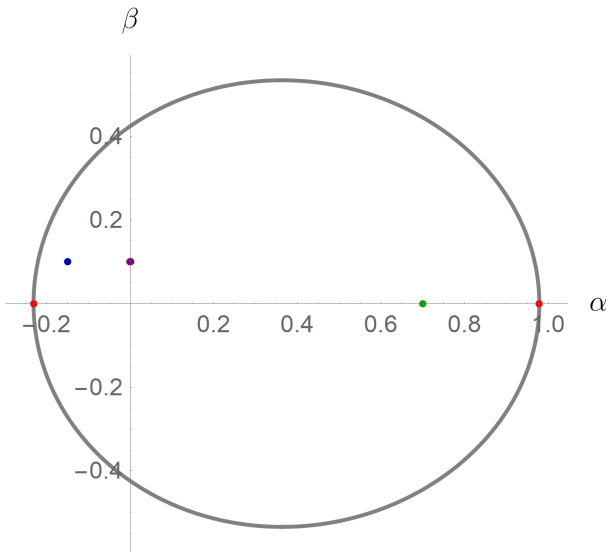

Figure 5.9.: The impact parameters of geodesics which have been discussed in this section: ($\alpha = -0.15$, $\beta = 0.1$) in blue, ($\alpha = -0.2315214984$, $\beta = 0$) and ($\alpha = 0.9783392086$, $\beta = 0$) in red, ($\alpha = +0.99 \sin(\pi/4)$, $\beta = 0$) in green, and the three neighbouring geodesics ($\alpha = -0.001$, $\beta = 0.1$), ($\alpha = 0$, $\beta = 0.1$) and ($\alpha = +0.001$, $\beta = 0.1$) in purple.

6. Visualisation of sky as seen through the disk

As the first point of this chapter we will discuss the concept of order applied to the case of vortical null geodesics inside the inner throat. In the black hole exterior, a useful definition of the order is connected to the amount of times the geodesic crosses the equatorial plane (see e.g. [11]). Since the geodesics we are considering are neither confined to the black hole exterior nor can they ever cross the equatorial plane, it is clear that this method will not work for us in a straightforward way. However, we can do something similar by classifying the geodesics based on their behaviour in the θ-coordinate.
Afterwards, in section 6.2 we will study what portion of the sky at postive radii an observer located at $r_o = -\infty$ can see. To do this, we first discretise the inner throat within Mathematica. Then, for each point thus characterised by a certain (α, β) we can calculate the angular values θ_s and ψ_s, as well as its coordinate time u_s, corresponding to the origin of the vortical null geodesic reaching the observer at the specified impact parameters. The bottom line of this section will be that the observer at $r_o = -\infty$ can only see a certain region of the sky at $r_s = +\infty$. Furthermore, we created a short film which visualises the field of view of the observer.
We can use the angular data calculated in section 6.2 to also study how an observer would perceive the sky at positive radii and what kind of distortions and/or other effects they would observe. To this end, we consider two toy light sources which span the whole northern hemisphere of the sky at $r_s = +\infty$. In addition, we animated a short sequence of snapshots illustrating what an observer with varying azimuthal coordinate would see. All of this will be discussed in section 6.3.

6.1. Order of the geodesics

In the case of the black hole exterior, one can define the order of a null geodesic by considering the amount of times it crosses the equatorial plane on its way from the emitting source to the observer [11]. In our case, this is not possible since we deal with vortical null geodesics which never cross $\theta = \pi/2$. In the Kerr exterior, instead of considering the crossings of the equatorial plane, one can equivalently consider the number of turning points in the polar angle along the trajectory [19]. The reader can easily convince themself that this is true by recalling that geodesics in the exterior region of a Kerr black hole oscillate in the polar coordinate θ around the equatorial plane at $\pi/2$.
We will pick up this characterisation with a slight modification, namely that we will not count the amount of turning points in the θ-motion but rather the number of whole periods the θ coordinate undergoes, meaning that we actually only count every second turning point. The advantage of this is that in the northern/southern hemisphere we are thus counting the number of minima/maxima in the θ-motion (i.e. the amount of times θ_- is reached), which in turn correspond to the points of closest approach of the geodesic to the

axis of symmetry. These are exactly the points where the geodesic "revolves" around the axis, and hence achieves an increase in order. It just happens to be the case in the exterior region of the black hole that these points of closest approach to the axis of symmetry correspond to both the maxima and minima in the polar motion, rather than just either of the minima/maxima for vortical geodesics in the northern/southern hemisphere. An exception to this is only made for geodesics with $\alpha = 0$, as for those we use the modified solution for θ (see subsection 4.1.4) and therefore the number of crossings of the axis of symmetry at $\theta = 0$ needs to be counted.
In our characterisation, until the geodesic motion in θ has reached one whole period, it will be considered of order zero or as direct image. Between the first whole period and the second it will be called of order one, between the second and the third it is of order two, etc. This can easily be calculated with the periodicity properties of elliptic integrals, which depend on the elapsed Mino time τ along the geodesic. For that reason we only need to calculate the difference of the final to the starting Mino time $\Delta\tau$ using (4.24), and determine the order with the periodicity properties given in subsection 4.1.1.
Consider the example of Fig. 4.2a where we highlighted the periodicity with vertical lines – according to our characterisation this would correspond to order one. On the other hand, the example close to the inner throat boundary in Fig. 5.2a is of order four following our definition.
We can calculate this order for each point inside the inner throat where we can influence the result by choosing the starting and the ending radius of the geodesic as well as the starting polar angle. The maximum order is reached when the geodesic travels from $r = -\infty$ to $r = +\infty$ (or vice versa), which is why we chose this as an example in Fig. 6.1. In Fig. 6.1a we calculated the order of 163,048 pairs of impact parameters inside the inner throat. The resolution is 2.5×10^{-3} and the closest we come to the throat boundary is 2.5×10^{-4} (in all the plots in Fig. 6.1 the closest point to the inner throat boundary is one order of magnitude smaller than the general resolution). As one can see, the vast majority of geodesics characterised in this parameter region is of order zero, indicated by the colour red. Only in the close vicinity of the throat boundary are some geodesics with order one, coloured orange. By zooming in on the small rectangle on the left side of the inner throat and enhancing the resolution we obtain Fig. 6.1b. Here, the resolution is 5×10^{-5}, and there is a clearly visible strip of first order geodesics. Zooming further in we obtain Fig. 6.1c, with a resolution of 5×10^{-6}. This is the first time that second order geodesics appear. Fig. 6.1d with a resolution of 2×10^{-7} does not give any new features, only Fig. 6.1e reveals third order geodesics for the first time. For this we needed to approach the throat boundary up to 10^{-9} with a resolution of 10^{-8}. As is also visible in the last picture, the combined yellow and blue strip of second and higher order images has a thickness of about 5×10^{-7}.

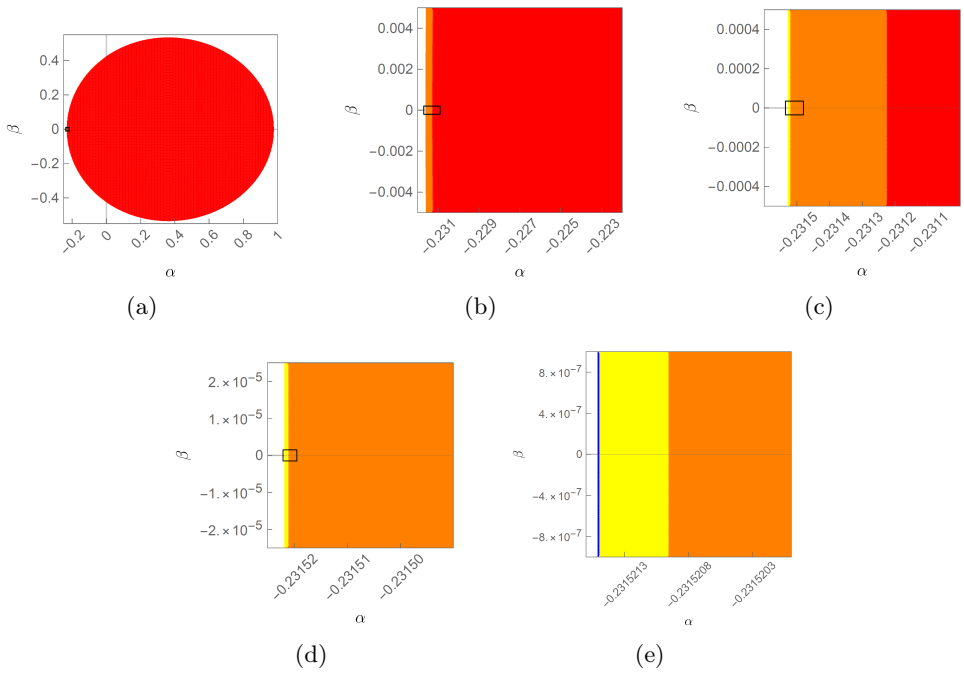

Figure 6.1.: Visualisation of the order of vortical null geodesics inside the inner throat which start at $r_o = -\infty$ and $\theta_o = \pi/4$, and end at $r_s = +\infty$. Direct images (order zero) are coloured red, first order images orange, second order images yellow, and higher orders are collectively coloured blue. From (a) to (e) we zoom ever further in onto the marked rectangular region of the previous plot.

We end this subsection with the conclusion that an observer very far away from the black hole would probably only be able to see direct and first order images of vortical null geodesics inside the inner throat. This is justified by the very demanding resolution requirements as a result of the small thickness of the images of order two and higher. Let us assume for the sake of argument that the observer uses a rectangular detector and optics such that the inner throat just barely fits inside the detector plate. We do not care about the actual optical system of the telescope the observer uses, but only about the detector itself. This would mean that the detector covers approximately the impact-parameter-region $-0.232 < \alpha < 0.978$ and $-0.538 < \beta < 0.538$. For this field of view and a required resolution of 5×10^{-7} one would need a detector with about 5.166×10^{12} pixels (or about 4.93×10^6 megapixels). Accordingly, each side of the detector would need to have between two and three million pixels. In actual astronomical observations one of the best cameras is at the Vera C. Rubin Observatory in Chile with 3,200 megapixels (approximately 3.2 billion pixels). Space telescopes have even much less detector pixels than that. Consequently, these high-order-features would probably be impossible to resolve using present-day camera technology when looking at the whole inner throat. The observer would need better optics to zoom in on one side of the inner throat as we have done in Fig. 6.1. This also seems unrealistic since it already took great effort to be able to resolve M87* as a whole with the Event Horizon Telescope.
On the other hand, the first-order-strip (orange) has a thickness of about 3×10^{-4}. The

requirement to resolve this would be a detector with less than 1.5×10^7 pixels, or about 14.3 megapixels, which is far more realistic.

6.2. Field of View

This section is dedicated to answer the question: What portion of the sky at positive radii can an observer at $r_o = -\infty$ in principle see? To this end we again consider an exemplary observer at ($r_o = -\infty$, $\theta_o = \pi/4$, $\psi_o = 0$) and integrate the equations up to $r_s = +\infty$. As before, the spacetime location of the observer is chosen such that the inner throat remains rather large while maximising the asymmetry due to the rotation of the central object, therefore being able to view the rotational effects with acceptable resolution. The black hole's rotation parameter is as usual set to $a/m = 0.99$ to ensure that rotational effects are large while still having horizons.
To calculate θ_s and ψ_s we need pairs of impact parameters (α, β) which we can put into the analytic solutions of the geodesic equations of motion. We obtain such pairs by discretising the inner throat, which is easily done in Mathematica. To be better track these pairs we colour-code them based on their distance to the centre of the inner throat – warm colours are in the middle while cool colours correspond to the region close to the inner throat boundary. This results in the appearance of the inner throat for the observer as seen in Fig. 6.2a. In total, the discretisation results in 1,492,000 pairs of (α, β) with a closest distance to the inner throat boundary of 3×10^{-4}. The distance to the boundary is chosen such that we only get first order images (cf. section 6.1). Higher order images will be discussed later in this section.
Fig. 6.2b shows the calculated starting angles in a θ_s-ψ_s-plot, where we already considered the azimuthal coordinate modulo 2π. Each point is coloured according to its point in the inner throat. It is apparent that large portions of the sky at positive radii are not visible for the observer as images of order zero – about half of Fig. 6.2b is empty as no geodesics originating from these angular regions reach the observer as zeroth order images. This statement of the very restricted (zero'th order) field of view of the observer is further reinforced by the fact that vortical null geodesics are bound to one hemisphere, meaning that Fig. 6.2b only shows half of the whole sky at positive radii (the other half would correspond to $\pi/2 < \theta_s < \pi$). It is also important to note that there is a strip close to the equatorial plane characterized by $\max(\theta_+) < \theta_s < \pi/2$ where no vortical null geodesics at all (irrespective of their order) can reach the observer. It was discussed in subsection 3.2.2 that this point of maximal θ_+ lies at the left edge of the inner throat. This forbidden region is represented by the shaded grey area in Fig. 6.2b.
In order to better visualise what portion of the sky is covered by these starting angles, one can make a polar plot where the distance to the origin is the polar coordinate θ_s while the angle around the origin (increasing in the anticlockwise direction) is the azimuthal angle ψ_s – shown in Fig. 6.2c. This can be accomplished by the transformation $(\theta_s, \psi_s) \to (\theta_s \cos(\psi_s), \theta_s \sin(\psi_s))$ and plotting the resulting pairs in a Cartesian coordinate grid. Doing this allows us to view Fig. 6.2c as the projection of the northern hemisphere onto a two-dimensional plane. The boundary of the plot is the equatorial plane, represented by a circle with radius $\pi/2$. As in Fig. 6.2b, irrespective of the order of the vortical null geodesics, there is a strip (now in form of an annulus of thickness $\max(\theta_+)$, again depicted as a shaded grey region) which is inherently not observable for an observer at negative

radii. A minor insight from this polar plot is that the region of the sky at $r > 0$ which the observer can see as zeroth order images is actually even smaller than suggested by Fig. 6.2b. This stems from the fact that the field of view covers the region around the axis of symmetry at $\theta_s = 0$. Furthermore, it becomes apparent that the vast majority of the inner throat (e.g. the middle to the dark blue region in Fig. 6.2a) corresponds only to a very limited portion of the sky at positive radii. This visible region is apparently almost centred around ($\theta_s = \pi/4$, $\psi_s = 0$) – the exact same values as at the observer ($\theta_o = \pi/4$, $\psi_o = 0$) – and only slightly shifted in the negative azimuthal direction (as can be seen in Fig. 6.2b). Because of the periodicity in the azimuthal direction, this results in a shift of the centre to just below 2π, which can best be observed in Fig. 6.2b. One might explain this fact as stemming from the rotation of the black hole in the negative azimuthal direction as seen by the observer at $r_o = -\infty$. Only by approaching the boundary region of the inner throat (purple region in Fig. 6.2a), the field of view vastly increases in size, thus "fanning out", and seemingly shifting in the positive ψ-direction.

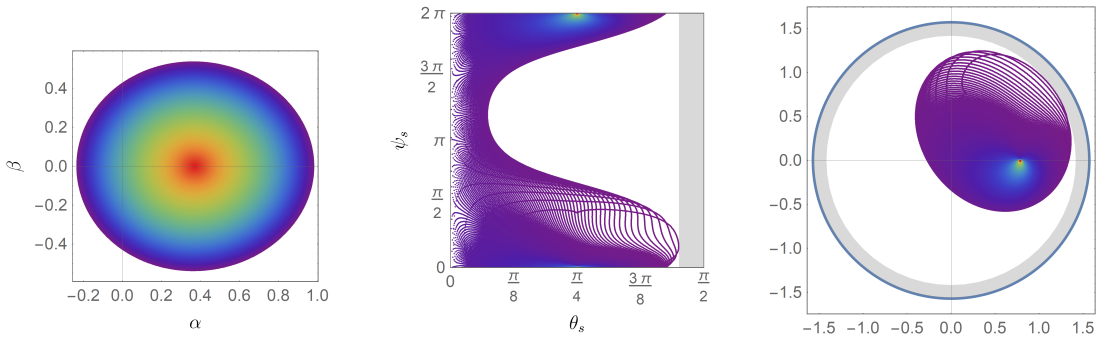

(a) (b) (c)

Figure 6.2.: The field of view for an observer at ($r_o = -\infty$, $\theta_o = \pi/4$, $\psi_o = 0$). (a): The inner throat as seen by the observer. The minimal distance to the inner throat boundary is $d = 0.0003$. (b): The calculated pairs of starting angles (θ_s, ψ_s) for geodesics starting at $r_s = +\infty$. The grey area is the forbidden region $\max(\theta_+) < \theta_s < \pi/2$. (c): The calculated starting angles (θ_s, ψ_s) in a polar plot. Here the distance to the origin is the polar angle θ_s while the angle going around the origin in the anticlockwise direction is ψ_s. The blue circle with radius $\pi/2$ corresponds to the equatorial plane, the forbidden region is now an annulus with thickness $\pi/2 - \max(\theta_+)$.

A further feature of the resulting curves in the polar plot is that these curves develop caustic-like structures before they fold in on themselves at certain distances from the inner throat boundary. Due to the overlapping of curves, this can hardly be seen in Figs. 6.2b and 6.2c, which is why we included Fig. 6.3, showing the outermost purple ring inside the inner throat from Fig. 6.2a with a distance to the boundary of $d = 0.0003$, as well as the corresponding starting angles (θ_s, ψ_s) in a polar plot. In the left plot of Fig. 6.3 the considered ring is coloured orange while the inner throat boundary is depicted in grey (the throat boundary and the ring are not distinguishable because of the small value of d). For better readability of how the ring inside the inner throat corresponds to the curve in the polar plot, certain points are marked by coloured dots.

The left edge of the inner throat is marked by a red dot – the location at which a caustic-like structure develops in the polar plot in the course of approaching the inner throat boundary. Going even closer to the inner throat boundary, one finds that the curve consequently folds in on itself and thus turns "inside out". By comparing the distance $d = 0.0003$ from the inner throat boundary (where this caustic appears) to the thickness of the strip corresponding to first order in Fig. 6.1, we see that the "folding" happens exactly at the point where geodesics transition from order zero to order one.
The green dot is located on the right edge of the considered ring. Since the right edge of the inner throat is where the maximum of θ_+ occurs (cf. subsection 3.2.2), the green dot in the polar plot is closest to the equatorial plane (i.e. the blue circle with radius $\pi/2$). The region between this $\max(\theta_+)$ and the equatorial plane is a forbidden region (shaded grey), represented in a polar plot by an annulus with inner radius $\max(\theta_+)$ and outer radius $\pi/2$ from which no geodesics reaching the observer at $r_o = -\infty$ can originate. As the distance to the inner throat boundary decreases, the green dot approaches the border of the forbidden regions multiple times, each one corresponding to an increase in order (defined on the periodicity of θ).

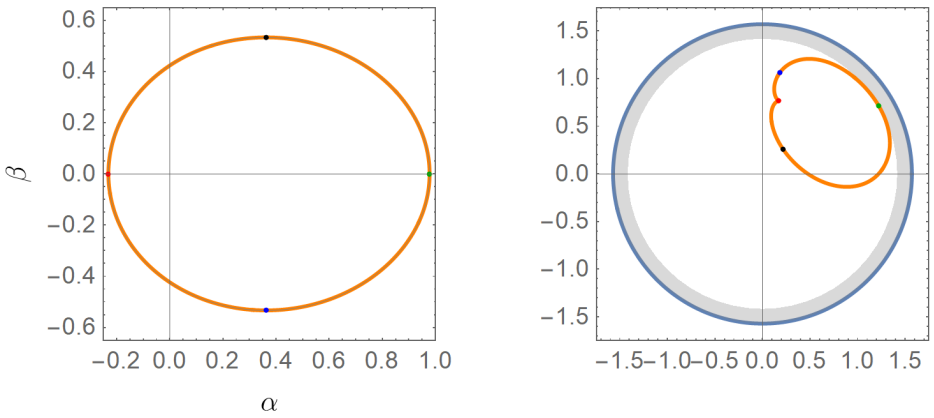

Figure 6.3.: Field of view for a ring inside the inner throat with a distance of $d = 0.0003$ away from the inner throat boundary. This corresponds to the closest ring to the inner throat boundary seen in Fig. 6.2. Already here the caustic like structure, developing at the verge of two different orders of geodesics, can be observed. The coloured dots are included for better orientation. The forbidden region is a shaded annulus with thickness $\pi/2 - \max(\theta_+)$.

The features just described can be seen better in a film we made (see https://www.quantagon.at/masters-thesis/), from which Fig. 6.3 is but one frame. In this film, we again considered centred rings inside the inner throat, growing in size from frame to frame and thus approaching the inner throat boundary (until the point where the analytic and the numerical solutions cease to coincide). The calculated starting angles (θ_s, ψ_s) are plotted in a polar plot as in Fig. 6.3.
It is clearly visible that the field of view shifts in the anticlockwise direction in the polar plot as the corresponding curve in the inner throat approaches the boundary, thus covering large portions of the sky at positive infinity close to the inner throat boundary.
Also the formation of caustic-like structures in the polar plot and the subsequent "folding"

of the curve at the transition of geodesics with order n to order $n+1$ can be extended to $n \geq 1$. Further snapshots of the film at the transitions of order n to order $n+1$ (for $n = 0, 1, 2$) can be found in Fig. 6.4. Here we omit the corresponding plots of the inner throat because one cannot distinguish the orange curves and the throat boundary for such small distances d. The transitions to higher orders happen at approximately $d = 3 \times 10^{-4}$, $d = 5 \times 10^{-7}$, and $d = 9 \times 10^{-9}$. These numerical values are in agreement with section 6.1. The fact that the curve in the polar plot folds in on itself means that the field of view covers the same part of the sky more than once. This results in the observer seeing multiple images of the same radiating object at $r_s = +\infty$, each one corresponding to a specific order of vortical null geodesics. Therefore, as in the exterior case of the Kerr black hole, the observer can in principle see infinitely many images. However, most of them are confined to a very small area in the boundary region of the inner throat and thus are not resolvable for a physical observer, as discussed in section 6.1.
Lastly, we can hereby numerically verify a finding from subsection 3.2.2. By inspection of the green dot (corresponding to the rightmost point of the considered ring inside the inner throat) in the polar plot of the film, it becomes clear that this point comes closer to the equatorial plane than all other points but never crosses the forbidden (grey) region. This can be ascribed to the fact that the maximum of θ_+ is reached on the right edge of the inner throat.

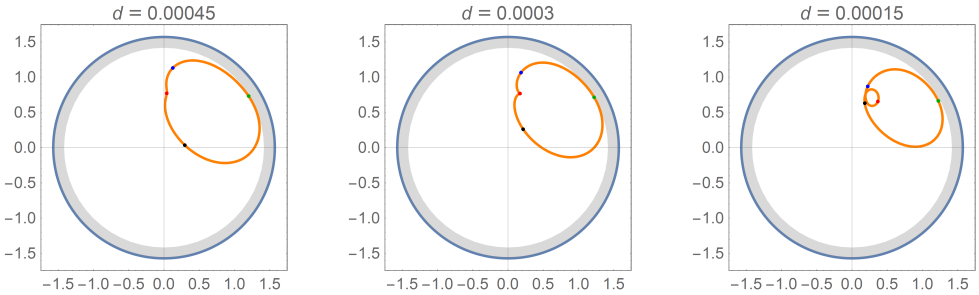

(a) Transition from zero'th to first order

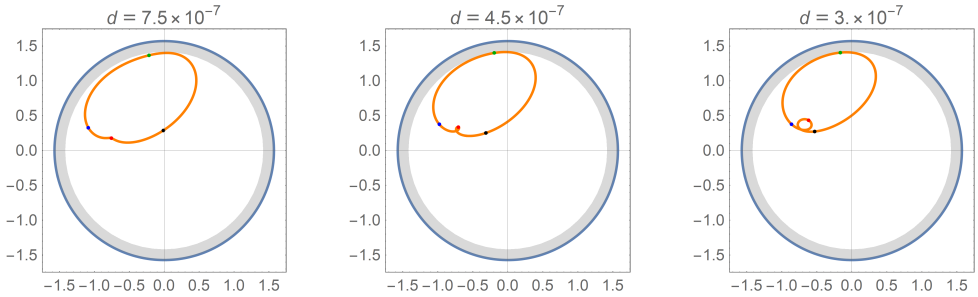

(b) Transition from first to second order

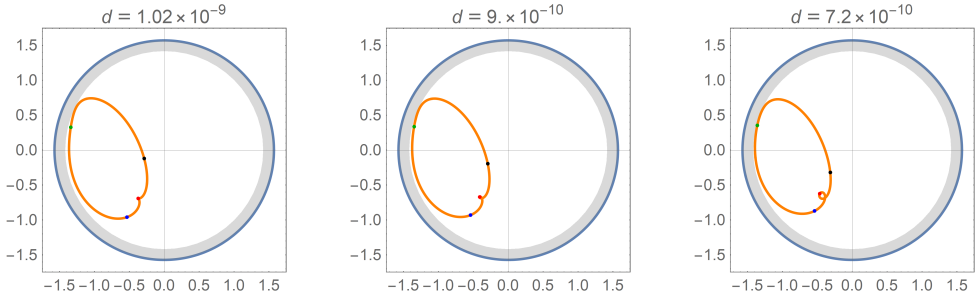

(c) Transition from second to third order

Figure 6.4.: The polar plots at the transition of the left edge of the inner throat (red dot) to higher orders, signalled by the occurrence of a caustic-like structure followed by the curve "folding in" on itself. The orange curve corresponds to a centred curve in the inner throat with distance d to the boundary.

6.3. Observing the sky

Having discussed what portion of the sky at $r_s = +\infty$ the observer at $r_o = -\infty$ can in principle see, we now want to find out how they would perceive a source lying in this field of view. In particular, we are interested in any effects distorting the appearance of the source as seen by the observer such as rotations, reflections, stretching or compression, etc. To visualise these distortions we will assume that the whole sky at $r_s = +\infty$ radiates light. For the inner throat we take the same discretisation as in Fig. 6.2a, and thus we can also use the starting angles (θ_s, ψ_s) as they were calculated before. For the colour of the emitted light we will consider two simple toy sources which will give us insight in distorting effects.
Furthermore, we can consider the observer "orbiting" around the black hole by varying their azimuthal angle ψ_o while keeping θ_o fixed. Thus, the observer circles around the black hole at a certain altitude determined by their polar angle. Without considering any frequency shifting effects, we consequently get snapshots of the distortion effects for such an orbiting observer, presented in a short film (https://www.quantagon.at/masters-thesis/). This only gives non-trivial results for the case considered in subsection 6.3.2, which is why we solely created the video in this scenario.

6.3.1. Colouring the sky in polar direction

In order to obtain the distortion in the "vertical" (polar) direction, we consider a toy source of light at $r_s = +\infty$ emitting light in four basic colours depending on the polar angle θ_s. In the range $0 < \theta_s < \pi/8$ the sky emits yellow light, for $\pi/8 < \theta_s < \pi/4$ it emits red light, for $\pi/4 < \theta_s < 3\pi/8$ it emits blue light, and finally in the range $3\pi/8 < \theta_s < \pi/2$ it emits green light. We do not need to consider the polar range $\pi/2 < \theta_s < \pi$ as this corresponds to the southern hemisphere, which vortical null geodesics arriving at the observer in the northern hemisphere can never reach. The colour pattern is illustrated in Figs. 6.5b and 6.5c, where we already overlayed the source with the calculated starting angles (θ_s, ψ_s).
In a flat spacetime, an observer at positive radii ($r_o > 0$) near the centre of symmetry would perceive the pattern we are considering here as follows: yellow would be on top (around the axis of symmetry), then lowering their sight in the direction of the equatorial plane they would perceive the colours ordered as yellow - red - blue - green (further "below" it would abruptly become black if we only assume that the northern hemisphere is radiating light).
From the distribution and the density of the pairs (θ_s, ψ_s) in Figs. 6.5b and 6.5c we can already deduce that most parts of what the observer (in curved spacetime) at $r_o = -\infty$ will see are blue and red, some parts will appear yellow, and almost nothing should be green. This last part is also true very close to the throat boundary (i.e. for any order of the geodesics), since the forbidden region $\max(\theta_+) < \theta_s < \pi/2$ lies entirely in the green part of the sky. As an alternative point of view on this we refer to section 6.2, and especially Fig. 6.2, where we have seen that the area around the middle of the inner throat corresponds to a rather confined area on the sky at $r_s = +\infty$, centred at $\theta_s = \theta_o = \pi/4$ in the polar direction. Furthermore, we see that for this light source the transition from red to blue on the sky happens at $\pi/4$, and thus the change in colour inside the inner throat lies exactly at the point of constant θ at $(\alpha = +a\sin\theta_o, \beta = 0)$. Due to the limited angular range of the starting angles, we conclude that the majority of the inner throat

must be blue and red.
This is also what is illustrated in Fig. 6.5a, which shows the appearance of the inner throat for the observer at $r_o = -\infty$ in this scenario. Each pair of impact parameters (α, β) is coloured according to the respective position on the sky at $r_s = +\infty$ of the starting angles (θ_s, ψ_s) calculated with this pair. Depending on the location of the polar angle θ_s (as seen in Figs. 6.5b and 6.5c), the point inside the inner throat is coloured yellow, red, blue, or green. It is apparent that our expectation holds true and that red and blue are indeed the most prominent colours as seen by the observer, taking up 96.5% of the inner throat (red $\approx$ 50%, blue $\approx$ 46.5%), only around 3% are yellow, and 0.5% are green. These shares do not change by much when we consider geodesics closer to the inner throat boundary (i.e. higher orders of geodesics) as they take up relatively very little space inside the inner throat and consequently also on the photographic plate of the observer.
Concerning distortion effects: we see that the differently coloured sections are not bordered by straight lines, as opposed to how an observer in a flat spacetime somewhere at positive radii would perceive them. Furthermore, the colours are skewed in one direction due to the asymmetry arising from the rotation of the black hole, while the ordering of the colours is flipped, so e.g. red is now "below" blue (as opposed for an observer in flat spacetime at $r_o > 0$). We conclude that the source appears both distorted and flipped in the polar direction for the observer.

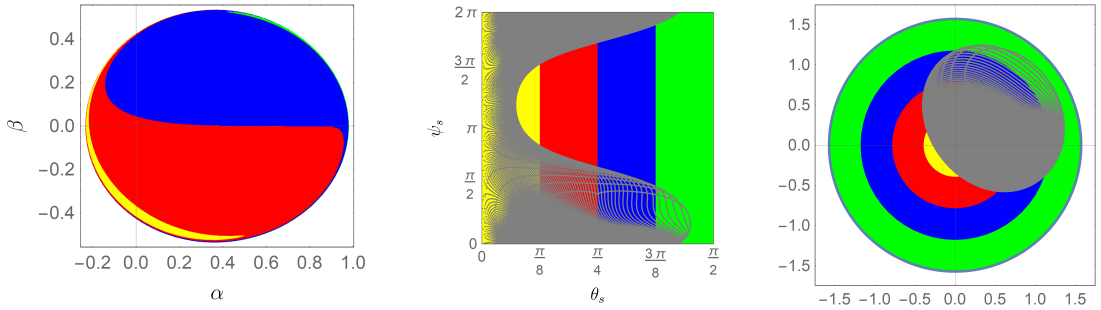

(a) (b) (c)

Figure 6.5.: Distortion of the sky at positive infinity coloured in polar direction. (a): illustration of how the observer at $r_o = -\infty$ would perceive the sky at $r_s = +\infty$ in this scenario. (b) and (c): θ_s-ψ_s- and polar plot of the toy light source separating the sky at $r_s = +\infty$ in polar direction into four sections of different colour, as well as the calculated starting angles (θ_s, ψ_s) in grey.

6.3.2. Colouring the sky in azimuthal direction

To study the distortion in the "horizontal" (azimuthal) direction, we consider another toy light source covering the whole sky at $r_s = +\infty$, emitting light in the same four basic colours as before, but now depending on the azimuthal angle ψ_s. Because the azimuthal angle has a range of 2π, the splits are as follows: for $0 < \psi_s < \pi/2$ the sky emits yellow light, for $\pi/2 < \psi_s < \pi$ it is red, for $\pi < \psi_s < 3\pi/2$ it is blue, and for $3\pi/2 < \psi_s < 2\pi$ it is green. This pattern can be seen in Figs. 6.6b and 6.6c, where we again also already plotted the starting angles (θ_s, ψ_s) to see which regions are covered (i.e. visible for the observer).

Again, let us first get an intuition how an observer in a flat spacetime at positive radii would perceive this light source. In this scenario, the coloured parts of the sky do appear to them as vertical strips meeting at the zenith (at the axis of symmetry). By considering them as such, we can say that the colours change in the horizontal direction. Starting from the border of green and yellow at $\psi_s = 0$, as the observer turns in the positive azimuthal direction ("from right to left"), they would see the colours of the sky in the order yellow - red - blue - green. After the last green strip, the colour pattern repeats because of the 2π-periodicity in the azimuthal coordinate.
Similarly to before, we can infer from the distribution and the density of the pairs (θ_s, ψ_s) in Figs. 6.6b and 6.6c what colours are most prominent for the observer at $r_o = -\infty$ (in curved spacetime). We expect that most of the inner throat should appear green and yellow, and only small parts light up in red and blue. Because the centre of the field of view is slightly shifted in the negative azimuthal direction, we can further assume that the middle of the inner throat will be coloured green. The fact that the majority of this field of view only covers a rather confined area at the sky also strengthens our suspicion that green and yellow will be the two most prominent colours, whereas red and blue do not cover a great percentage of the inner throat.
The final picture of the inner throat as seen by the observer at $r_o = -\infty$ in this scenario is illustrated in Fig. 6.6a, which matches the discussion above. In this case the relative size of the green and yellow region combined is again overwhelming at 98.4% (green $\approx 73.7\%$, yellow $\approx 24.7\%$), whereas red ($\approx 1.2\%$) and blue ($\approx 0.4\%$) are barely visible at all. In fact, the red and blue areas in the inner throat are restricted to the boundary region. This is due to the fact that the centre of the field of view lies at $\theta_s = \pi/4$ and small negative ψ_s, and only greatly increases in size by approaching the inner throat boundary, thus covering the region $\pi/2 < \theta_s < 3\pi/2$.
Finally, let us mention the distortion effects seen by the observer. It was to be expected that as before the borders separating the different colours are no straight lines, as they are seen by an observer in flat spacetime at positive radii, but rather bent and twisted. Furthermore, similarly to before, the "ordering" of the colours is flipped (e.g. green is now "left" of yellow).

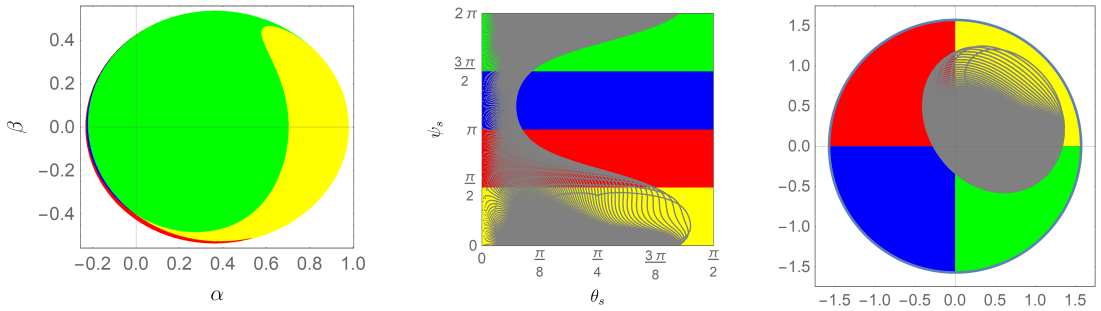

(a) (b) (c)

Figure 6.6.: Distortion of the sky at positive infinity coloured in azimuthal direction. (a): illustration of how the observer at $r_o = -\infty$ would perceive the sky at $r_s = +\infty$ in this scenario. (b) and (c): θ_s-ψ_s- and polar plot of the toy light source separating the sky at $r_s = +\infty$ in azimuthal direction into four sections of different colour, as well as the calculated starting angles (θ_s, ψ_s) in grey.

Animation of observer orbiting the black hole

The azimuthal position of the observer $\psi_o = 0$ is chosen arbitrarily, which, because of the underlying rotational symmetry of Kerr spacetime, is irrelevant for the behaviour of the vortical null geodesics. We may, however, vary this angle ψ_o, which results in the rotation of the field of view for the observer in the polar plot of Fig. 6.2c. One can see this by finding that ψ_s is only linearly dependent on ψ_o (cf. equation (4.37)). Equivalently, we can also rotate the source while keeping ψ_o fixed. However, one needs to be careful since a rotation of the observer in the positive ψ-direction is equivalent to a rotation of the source in the negative ψ-direction. Either way, the result is presented in a short film (which can be found at https://www.quantagon.at/masters-thesis/) in which the azimuthal coordinate of the observer ψ_o increases from frame to frame. Because each frame needs to be calculated individually, making a film takes a lot more computational resources. This is why we used a slightly worse resolution for the animation, only taking the starting angles (θ_s, ψ_s) for 149,000 individual pairs of impact parameters inside the inner throat into consideration. It was made sure, however, that the closest distance to the inner throat stays the same at 5×10^{-4}, thus giving the full picture of zero'th order geodesics. Apart from this difference in resolution, Fig. 6.6a corresponds to the first frame of the film.
It can be seen quite nicely that the middle of the inner throat magnifies the restricted field of view of the sky at $r_s = +\infty$ as the transitions of the colours happen rather quickly there. At the same time, the regions in the vicinity of the inner throat boundary cramp together large parts of the sky at positive infinity, thus showing multiple colours at once throughout the whole revolution of the observer around the black hole.

7. Conclusions and outlook

The purpose of this master's project was to simulate the visual appearance of a Kerr black hole for an observer far away from this central object in the region with negative radius (i.e. the region where the black hole acts repellent). The light source in this scenario is located at positive radii, meaning that the null geodesics connecting the emission point and the observer must cross both horizons as well as the disk bounded by the ring singularity.
To accomplish this task, we started in chapter 3 by presenting a derivation of the first order geodesic equations of motion [5] and transformed the resulting system from Boyer-Lindquist to Eddington-Finkelstein-like coordinates to avoid the coordinate singularity at the horizons. Then we parametrised the geodesic by Mino time [24] in order to decouple the system of differential equations, and further restricted the equations to null geodesics for which two of the four constants of motion are fixed. Upon analysing the radial potential in more detail, we found that the only null geodesics originating at positive radii and reaching arbitrary large negative radii are in a subclass called vortical null geodesics (characterised by the negativity of Carter's constant of motion). For visualisation purposes it is convenient to relate the remaining two constants of motion to impact parameters [2], functioning as a coordinate grid on a small part of the sky of an observer substantially far away from the black hole. Based on the number of roots of the radial potential, one can define an inner and an outer throat in the impact-parameter-plane [18]. Inside the inner throat no radial turning points occur and thus it served as the field of view for our observer. The analysis of the polar potential gave us insight into the polar motion of null geodesics by calculating the turning points. It turns out that vortical null geodesics are bound to one hemisphere, i.e. they can never cross the equatorial plane. Furthermore, there are at most two points inside the inner throat for which the polar angle stays constant along the whole geodesic. One of these points corresponds to the principal null congruence on which Eddington-Finkelstein-like coordinates are based [29]. We argued that a thin accretion disk around the black hole at positive radii would mostly not be visible for the observer at negative infinity. From our calculations we can additionally deduce that there is no gravitational redshift for photons travelling from positive to negative radial infinity.
In chapter 4 we solved the geodesic equations for vortical null geodesics with no radial turning point analytically (using elliptic integrals and elliptic functions) and numerically. By comparing the two approaches, we were able to correct some formulas from [17]. The numerical and analytical solutions coincide to high accuracy within a reasonable distance to the inner throat boundary.
We put these analytic solutions to use in chapter 5 where we studied some exemplary trajectories originating from positive radial infinity and going to negative radial infinity in both Eddington-Finkelstein-like and Kerr-Schild coordinates. Due to our setup, we integrate in the opposite direction, which is why one needs to be careful with the transformation between the two coordinate systems.
The beginning of chapter 6 was devoted to the classification of geodesics inside the inner throat by their order. We defined this order on the elapsed Mino time along the geodesic

and the periodicity property of its polar motion. This can be seen as a generalisation of the definition of order in the exterior case of a Kerr black hole [11][16][19][20]. We concluded that an observer with modern-day technology would only be able to resolve zero'th and first order geodesics. Thus, they could merely observe a rather restricted portion of the sky at positive infinity. A more advanced observer could in principle see infinitely many images of large parts of the sky.
Finally, we found that our observer at negative infinity would perceive a light source at positive infinity flipped in both the azimuthal, as well as the polar direction, corresponding to an effective rotation of the source by π. Two short animations (which can be found at https://www.quantagon.at/masters-thesis/) gave additional insights in both the order and the appearance of the light source.

With our analytic solutions to the geodesic equations of motion one can answer many more questions than we presented here. We state some of these questions in the following, yet defer them to future work.
In the final chapter we considered a light source at positive radial infinity as the order and the distortion effects are maximal for this setup. However, there is nothing which prevents one from modelling a more realistic scenario using our solutions to the equations of motion. Such light sources may be a star orbiting the black hole, or a thick accretion disk around the black hole at positive radii. In the case of an astrophysically acceptable thick accretion disk it would be interesting how much the observer at negative radii would be able to see (cf. discussion at the end of subsection 3.2.2). As these light sources are located at finite radii and are non-stationary, it is necessary to calculate the corresponding gravitational redshift and frequency shift from the source to the observer along the vortical null geodesic. By doing this and devoting enough computational resources (as well as writing efficient code), one could generate stunning images in the spirit of [19]. Moreover, by calculating the frequency shift along vortical null geodesics one can model light curves (similar to [11]), which probably are observationally more relevant for real astrophysical missions in the near future.
Furthermore, for causality reasons it would be interesting if one can analytically determine whether a null geodesic arriving at the observer traversed Carter's time machine.
One can also ask whether there are significant changes in the behaviour of null geodesics (and thus in the appearance of the light source for the observer in our scenario) in the case of an electrically charged black hole. This requires an adaption of our analysis to the case of Kerr-Newman spacetime.

List of Figures

Bibliography

[1] M. Abramowitz and I. Stegun. *Handbook of mathematical functions : with formulas, graphs, and mathematical tables*. Applied mathematics series ; 55. National Bureau of Standards, Washington, DC, 10. print. with corr. edition, 1972.

[2] J. Bardeen. Timelike and null geodesics in the Kerr metric. In *Les Houches Summer School of Theoretical Physics: Black Holes*, pages 215–240, 1973.

[3] G. D. Birkhoff. *Relativity and modern physics*. Harvard Univ. Press, Cambridge, Mass.[u.a.], 1923.

[4] R. H. Boyer and R. W. Lindquist. Maximal Analytic Extension of the Kerr Metric. *Journal of Mathematical Physics*, 8(2):265–281, 1967.

[5] B. Carter. Global Structure of the Kerr Family of Gravitational Fields. *Phys. Rev.*, 174:1559–1571, Oct 1968.

[6] S. Chandrasekhar. *The mathematical theory of black holes*. Oxford Univ. Pr., 1985.

[7] P. T. Chruściel, C. R. Ölz, and S. J. Szybka. Space-time diagrammatics. *Physical Review D*, 86(12), Dec 2012.

[8] P. T. Chruściel, M. Maliborski, and N. Yunes. Structure of the singular ring in kerr-like metrics. *Phys. Rev. D*, 101:104048, May 2020.

[9] P. Chrusciel. *Geometry of Black Holes*. International Series of Monographs on Physics. Oxford University Press, 8 2020.

[10] P. T. Chrusciel. *Elements of General Relativity*. Compact Textbooks in Mathematics. Springer, 2020.

[11] C. T. Cunningham and J. M. Bardeen. The Optical Appearance of a Star Orbiting an Extreme Kerr Black Hole. *Astrophysical Journal*, 183:237–264, July 1973.

[12] A. Einstein. Die Grundlage der allgemeinen Relativitätstheorie. *Annalen der Physik*, 354(7):769–822, 1916.

[13] J. Fukue and T. Yokoyama. Color Photographs of an Accretion Disk around a Black Hole. 40:15—24, 1988.

[14] G. W. Gibbons and M. S. Volkov. Zero mass limit of kerr spacetime is a wormhole. *Phys. Rev. D*, 96:024053, Jul 2017.

[15] I. S. Gradshteyn, I. M. Ryzhik, A. Jeffrey, and D. Zwillinger. *Table of integrals, series and products*. Elsevier, Amsterdam ; Boston :, 7th ed.. edition, 2007.

[16] S. E. Gralla and A. Lupsasca. Lensing by kerr black holes. *Phys. Rev. D*, 101:044031, Feb 2020.

[17] S. E. Gralla and A. Lupsasca. Null geodesics of the Kerr exterior. *Physical Review D*, 101(4), Feb 2020.

[18] T. M. Helliwell and A. J. Mallinckrodt. Null geodesics in the extended Kerr manifold. *Phys. Rev. D*, 12:2993–3003, Nov 1975.

[19] O. James, E. von Tunzelmann, P. Franklin, and K. S. Thorne. Gravitational lensing by spinning black holes in astrophysics, and in the movie Interstellar. *Classical and Quantum Gravity*, 32(6):065001, Mar. 2015.

[20] M. D. Johnson, A. Lupsasca, A. Strominger, G. N. Wong, S. Hadar, D. Kapec, R. Narayan, A. Chael, C. F. Gammie, P. Galison, and et al. Universal interferometric signatures of a black hole's photon ring. *Science Advances*, 6(12):eaaz1310, Mar 2020.

[21] R. P. Kerr. Gravitational Field of a Spinning Mass as an Example of Algebraically Special Metrics. *Phys. Rev. Lett.*, 11:237–238, Sep 1963.

[22] J.-P. Luminet. Image of a spherical black hole with thin accretion disk. *Astronomy and Astrophysics*, 75:228—235, 1979.

[23] J.-A. Marck. Short-cut method of solution of geodesic equations for Schwarzchild black hole. *Classical and Quantum Gravity*, 13(3):393, 1996.

[24] Y. Mino. Perturbative approach to an orbital evolution around a supermassive black hole. *Phys. Rev. D*, 67:084027, 2003.

[25] C. W. Misner, K. Thorne, and J. Wheeler. *Gravitation*. W. H. Freeman, San Francisco, 1973.

[26] G. Nordström. On the Energy of the Gravitation field in Einstein's Theory. *Koninklijke Nederlandse Akademie van Wetenschappen Proceedings Series B Physical Sciences*, 20:1238–1245, Jan 1918.

[27] B. O'Neill. *The Geometry of Kerr Black Holes*. Peters, Wellesley, Mass., 1995.

[28] R. Penrose and R. M. Floyd. Extraction of rotational energy from a black hole. *Nature*, 229:177–179, 1971.

[29] E. Poisson. *A Relativist's Toolkit: The Mathematics of Black-Hole Mechanics*. Cambridge University Press, 2004.

[30] H. Reissner. Über die Eigengravitation des elektrischen Feldes nach der Einsteinschen Theorie. *Annalen der Physik*, 355(9):106–120, Jan 1916.

[31] A. Riazuelo. Seeing relativity-I: Ray tracing in a Schwarzschild metric to explore the maximal analytic extension of the metric and making a proper rendering of the stars. *International Journal of Modern Physics D*, 28(02):1950042, 2019.

[32] A. Riazuelo. Seeing Relativity – III. Journeying within the Kerr metric toward the negative gravity region. *arXiv*, 2020.

[33] K. Schwarzschild. Über das Gravitationsfeld eines Massenpunktes nach der Einsteinschen Theorie. *Sitzungsberichte der Königlich Preußischen Akademie der Wissenschaften (Berlin)*, pages 189–196, Jan 1916.

[34] The Event Horizon Telescope Collaboration. First M87 Event Horizon Telescope Results. I. The Shadow of the Supermassive Black Hole. *The Astrophysical Journal Letters*, 875(1):L1, 2019.

[35] S. U. Viergutz. Image generation in Kerr geometry. I. Analytical investigations on the stationary emitter-observer problem. *Astronomy and Astrophysics*, 272:355, May 1993.

[36] M. Visser. The Kerr spacetime: A brief introduction, 2007.

A. Appendix

A.1. Definitions of necessary quantities for the antiderivatives

To proceed with the calculation of the antiderivatives in section 4.1 in the same way as in [17], we need to set some ground rules and define a few quantities. For a better overview we will do this here.
In the case of no radial turning point, all roots of the radial potential $R(r)$ are complex with $r_1 = \bar{r}_2$ and $r_3 = \bar{r}_4$ (where the bar denotes complex conjugation). These roots are not hard to calculate in general but we will give the form found in [17] as they derived them in the especially compact form

$$r_1 = -z - \sqrt{-\frac{\mathcal{A}}{2} - z^2 + \frac{\mathcal{B}}{4z}}\,, \tag{A.1}$$

$$r_2 = -z + \sqrt{-\frac{\mathcal{A}}{2} - z^2 + \frac{\mathcal{B}}{4z}}\,, \tag{A.2}$$

$$r_3 = -z - \sqrt{-\frac{\mathcal{A}}{2} - z^2 - \frac{\mathcal{B}}{4z}}\,, \tag{A.3}$$

$$r_4 = -z + \sqrt{-\frac{\mathcal{A}}{2} - z^2 - \frac{\mathcal{B}}{4z}}\,, \tag{A.4}$$

$$\tag{A.5}$$

where they defined

$$\mathcal{A} = a^2 - \eta - \lambda^2\,, \tag{A.6}$$

$$\mathcal{B} = 2m\left(\eta + (\lambda - a)^2\right)\,, \tag{A.7}$$

$$\mathcal{C} = -a^2\eta\,, \tag{A.8}$$

as well as

$$z = \sqrt{\frac{\xi_0}{2}}\,, \tag{A.9}$$

$$\xi_0 = \omega_+ + \omega_- - \frac{\mathcal{A}}{3}\,, \tag{A.10}$$

$$\omega_\pm = \sqrt[3]{-\frac{\mathcal{Q}}{2} \pm \sqrt{\left(\frac{\mathcal{P}}{3}\right)^3 + \left(\frac{\mathcal{Q}}{2}\right)^2}}\,, \tag{A.11}$$

$$\mathcal{P} = -\frac{\mathcal{A}^2}{12} - \mathcal{C}\,, \tag{A.12}$$

$$\mathcal{Q} = -\frac{\mathcal{A}}{3}\left[\left(\frac{\mathcal{A}}{6}\right)^2 - \mathcal{C}\right] - \frac{\mathcal{B}^2}{8}\,. \tag{A.13}$$

Furthermore, some formulas needed in section 4.1 are

$$r_3 = b_1 - ia_1 \,, \tag{A.14}$$
$$r_1 = b_2 - ia_2 \,, \tag{A.15}$$
$$C = \sqrt{(r_3 - r_1)(r_4 - r_2)} \,, \tag{A.16}$$
$$D = \sqrt{(r_3 - r_2)(r_4 - r_1)} \,, \tag{A.17}$$
$$g_0 = \sqrt{\frac{4a_2^2 - (C-D)^2}{(C+D)^2 - 4a_2^2}} \,, \tag{A.18}$$
$$k = \frac{D^2}{C^2} \,, \tag{A.19}$$
$$k_4 = \frac{4CD}{(C+D)^2} \,, \tag{A.20}$$
$$x_4(r) = \frac{r + b_1}{a_2} \,, \tag{A.21}$$
$$h = \operatorname{sign}(\cos\theta_s) \,, \tag{A.22}$$

where a_1, b_1, a_2, b_2 are uniquely specified by the restrictions on the roots. Note that C from (A.8) is not equal to $\mathcal{C}$ from (A.16).
For the calculation of the radial solution we additionally need

$$X_4(\tau) = \frac{C+D}{2}\left(\nu_r \tau + \mathcal{I}_0(r_s)\right) \,, \tag{A.23}$$

where $\mathcal{I}_0(r_s)$ denotes the antiderivative of (4.9) for $\ell = 0$ evaluated at the source's radial position r_s, and τ is the Mino time.

A.2. Rewriting I_φ and I_t

To simplify (4.33) we start by writing it as

$$I_\varphi = \nu_r \int_{r_s}^{r_o} \frac{\mathrm{d}r}{\sqrt{R(r)}} \frac{a(2mr - a\lambda)}{(r - r_+)(r - r_-)} \tag{A.24}$$
$$= \nu_r \int_{r_s}^{r_o} \frac{\mathrm{d}r}{\sqrt{R(r)}} f_1(r) \tag{A.25}$$

and use partial fraction decomposition to rewrite $f_1(r)$. The two decompositions we need for this are

$$\frac{1}{(r - r_+)(r - r_-)} = \frac{1}{(r - r_+)(r_+ - r_-)} - \frac{1}{(r - r_-)(r_+ - r_-)} \,, \tag{A.26}$$
$$\frac{r}{(r - r_+)(r - r_-)} = \frac{r_+}{(r - r_+)(r_+ - r_-)} - \frac{r_-}{(r - r_-)(r_+ - r_-)} \,. \tag{A.27}$$

With these two formulas we can write

$$\begin{aligned} f_1(r) &= \frac{a(2mr - a\lambda)}{(r-r_+)(r-r_-)} \\ &= 2ma\frac{r}{(r-r_+)(r-r_-)} - a^2\lambda\frac{1}{(r-r_+)(r-r_-)} \\ &= \frac{2ma}{r_+ - r_-}\left(\frac{1}{r-r_+}\left(r_+ - \frac{a\lambda}{2m}\right) - \frac{1}{r-r_-}\left(r_- - \frac{a\lambda}{2m}\right)\right) . \end{aligned} \tag{A.28}$$

By inserting (A.28) back into (A.25) and using the definition of $I_\pm$ from (4.8) we find

$$I_\varphi = \frac{2ma}{r_+ - r_-}\left[\left(r_+ - \frac{a\lambda}{2m}\right)I_+ - \left(r_- - \frac{a\lambda}{2m}\right)I_-\right] . \tag{A.29}$$

Simplifying (4.47) is very similar, although it takes a few more steps. First, let us write I_t as

$$\begin{aligned} I_t &= \nu_r \int_{r_s}^{r_o} \frac{\mathrm{d}r}{\sqrt{R(r)}}\left(r^2 + \frac{2mr(r^2+a^2-a\lambda)}{(r-r_+)(r-r_-)}\right) \\ &= \nu_r \int_{r_s}^{r_o} \frac{\mathrm{d}r}{\sqrt{R(r)}}\, f_2(r) . \end{aligned} \tag{A.30}$$

Using the partial fraction decompositions (A.27) and

$$\frac{r^3}{(r-r_+)(r-r_-)} = r + r_+ + r_- + \frac{1}{r_+ - r_-}\left(\frac{r_+^3}{r-r_+} - \frac{r_-^3}{r-r_-}\right) , \tag{A.31}$$

we can rewrite $f_2(r)$ as

$$\begin{aligned} f_2(r) &= r^2 + 2m\,\frac{r^3}{(r-r_+)(r-r_-)} + (2ma^2 - 2ma\lambda)\,\frac{r}{(r-r_+)(r-r_-)} \\ &= r^2 + 2m(r + r_+ + r_-) + \frac{2m}{r_+ - r_-}\left(\frac{r_+^3}{r-r_+} - \frac{r_-^3}{r-r_-}\right) + \frac{2ma^2 - 2ma\lambda}{r_+ - r_-}\left(\frac{r_+}{r-r_+} - \frac{r_-}{r-r_-}\right) \\ &= r^2 + 2m(r + r_+ + r_-) + \frac{2m}{r_+ - r_-}\left(\frac{r_+(r_+^2+a^2) - a\lambda r_+}{r-r_+} - \frac{r_-(r_-^2+a^2) - a\lambda r_-}{r-r_-}\right) \\ &= r^2 + 2mr + (2m)^2 + \frac{(2m)^2}{r_+ - r_-}\left(\frac{r_+}{r-r_+}\left(r_+ - \frac{a\lambda}{2m}\right) - \frac{r_-}{r-r_-}\left(r_- - \frac{a\lambda}{2m}\right)\right) , \end{aligned} \tag{A.32}$$

where in the last equality we used that $r_+r_- = a^2$ and $r_+ + r_- = 2m$. Inserting (A.32) back into (A.30) and using the definitions of $I_\pm$ and I_ℓ as given in (4.8) and (4.9), respectively, gives us

$$I_t = \frac{(2m)^2}{r_+ - r_-}\left[r_+\left(r_+ - \frac{a\lambda}{2m}\right)I_+ - r_-\left(r_- - \frac{a\lambda}{2m}\right)I_-\right] + (2m)^2 I_0 + 2mI_1 + I_2 . \tag{A.33}$$